Printed graphene field-effect transistors : chemical and electrochemical control of graphene's electronic properties and applications in biosensing

Sandra Vasilijevic

UNIVERSITÉ DE PARIS

École doctorale Chimie Physique et Chimie Analytique de Paris Centre

ED 388

Laboratoire Interfaces Traitements Organisation et Dynamique des systèmes

UMR CNRS 7086

THÈSE DE DOCTORAT

Nanosciences, matériaux, surfaces

Printed graphene field-effect transistors: chemical and electrochemical control of graphene's electronic properties and applications in biosensing

Sandra Vasilijević

Directeur de thèse : Professeur Benoît Piro

Co-directeur : PhD HDR Nicolas Battaglini

Présentée et soutenue publiquement le 28 janvier 2021 devant un jury composé de :

Rapportrice	**Esma Ismailova**	PhD HDR, École de Mines de Saint-Étienne
Rapporteur	**Guillaume Wantz**	PhD HDR, Institut polytechnique de Bordeaux
Présidente du jury	**Emmanuelle Lacaze**	DR CNRS, Sorbonne Université
Examinateur	**Emanuele Orgiu**	Prof., Institut national de la recherche scientifique, Canada
Directeur	**Benoît Piro**	Prof., Université de Paris
Co-directeur	**Nicolas Battaglini**	PhD HDR, Université de Paris
Co-encadrant	**Giorgio Mattana**	PhD, Université de Paris
Invité	**Evangéline Bènevent**	PhD, Université Aix Marseille

UNIVERSITÉ DE PARIS

École doctorale Chimie Physique et Chimie Analytique de Paris Centre

ED 388

Laboratory Interfaces Traitements Organisation et Dynamique des systèmes

UMR CNRS 7086

DOCTORAL THESIS

Nanosciences, materials, surfaces

Printed graphene field-effect transistors: chemical and electrochemical control of graphene's electronic properties and applications in biosensing

Sandra Vasilijević

Supervisor: Professor Benoît Piro

Co-supervisor: PhD HDR Nicolas Battaglini

Thesis presented and defended publicly on January 28th 2021 in front of jury composed of:

Reviewer	**Esma Ismailova**	PhD HDR, École de Mines de Saint-Étienne
Reviewer	**Guillaume Wantz**	PhD HDR, Institut polytechnique de Bordeaux
President of the jury	**Emmanuelle Lacaze**	DR CNRS, Sorbonne Université
Examiner	**Emanuele Orgiu**	Prof., Institut national de la recherche scientifique, Canada
Supervisor	**Benoît Piro**	Prof., Université de Paris
Co-Supervisor	**Nicolas Battaglini**	PhD HDR, Université de Paris
Co-Supervisor	**Giorgio Mattana**	PhD, Université de Paris
Invited	**Evangéline Bènevent**	PhD, Université Aix Marseille

Acknowledgments

Acknowledgments

First and foremost I would like to gratefully acknowledge my thesis supervisors Benoît Piro and Nicolas Battaglini and my co-supervisors Giorgio Mattana and Guillaume Anquetin. Working with you was a great privilege for me and an unforgettable scientific experience. Thank you for giving me the opportunity to work on this research project, for the constant trust given to me, your patience and your readiness to always listen, which I sincerely appreciate. You were always a great source of motivation for this work. Thanks to you I have learned what it really means to be a great scientist. You are the best supervisors that I could have.

I warmly acknowledge the members of my jury who accepted to evaluate my work. Thank you Esma Ismailova and Guillaume Wantz for reviewing my thesis, Emmanuelle Lacaze and Emanuele Orgiu for examining my work and Evangéline Bènevent for your participation in jury. Thank you for the great scientific discussion during my thesis defense, which I have truly enjoyed.

Thanks to the director of the ITODYS laboratory, François Maurel, for giving me the chance to work at ITODYS and for pleasant working conditions. Thanks to Pierre François Quenin for making the administrative procedures much easier.

I was happy to be a part of the amazing and constantly growing "Bioelectronics and smart surfaces (BiOSS)" team. Thank you Samia Zrig for all the precious advice you gave to me, for your interest in my work and scientific career, Vincent Noël for bringing very useful remarks regarding my work and Steeve Reisberg for your kindness. I would like to warmly thank all dear colleagues, PhD students, post-docs and R & D engineers which I had the chance to get to know and work within BiOSS team. Special thanks to Jérémy Le Gall for his enthusiasm and the will to share with me his know-how related to the cyanobacteria culture. I had the chance to work with two internship Master students, Rémy Sequestra and Le Hoang Hoang To, who directly contributed to the realization of one part of the experiments presented in this manuscript and to whom I owe a big thanks. Thank you Julie Pham for proofreading my manuscript and all your useful remarks.

Thank you Jérôme Médard for your help in the realization of structural characterizations of my samples and Jean Pinson for very fruitful discussions about the obtained results.

Thanks to all other dear colleagues from ITODYS and LEM with whom I shared many nice moments.

Doing science would not be possible without scientific collaborations and I am entirely grateful for an unforgettable experience to pursue a 3 months doctoral internship in Montreal, Canada at the *Institut de la Recherche Scientifique* in the "Molecular and device physics" team supervised by Emanuele Orgiu. Emanuele, thank you for giving me the chance to broaden my knowledge and experimental skills on another type of graphene-based electronics. Working with a scientist like you was a great honor for me. Thanks for everything and big thanks to your great team. Thank you Chaoying Fu for all the great scientific discussions that we had and Ilknur Eryilmaz for a very warm welcome.

I am grateful to be surrounded by amazing friends Mélanie Rouelle, Marina Valenta, Caroline Deleplace, Ivana Vićentijević now Nikolić, Wilma and Nemanja Ivanišević. Thanks for always bringing joy to my life.

Thank you Mr. Ljubisav Pajkić for the constant encouragement to progress further in scientific field.

Last but not least, I am grateful to my family in Serbia: brother David and sister Gabrijela, my parents Rajko and Vesna for always believing in me, for constantly and unconditionally showing love and support. Thanks to you I never gave up on my dreams. Mom, thanks for your constant presence and encouragements to overcome each obstacle on this journey called life. I will be eternally grateful for everything you did for me. This doctoral thesis is dedicated to you.

Na kraju, ali ne i manje važno, zahvalna sam svojoj porodici u Srbiji: bratu Davidu i sestri Gabrijeli, mojim roditeljima Rajku i Vesni jer su uvek verovali u mene, konstantno i bezuslovno pokazivali ljubav. Zahvaljujući vama, nikada nisam odustala od svojih snova. Mama, hvala ti jer si uvek i konstantno bila uz mene. Zahvaljujući tebi i tvojim ohrabrenjima svaka prepreka na ovom putu, zvanom život, je savladiva. Uvek ću ti biti zahvalna za sve što si uradila za mene. Ovaj doktorat je tebi posvećen.

Dedicated to my mom Vesna
Posvećeno mojoj mami Vesni

Transistors à effet de champ à base de graphène imprimés : contrôle chimique et électrochimique des propriétés électroniques du graphène et applications en bio-détection

Résumé

Le graphène est un matériau bidimensionnel ayant des caractéristiques physico-chimiques remarquables, notamment une sensibilité élevée à son environnement électronique. Parmi les différentes applications du graphène, son utilisation comme matériau sensible dans des transistors à effet de champ (GFET) est très étudiée, en particulier à des fins de biodétection. Dans ce travail de thèse, nous avons cherché à élaborer un GFET par la technologie originale de l'impression numérique à jet d'encre et de tester les performances de ce dispositif en tant que biocapteur. Pour faire cela, une encre aqueuse à base d'une dispersion de flocons d'oxyde de graphène (GO) a été formulée puis imprimée sur des structures lithographiées de type transistor à effet de champ. Grâce à ce dispositif fonctionnant en milieu électrolytique, nous avons montré que le degré de réduction électrochimique du GO permettait de contrôler efficacement les propriétés de transport de charges dans le matériau réduit (mobilité et taux de dopage du rGO) et qu'un contrôle additionnel pouvait être obtenu via un dopage induit par une couche de molécules riches en groupements de type donneurs électroniques, adsorbées sur les flocons de rGO.

Ces GFETs à grille électrolytique, fonctionnels en milieu aqueux, ont ensuite été appliqués au suivi du métabolisme d'un organisme aquatique, à savoir une cyanobactérie. Notre dispositif électronique montre une sensibilité élevée aux variations du taux d'oxygène induit par l'activité photosynthétique de la cyanobactérie, avec un facteur d'amplification du signal électrique mille fois plus important que celui obtenu avec un dispositif équivalent, à base de semi-conducteur organique. Nous avons également montré que ce dispositif GFET pourrait être potentiellement utilisé dans le cadre de contrôles environnementaux, par exemple pour détecter la présence de polluants dans les eaux.

Mots clés : impression à jet d'encre, transistor à effet de champ à grille électrolytique à base de graphène, transport de charge, fonctionnalisation moléculaire, biocapteur.

Printed graphene field-effect transistors: chemical and electrochemical control of graphene's electronic properties and applications in biosensing

Abstract

Graphene is a two-dimensional material with remarkable physicochemical characteristics. In particular, graphene is highly sensitive to its electronic environment. Among different applications of graphene, its use as a sensitive material in the field-effect transistors (GFET) is widely studied, especially for biodetection purposes. In this work, we sought to develop a GFET using original digital printing technology and test the device performance when working as a biosensor. To achieve this, an aqueous ink based on graphene oxide (GO) flakes dispersion was formulated and printed on lithographed field-effect transistor structures. Thanks to this device, able to work in an electrolyte, we have shown that the electrochemical reduction degree of GO allowed efficient control of the charge transport properties in the reduced material (control of both the mobility and the doping rate of rGO). Moreover, the electron-rich molecules adsorbed on the rGO flakes were shown to induce additional doping effects.

These electrolyte-gated GFET devices, operating in an aqueous medium, were then used for life-cycle monitoring of an aquatic organism, the cyanobacteria. Our device shows very high sensitivity to variations in oxygen levels induced by cyanobacteria's photosynthetic activity with amplification of electric signal a thousand times greater than that obtained with an equivalent device, based on the organic semiconductor. We have also demonstrated that this GFET device could potentially be used in the framework of environmental monitoring, for the detection of water pollutants in water.

Keywords: inkjet printing, graphene-based electrolyte-gated field-effect transistor, electronic transport, molecular functionalization, biosensor.

Contents

Contents

Acronyms and Abbreviations

Acronyms and Abbreviations

A

AFM atomic force microscopy

B

BTZ bis-triazine

C

$\mathbf{C_{EDL}}$ electrical double layer capacitance

$\mathbf{C_Q}$ quantum capacitance

$\mathbf{C_{TOT}}$ total capacitance

CE counter electrode

CNP charge neutrality point

CV cyclic voltammetry

CVD chemical vapor deposition

D

DZM 3-trifluoromethyl-3-(3-octadecyloxyphenyl)

E

$\mathbf{E_F}$ Fermi level energy

$\mathbf{E_G}$ electrochemical gate potential

EDL electrical double layer

EG-GFET electrolyte-gated graphene field-effect transistor

EGOFET electrolyte-gated organic field-effect transistor

ERGO electrochemically reduced graphene oxide

F

F4-TCNQ tetrafluoro-tetracyanoquinodimethane

FET field-effect transistor

G

GCE glassy carbon electrode

GFET graphene field-effect transistor

GO graphene oxide

H

HOMO highest occupied molecular orbital

HOPG highly oriented pyrolytic graphite

I

$\mathbf{I_{DS}}$ drain-source current

$\mathbf{I_{GS}}$ gate-source current

L

LUMO lowest unoccupied molecular orbital

M

MOSFET metal-oxide-semiconductor field-effect transistor

O

OECT organic electrochemical transistor

P

PBS phosphate-buffered saline

PDMS polydimethylsiloxane

PET polyethylene terephthalate

PMMA polymethyl methacrylate

R

rGO reduced graphene oxide

rGO EG-FET reduced graphene oxide electrolyte-gated field-effect transistor

S

S/D source and drain

STM scanning tunneling microscopy

T

TPA tetra-sodium 1,3,6,8-pyrene tetra-sulfonic acid

V

$\mathbf{V_{DS}}$ drain-source voltage

$\mathbf{V_{GS}}$ gate-source voltage

$\mathbf{V_{ref}}$ potential of reference electrode

W

WE working electrode

WHO World Health Organization

Introduction

Introduction

The revolutionary work of Novoselov and Geim on two-dimensional materials, awarded by the Nobel prize for graphene discovery in 2004[1], initiated many theoretical and experimental research works on graphene-based materials. Graphene's remarkable properties such as high charge mobility, excellent electrical conductivity at ambient conditions, chemical inertness and high surface area are just some of its particular aspects attracting scientific attention. Considering their uniqueness, graphene-based materials are promising for enhancing the performance of energy storage devices such as Li-ion batteries, supercapacitors and photovoltaic cells.[2;3]. Besides, graphene's unique optical properties could also be used in transparent conductive electrodes (components of touch-screen displays), light-emitting devices, photodetectors and other optoelectronic devices.[4]

The chemical structure of graphene and its unique electronic band structure enable the control of graphene's electronic properties by means of covalent and non-covalent functionalization approaches. Additionally, graphene integration in devices such as field-effect transistors (GFETs) enables not only to control its electronic properties, but also to measure and record every change in its electronic environment through modulation of an external electric field. Moreover, GFETs are nowadays one of the promising approaches toward a great platform for sensing applications. Indeed, graphene's sensitivity to local changes in its electronic environment is very auspicious for the development of efficient (bio)sensors. In particular, electrolyte-gated graphene based field-effect transistor (EG-GFET) configuration is very convenient for bio-sensing applications, since it allows for aqueous working environment and low operating voltages. This goes hand in hand with fragile biological samples, physiological processes in living microorganisms and can be even adapted for wearable electronics.[5] Using the inkjet printing technique, fabrication of such types of devices can be accessible even outside of conventional cleanroom procedures, thus enabling low cost and time effective device production.

In this work, we wanted to take advantage of graphene's sensitivity and to combine it with practical aspects of the inkjet printing technique for the development of reliable biosensors. To do so, the challenge of printing inks containing graphene should be overcome. Graphene-based material containing oxygen groups, graphene

oxide (GO) known as highly-solution processable material, was used in this work for the formulation of a printable ink. For the integration and study of GO in GFETs, we developed an *in-situ* approach to obtain conductive, reduced-graphene oxide (rGO) directly on the bottom-contact transistor structure. Prior to the application of our device for sensing purposes, we needed to get a more in-depth insight into rGO's intrinsic electronic properties and the ways to master them. Our characterizing tool, the EG-GFET configuration was shown as the most eligible, as it is compatible with our initial goal: biosensing on rGO. Finally, we show an application of EG-GFET for life cycle-monitoring of photosynthetic organisms.

The contents of this thesis are structured as follows. To give an insight into graphene's state of the art, in *Chapter 1*, we will see some of graphene's main production techniques, properties and the ways to control them, as well as the main characteristics of GFETs toward their applications in the (bio)sensing field.

The main experimental methods and protocols will be presented in *Chapter 2*.

In *Chapter 3*, we will discuss the elaboration of printed GO films and the control of GO's electronic properties in EG-GFET configuration. Through electrochemical and molecular approaches, we will see how the electronic properties of GO change with different reduction degree and how the two-dimensional self-assemblies of original aromatic molecules can influence the doping effects in reduced graphene oxide (rGO).

The application of rGO EG-FET will be presented in *Chapter 4* where the photosynthetic activity of cyanobacteria was followed in order to obtain information about the presence of water pollutants in the environment.

One part of the experimental work was performed in Canada, as a side project carried out through an international scientific collaboration, in which graphene was used as an active material of back-gated GFET structures for the detection of biomarkers related to sepsis. This project and the main results will be presented as an Appendix to the main text.

Chapter 1

State of the art

Chapter 1

State of the art

This chapter aims to introduce the reader to the state of the art of graphene-based materials and their applications. Among numerous ways to produce graphene-based materials, some of the most important, widely used methods will be presented herein. We will take a deeper look at the physical properties of graphene before reviewing the applications. As the work of this thesis is based on the study of a graphene-based material, in particular a reduced graphene oxide in the field-effect transistor (FET) configuration, the working principle of FETs as well as the specificities of graphene-based FETs will be discussed. Also, control of the graphene's electronic properties through molecular functionalization will be presented. Finally, some of the recent work concerning the use of FETs in the sensing applications will be reviewed.

1.1 Graphene and carbon based materials

Graphene has been extensively studied in the last years due to its remarkable properties. According to IUPAC recommendations from 1994, the term *graphene* should be employed to describe 'the individual carbon layers in graphite intercalation compounds'.[6] For the first time ever, a graphene layer of atomic thickness was isolated from highly oriented pyrolytic graphite (HOPG) by Novoselov et al. in 2004.[1] HOPG was mechanically exfoliated by repeated peeling with an adhesive tape. Since then, the rise of graphene in different range of applications has been growing fast. Graphene is one of the allotropic forms of carbon. The electronic configuration of carbon with 6 electrons allows for sp^2 or sp^3 hybridization. Carbon being a structural element of two dimensional ($2D$) graphene plane, its atoms are sp^2 hybridized forming hexagonal arrangements, the so-called 'honeycomb' lattice (Figure 1.1).

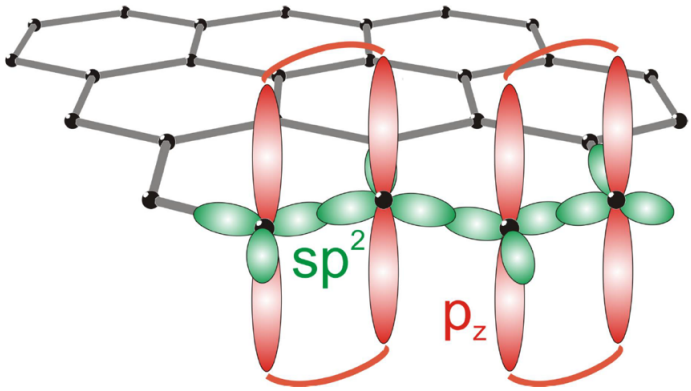

Figure 1.1: Single layer of graphene with the representation of sp^2 orbitals forming σ bonds and p_z unhybridized orbitals forming π bonds.[7]

Thanks to the $\pi - \pi$ electronic conjugation, graphene exhibits great electrical conductivity. Thanks to its valency, carbon is capable of forming different stable forms which can be classed into three groups: zero-dimensional ($0D$) fullerenes, one-dimensional ($1D$) nanotubes and two-dimensional ($2D$) referring to graphene.[8] Figure 1.2 represents all carbon ordered structures, including graphene.

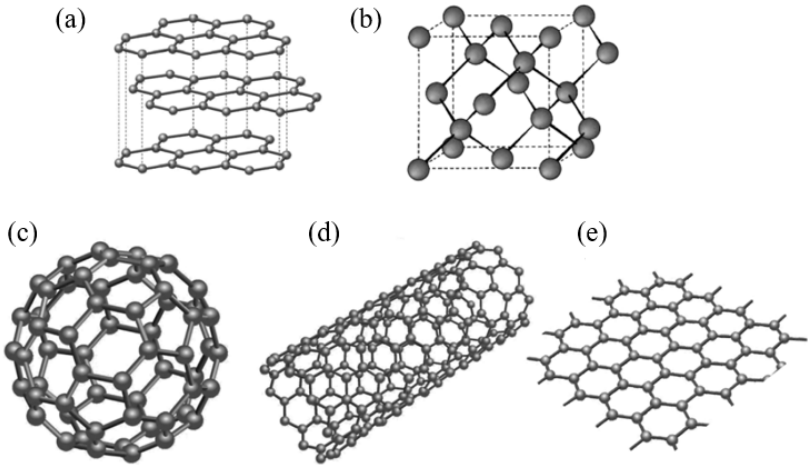

Figure 1.2: Allotropic forms of crystallized carbon: a) graphite, b) diamond, c) buckminsterfullerene (C_{60}), d) $1D$ nanotube, e) graphene.[8]

Graphite (Figure 1.2 a.) itself is nothing more than a bunch of stacked graphene layers weakly connected by Van der Waals forces with interlayer spacing of 0.34 nm[9;10]. The difference between graphite and diamond (Figure 1.2 b.) is the arrangement of carbon atoms. Diamond possesses a tetrahedral lattice with overall sp^3 hybridization, while graphite has an overall sp^2 hybridization.[11] Fullerenes (Figure 1.2 c.) are 'close caged molecules' of carbon which are geologically most abundant.[12] Carbon nanotubes (Figure 1.2 d.) and fullerenes both require high energies of formation to overcome the formation of graphite.

When it comes to research work with graphene, the production step is very important to obtain a good quality material. The good news is that there are many different ways and techniques to produce this amazing material, according to the researchers' needs, which will be discussed in the following section.

1.2 Graphene production

Graphene production techniques can be grouped into two main categories: top-to-down and bottom-to-up.[13] Top-to-down methods refer to graphite as the starting "top" material to obtain a single layer graphene ("down").

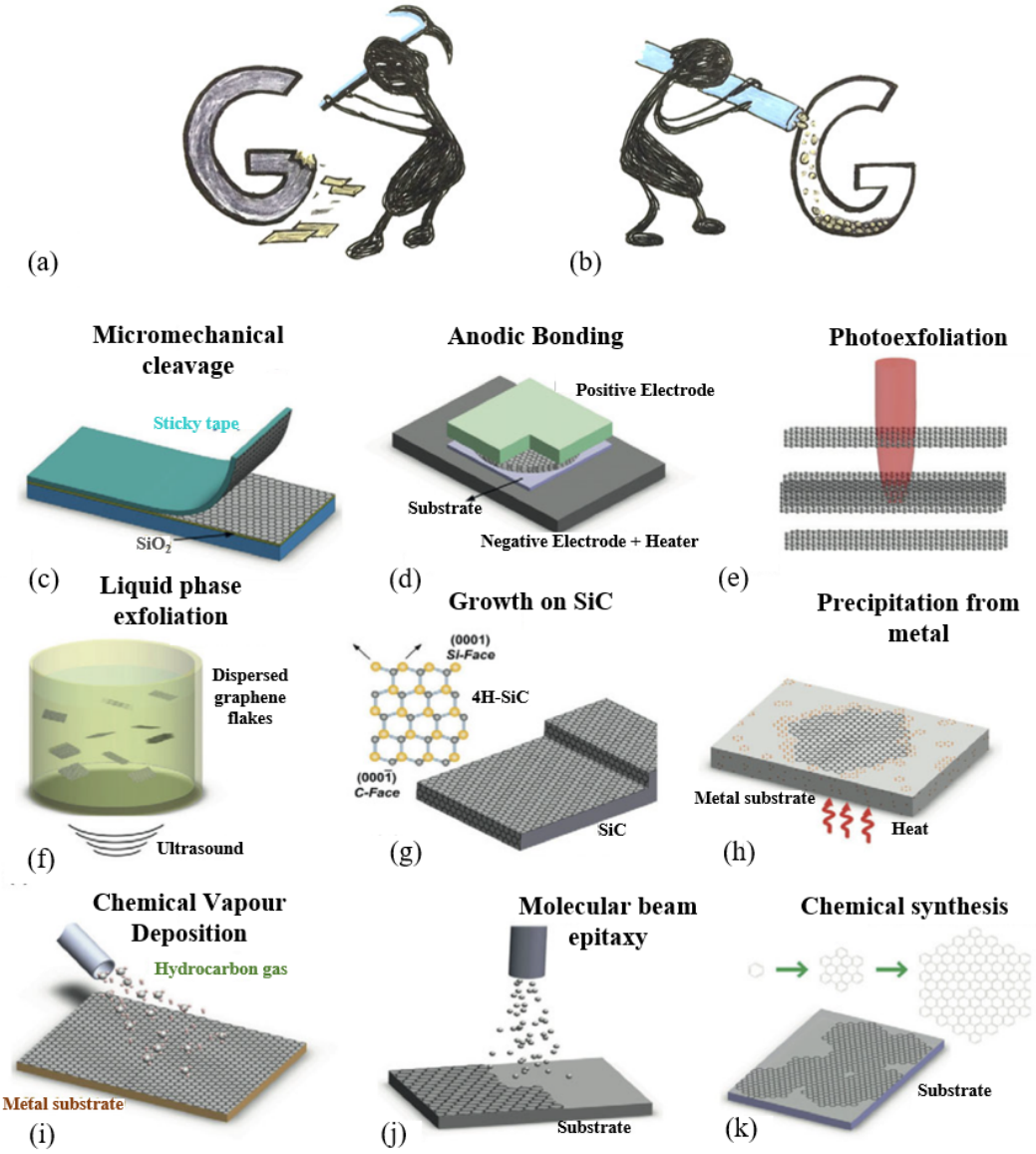

Figure 1.3: Different ways to produce graphene: a) top-down and b) bottom-up methods; c) Micromechanical exfoliation, d) Anodic bonding, e) Photoexfoliation, f) Sonication, g) SiC growth, h) Precipitation from metallic substrate, i) CVD, j) Molecular beam, k) Chemical synthesis from carbon precursors.[13]

This can be done by exfoliation (mechanical, electrochemical, liquid-phase, photo-exfoliation). On the other hand, bottom-to-up methods involve the use of carbon precursors (liquid, solid, gas precursors)[14] for establishing the graphene structure on the chosen type of substrate. Figure 1.3 shows the main fabrication methods and some of them will be described in the following subsections.

1.2.1 Graphite exfoliation

Micromechanical exfoliation of graphite (graphene's "mother" material) is probably one of the cleanest and easiest methods for graphene production, since it does not involve the use of any harsh chemicals and expensive apparatus, but just an adhesive tape. This method was first reported by Novoselov.[1] Graphene layers obtained by this technique are of the best quality. On the other hand, the yields of graphite exfoliation can be really low which makes this method inappropriate for mass production. In addition, finding a single layer for the design of a conductive channel with the desired dimensions can be time consuming.

Electrochemical exfoliation involves the use of graphite as a working electrode (WE) in electrochemical setups. The graphite source can be in the form of a graphite rod, foil/film or an HOPG crystal.[15] The essential process for this type of exfoliation is reduction and oxidation at the cathode and anode in an electrolyte to ensure the presence of charged ions.[16;17] The graphite electrode is oxidized and attracts the counter ions coming from the electrolyte, which intercalate in the graphite structure separating the graphene layers, as represented in Figure 1.4.

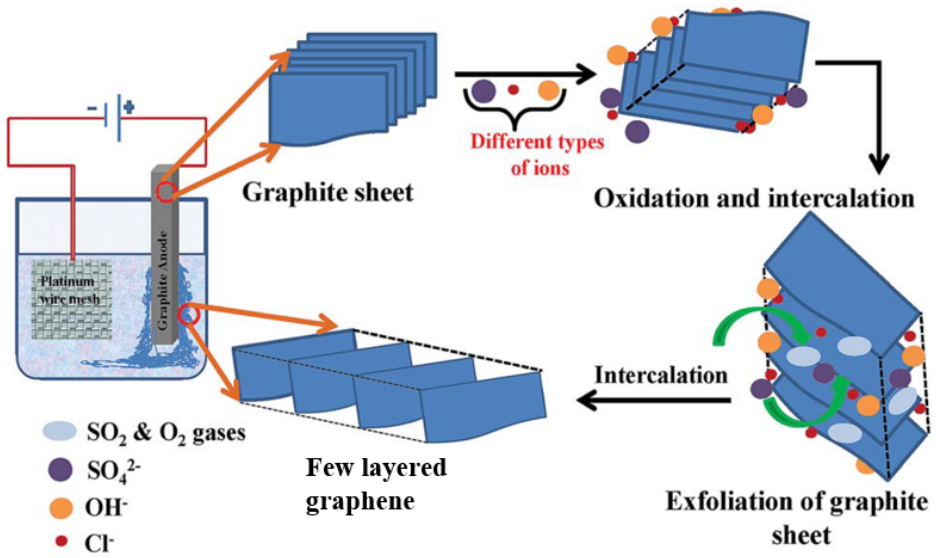

Figure 1.4: Representation of the electrochemical exfoliation mechanism.[18]

The choice of the electrolyte as well as the potential applied may be crucial for good exfoliation. The electrochemical exfoliation is usually performed in ionic liquids

or aqueous acids (H_3PO_4 or H_2SO_4).[19] Graphite exfoliated in ionic liquids mainly leads to low yields of graphene with graphene flakes of small lateral size, often functionalized with ionic liquids (disrupting the graphene structure). Better quality graphene with larger lateral size can be obtained by graphite exfoliation in aqueous acids, but graphite may be over-oxidized by acids. Depending on the potential applied between a WE and counter electrode (CE), which can be positive or negative, cathodic and anodic exfoliation can be distinguished. The exfoliation process is very fast (few minutes) and with high yields, but the main inconvenience of this method is a high level of defects produced in graphene layers.[20]

However, for the exfoliation of graphite we should keep in mind that the sources of natural graphite are limited, as this material is listed on the European list of scarce materials.[21]

1.2.2 Chemical vapor deposition (CVD) graphene

The principle of CVD technique is the decomposition of the carbon precursors using high temperatures and metallic surfaces, acting as catalysts for graphene growth. The CVD growth of graphene was demonstrated on different metallic surfaces like Rh[22;23], Cu[24;25], Ni[26;27], Fe[28;29], Co[30;31]. The main advantages of the CVD technique are the large scale graphene domains as well as the compatibility of CVD methods with industrial technologies.[32] One of the most widely used hydrocarbon precursor is methane (CH_4) which, in the case of non-catalytic thermal decomposition, requires the use of a very high temperature (1200 °C) due to strong C-H bonding (440 kJ mol^{-1}).[33] Due to the catalytic behavior of metallic surfaces, the temperature of decomposition can be lowered to less than 900 °C. The supporting surface on which the graphene is grown was observed to have an important influence. Comparing Cu to Ni, growth kinetics and reaction mechanisms of graphene are not the same. The main reason lies in the solubility of carbon: copper is known to have very low carbon solubility (< 0.001 atomic %) while carbon solubility in nickel is far more important (> 0.1 atomic %).[34] In the case of Cu, there is a negligible carbon dissolution in the bulk, resulting in a self-terminating graphene monolayer, once the surface passivates (no metal surface available for the growth).[35] In Ni and other metal surfaces mentioned above, higher carbon solubility leads to the graphene growth by bulk diffusion mechanism. Higher carbon solubility also means that the growth kinetics is more difficult to control, resulting in a non-controlled number of graphene layers.

For further use, such as electronics, CVD graphene needs to be transferred on an insulating surface like SiO_2. In the case of graphene grown on Cu foils, copper needs to be etched first. Copper etching solutions are often acidic solutions of $FeCl_3$ or HCl. Once the metal is etched, polymers such as polymethyl methacrylate (PMMA) can

be used as graphene supporting layer and easily dissolved in acetone once graphene is transferred onto the desired substrate. Polymer-free methods are described as well.[36] As graphene transfer includes several steps, sources of contaminations which could degrade the graphene quality are not negligible. For example, Fe and Cl ions from etching solutions or Cu atoms from the substrate as well as PMMA residues from the transfer step could stick on the graphene surface. Moreover, the transfer process may introduce structural defects such as cracks, holes and wrinkles.

As the obtained product is a large-scale graphene layer, further 'graphene patterning' is a necessary step, especially in the fabrication of field-effect transistors where conductive channel has to be with well-defined dimensions to avoid any current leakage. For this step, oxygen plasma etching is a widely used technique.[37;38]

Possibly the main disadvantage of CVD is the risk of contamination during the transfer process as well as the harsh growth conditions.

1.2.3 Graphene on SiC

Commercially available silicon carbide (SiC) substrates can also be used for graphene growth. The principle of this method, schematically represented in Figure 1.5, is the thermal decomposition of SiC at high temperatures ($\approx$ 1400 °C) under ambient or vacuum pressure.[39]

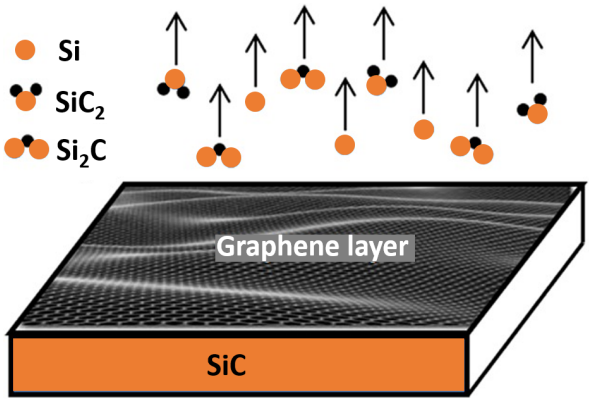

Figure 1.5: Schematic representation of SiC decomposition. Adapted from[39].

High temperatures are necessary since the Si-C bond is very strong ($\approx$ 276 kJ mol^{-1}) and a high amount of energy is needed to break this bond, allowing the evaporation of Si atoms.[40] Once Si atoms are evaporated, residual carbon atoms will rearrange into the graphene lattice on the surface. Graphene grown on SiC can be directly used for nanoelectronic applications since its $2D$ planar structure enables the use of conventional top-down lithography.[41] Compared to the CVD technique, no further transfer of the graphene layer is needed thus avoiding potential contaminations. However, this technique has some disadvantages as well, such as costly single crystal SiC substrates,

electronic properties potentially affected due to underlying SiC and small domain size with more defects compared to exfoliated graphene.[42]

1.2.4 Solution processed graphene

Manipulation of graphene can be much easier when it is solution-processed. This opens the door to the use of graphene in liquid-based deposition techniques such as drop casting and inkjet printing, among others. To do so, good dispersing solvents[a] are essential. Graphene is known to be a hydrophobic material, making the dispersions in water quite impossible.

However, Bepete et al. reported a stable additive-free dispersion of single layer graphene in water, by mixing the negatively charged graphene in tetrahydrofuran (THF) and degassed water and by evaporating the organic solvent as the final step.[43]. Furthermore, n-methyl-2-pyrrolidone (NMP), dimethyl sulfoxide (DMSO) and dimethylformamide (DMF) were also found to be good candidates. NMP yields dispersions of graphene in the range of concentrations of $0.01 - 2$ mg mL^{-1}.[44]

Li et al. reported graphene sheets suspended in DMF used in the Langmuir-Blodgett technique.[45] The treatment used in this work comprised few steps: exfoliation of graphite at 1000 °C in forming gas atmosphere, intercalation of graphite with tetrabutylammonium hydroxide (TBAOH) along with the treatment in oleum and polyethylene glycol (PEG) based surfactant. However, these harsh treatments resulted in C-O residuals demanding further annealing step (800 °C in H_2).

Making a processable graphene dispersion also requires the use of a sonication bath, where the sonication step could be very time consuming. Khan et al. reported the sonication of graphite powder for 460 h in NMP.[46] Graphene sonication for long hours is not desirable for further applications, since a high number of defects could be introduced which could alter graphene's intrinsic properties. The use of a high-shear mixer could significantly reduce the sonication times.[47]

One can also use graphene's hydrophobic character to promote its interactions with completely or partially hydrophobic molecules like ionic liquids, macromolecules and surfactants, which can help to improve its dispersibility in water or in organic solvents.[48] Nevertheless, in most cases graphene dispersions need the use of some harsh and toxic solvent to improve the dispersibility, or some additives which are difficult to remove afterwards. On the other hand, chemical modifications of graphene through the introduction of polar oxygen groups on its basal plane can be advantageous in terms of its dispersibility in water, since the material becomes more hydrophilic. This leads to the use of the well-known graphene derivate: *the graphene oxide* (GO).

[a] Although graphene is not dissolved but rather dispersed in a solution, the term "solvent" will be used in the text.

1.2.5 Graphene oxide

Graphene oxide is considered as one of the precursors for obtaining graphene. One can describe the surface of graphene oxide as a graphene layer 'decorated' with different oxygen groups. Although graphite oxide[b] was prepared for the first time in 1800's[49], its exact atomic structure remains unknown to this day. The main bottleneck is its non-stoichiometric structure as well as the lack of instrumental technique sensitive enough to quantify and characterize its structure.[50] However, chemical groups present on the surface of GO can be identified by techniques including solid state nuclear magnetic resonance (NMR), Raman spectroscopy and X-ray photoelectron spectroscopy (XPS). The Lerf-Klinowski model (Figure 1.6) is one of the most commonly used schematic model of GO. This model is based on ^{13}C NMR results.[51].

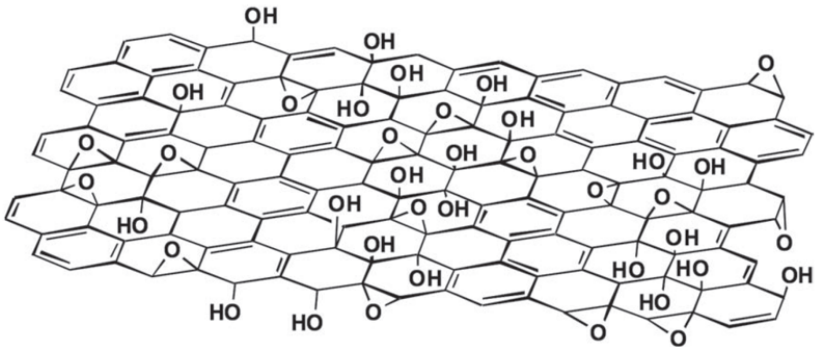

Figure 1.6: Lerf-Klinowski model representing the presence of different oxygen groups on the surface of graphene oxide.[52]

As observed in Figure 1.6, the main covalently bonded oxygen groups present on the GO surface are: epoxide (C−O−C), hydroxyl (C−OH), carboxyl (COOH) and carbonyl (C=O) groups.

GO can be obtained by three different methods or by variations of these methods[52]: Staudenmaier's[53], Brodie's[49], or Hummers method[54]. Hummers method is one of the most used methods and involves the use of sulfuric acid (H_2SO_4), sodium nitrate ($NaNO_3$) and potassium permanganate ($KMnO_4$). Improved and modified versions of Hummers method, in terms of production cost and yields, were reported.[55;56]

The presence of oxygen groups on GO's surface has its pros and cons. They render GO more hydrophilic and dispersible in water, compared to graphene. Thanks to this, GO can be further manipulated with more ease. On the other hand, the presence of oxygen groups on GO disrupts the graphene's planar structure, changing its sp^2 hybridization into sp^3. Oxygen groups can be considered as scattering centers for charge carriers, disturbing their percolation pathways and making GO an insulating

[b] N.B. Graphite oxide is graphite intercalated with oxygen groups. *Graphene oxide* can be obtained by further exfoliation (e.g. sonication) of graphite oxide.

material. This is the main reason why GO's application as the active element in electrical devices is limited.

Why then is GO called "graphene's precursor"? Initial sp^2 hybridization can be recovered by a reduction step. This reduction step contributes to the elimination of oxygen groups resulting in different forms of GO: the reduced graphene oxide (rGO) which is a conductive material. In the following subsection, the reduction of graphene oxide will be discussed.

1.2.6 Reduction of graphene oxide

Reduced graphene oxide (rGO) is often regarded as an equivalent to graphene. However, one should note that the behavior of rGO is not completely comparable to that of *pristine* (perfect, ideal) graphene. Elimination of oxygen groups also means an introduction of possible defects into the graphene's lattice. Raman spectroscopy is a powerful tool to distinguish the presence of defects in graphene-based materials. The D band in Raman spectra is assigned to the presence of defects and the G band is a typical band of graphitic materials. As shown in Figure 1.7, GO reduction leads to an increase in the D band intensity corresponding to the presence of defects introduced during the reduction step.

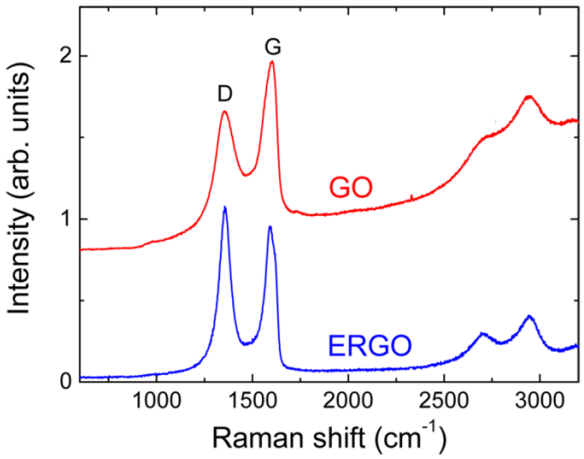

Figure 1.7: Raman spectra of GO and electrochemically reduced GO (ERGO).[57]

One should note that the removal of all oxygen groups is hard to achieve. Some of the oxygen groups have the tendency to remain, as different functional groups bind to GO with different affinities. Edge groups (carboxyl groups) are known to remain, while those on the basal plane are more easily removed (hydroxyl and epoxide groups). The remaining groups can alter the initial properties of graphene, in terms of electrical conductivity, doping levels, band gap, etc. As graphene obtained by reduction often contains oxygen groups, it is better to use the term *reduced graphene oxide* rather than just *graphene*.[58].

Successful GO reduction can be easily visualized since an effective color change follows the reduction process. Figure 1.8 shows the optical images of GO/rGO film (deposited onto a polyethylene terephthalate (PET) substrate), solution, and sheets deposited on SiO_2.

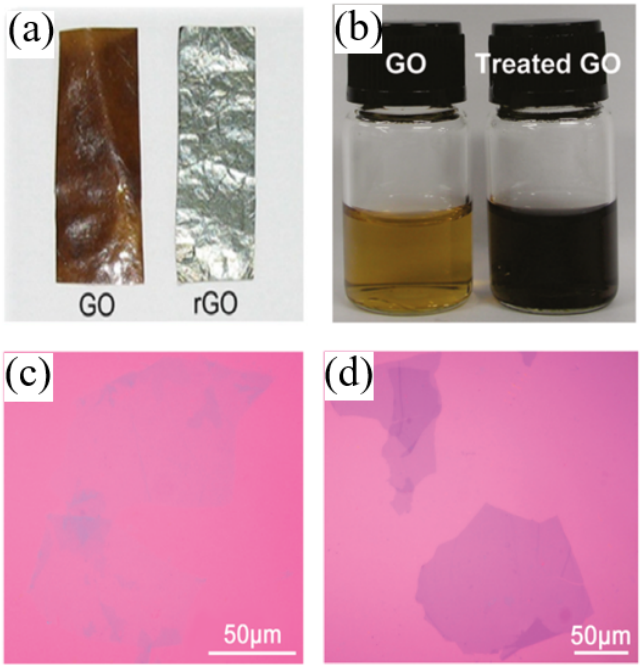

Figure 1.8: Optical images of GO/rGO a) film on the PET substrate, b) solution and sheets on SiO_2 substrates c) before and d) after reduction.[59;60;61].

After reduction, the dark-brown GO film (Figure 1.8 a.) becomes a film with a metallic luster, indicating improved reflection of the incident light.[59] Solution-processed yellow-brown GO (Figure 1.8 b.) turns into a dark-brown rGO solution, with increased precipitation due to the hydrophobic character of rGO. In the case of GO/rGO on the SiO_2 substrates (Figure 1.8 c. and d.), the contrast with the substrate is higher for conductive rGO than for insulating, practically transparent GO sheets. In the next section, some of the reduction methods frequently used in the GO treatment will be described.

Chemical treatment

Chemical treatment involves the use of chemical agents able to remove the oxygen groups present on GO's surface. The advantage of these methods is the low cost for high-volume production of chemically modified reduced GO.[62] Furthermore, subsequent processing is accessible, since the chemical reduction is a solution-based method. Some of the chemical reagents used for this purpose are: hydrazine, dimethyl hydrazine, $NaBH_4$, hydroquinone.[63] The use of pure hydrazine[64] with heating step which promotes the reduction reaction or use of hydrazine vapors[65] are widely used techniques for GO

reduction. However, hydrazine is known as highly toxic for human health and the environment and should be handled with great precaution. With this in mind, researchers tried to replace hydrazine with eco-friendly and less hazardous chemicals.

An important component of healthy human nutrition was shown as a promising candidate for GO reduction: ascorbic acid (vitamin C). Fernandez-Morino et al. compared the efficiency of different reducing agents (potassium hydroxide, pyrogallol, sodium borohydride, hydrazine monohydrate) with ascorbic acid.[66] A maximum decrease in oxygen groups on GO were observed when using ascorbic acid or hydrazine, compared to other agents. Electrical conductivities of rGO in both cases were also comparable, making ascorbic acid as efficient as hydrazine with the main advantage of being innocuous.

The main drawback of this method is the difficulty in removing chemical reagents after the reduction step, as residual chemical reagents can alter the rGO's properties. Other eco-friendly methods for GO reduction are thermal and electrochemical reduction.

Thermal treatment

Exposure of GO to elevated temperature ($1600 - 2000$ °C) under inert atmosphere (argon flow) was shown to successfully eliminate the oxygen groups.[67] There is an effective rearrangement of different $C-O$ groups into the graphene-like initial structure. Also termed "chemical disproportionation", this treatment results in CO and CO_2 by-products.[68] During the release of CO_2, graphene sheets suffer from structural distortion and damage. Decomposition of chemical groups also affects and removes carbon atoms from the GO plane, leaving defects in the lattice.[59]

Electrochemical treatment

Electrochemical reduction is probably one of the most convenient methods for GO reduction, since it does not involve the use of harsh chemical agents nor high temperatures, unlike the thermal reduction method. Production of rGO by this method can be performed using a one-step or a two-step approach.[69]

In a one-step approach, reduction is performed in a conventional three-electrode electrochemical cell, from the collodial dispersion of GO in water in the presence of an electrolyte (usually phosphate-buffered saline: PBS). During the reduction process, a thin film of GO is deposited on the working electrode surface (usually macroscopic glassy carbon or gold electrode).

A two step approach requires previous deposition of GO on the surface of the desired electrode using deposition methods like dip-coating or drop-casting. The electrochemical reduction step is performed using cyclic voltammetry (CV), linear sweep

voltammetry or by chronoamperometry.

Guo et al. performed the reduction of GO obtained by exfoliation of graphite oxide.[70] GO deposited on the surface of a glassy carbon electrode (GCE) was reduced by performing cyclic voltammetry in PBS. The cathodic peak at ≈ -1.2 V, as observed in Figure 1.9, suggests the reduction of oxygen groups since the water reduction is expected to occur at more negative potentials.

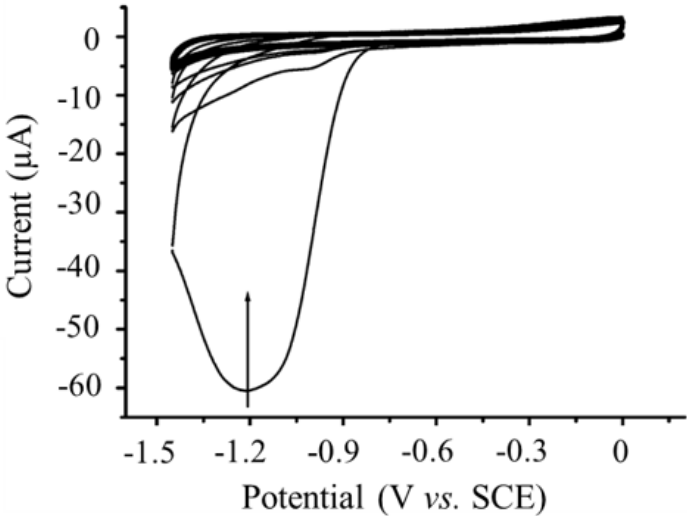

Figure 1.9: Cyclic voltammogram of GO reduction on the surface of a GCE in PBS.[70]

The highly negative potential was necessary to achieve the successful reduction of oxygen-containing groups. The reduction current was observed to decrease with each cycle, which was an indication of fast and irreversible reduction process.

One of the main limitations of this method is the very low yield of produced rGO (solely on the electrode's surface). The thickness of the film is difficult to control as well and may vary from one experiment to another (depending on the deposition technique used), which means that GO which is far from the electrode surface will be partly reduced or not at all. Furthermore, obtained rGO is hard to handle for further use.

In-situ electrochemical reduction techniques are very practical, inexpensive and could be adapted according to research needs. This is convenient in transistor configuration, since the transistor's electrodes could be used as electrodes for the GO's reduction.

Orgiu and co-workers demonstrated an *in-situ* method for obtaining rGO directly on the bottom contact structure of a field-effect transistor.[71]. By applying a voltage between pre-patterned source-drain gold contacts they achieved selective reduction of GO, making it possible to engineer rGO layers on the nanoscale directly on the device, avoiding the post-patterning step. The same group also demonstrated the possibility to locally pattern rGO using a tip of conductive atomic force microscopy (C-AFM).[72]

Samori et al. performed an *in-situ* GO electrochemical reduction using the short-

circuited source-drain gold contacts as the working electrode and an outer Au plate as a counter/reference electrode, schematically represented in Figure 1.10.[5]

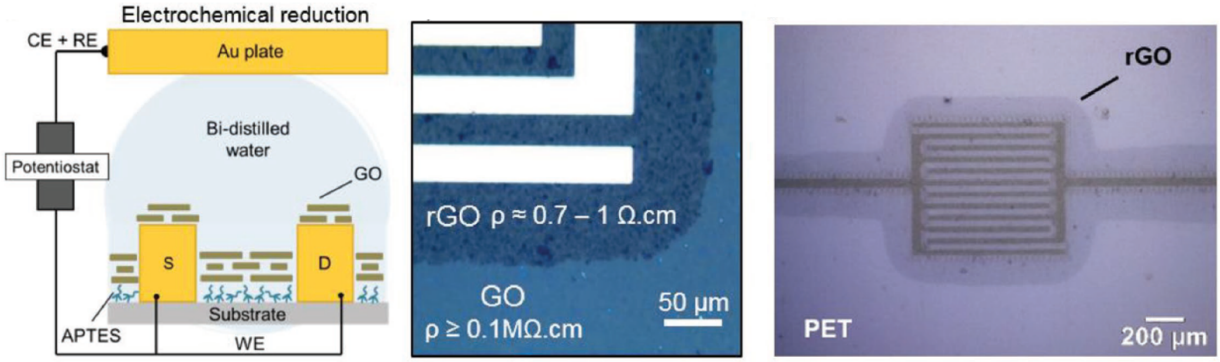

Figure 1.10: (a) Electrochemical reduction setup. (b) Optical image of rGO/GO film with the respective values of electrical resistivities. (c) rGO on the flexible substrate.[5]

By performing a few voltammetric cycles (1-4) from 0 to −2.8 V in bidistilled water, the rGO thin film was obtained on the interdigitated transistor's structure. The method was feasible on both rigid (SiO_2, Figure 1.10 b.) and flexible substrates (PET, Figure 1.10 c.).

Faucett et al. conducted a study of the GO voltage-induced reduction process across gold electrode pairs.[73] By applying a bias of 5 V, an *in-situ* study using optical microscopy revealed a time-dependent growth of rGO filaments across the electrode gap. As shown in Figure 1.11, the growth of rGO film was found to occur on the opposite side of the applied electrical field.

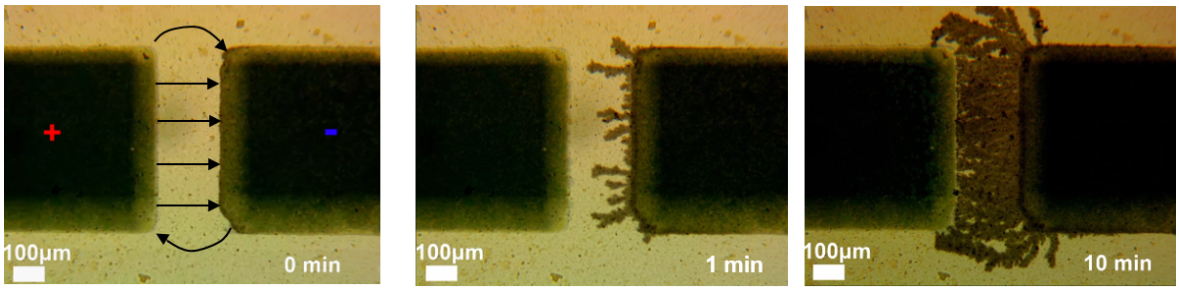

Figure 1.11: *In-situ* optical microscopy of rGO progressive growth across gold electrode pairs. The arrows show the electric field's direction.[73]

Also, the growth progressed with increased reduction time. The gap between the two electrodes was completely filled with rGO film after 10 minutes of applied bias. The authors also showed that the rGO growth was conducted by the electrical field, regardless of the geometry of electrodes used. This work demonstrates that the reduction process of GO is very time-dependent. Moreover, the rGO's electrical properties could be easily triggered in an environmentally friendly way.

The advantage of electrochemical reduction methods compared to other aforementioned reduction methods is the better control of the reduction process. As previously mentioned, complete removal of oxygen groups from the GO surface is hard to achieve and it is still a topic of research. For further applications of rGO in electronic devices, understanding of the reduction process is crucial.

The work of this thesis partly relies on an electrochemical reduction of GO into rGO for some further applications, which will be discussed later in Chapter 3. In the following section, we will take a closer look at graphene's peculiar properties.

1.3 Physical properties of graphene

Why does graphene attract such scientific attention? The answer can be found in its unusual mechanical, optical, thermoelectrical, thermal and electrical properties. Moreover, graphene's stability in two dimensions defies the solid physics theorem defined by Mermin-Wagner, according to which long-range order in $2D$ crystal lattice cannot exist[c] at any finite temperature.[74;75]

Novoselov et al. have investigated different $2D$ materials isolated from the most strongly layered materials which remained stable under ambient conditions and without any degradation during a long period of time (weeks).[76] Among investigated $2D$ materials ($Bi_2Sr_2CaCu_2Ox$, MoS_2, $NbSe_2$, BN and graphite) graphene exhibited the best electrical conductivity with a charge mobility up to 5000 $cm^2\ V^{-1}s^{-1}$. Lee et al. investigated the mechanical properties of free standing graphene membranes under nanoindentation using an AFM tip.[77] Their experimental results showed graphene as the strongest material ever measured, with a Young's modulus of 1 TPa and breaking strength of 42 N m^{-1} which demonstrates at the same time its intrinsic strength. Compared to steel, graphene has 200 times greater breaking strength. What is the secret of all these amazing properties? The answer lies in graphene's peculiar electronic properties.

Electronic band structure as well as the Brillouin zone of graphene were described in 1946 by Wallace using the band theory of solids under the nearest neighbor tight binding approximation.[78] Graphene's honeycomb lattice can be observed as two interpenetrating triangular lattices with carbon atoms in their bases, represented in Figure 1.12 (left).[79]

[c]N.B. Perfect $2D$ sheets of graphene are always placed on a rigid substrates, thus the overall system is $3D$.

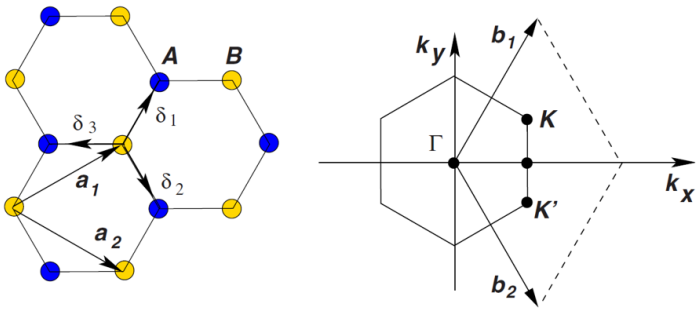

Figure 1.12: Left: Graphene's lattice structure with its parameters. Right: Lattice in reciprocal space, first Brillouin zone with the lattice vectors (b_1, b_2). K and K' are high symmetry points located at the edges of the Brillouin zone centered in Gamma.[79]

Each carbon atom possesses three neighboring carbon atoms, which is the case for each sub-lattice (A and B) leading to overall sp^2 hybridization. Lattice unit vectors are defined as:

$$\vec{a_1} = \frac{a}{2}\,(3, \sqrt{3}),\ \vec{a_2} = \frac{a}{2}\,(3, -\sqrt{3}) \tag{1.1}$$

where $a = 1.42$ Å is the distance between two carbon atoms and the next nearest neighbors vectors are:

$$\vec{\delta_1} = \frac{a}{2}\,(1, \sqrt{3}),\ \vec{\delta_2} = \frac{a}{2}\,(1, -\sqrt{3}),\ \vec{\delta_3} = -a\,(1, 0). \tag{1.2}$$

The reciprocal lattice vectors (Figure 1.12, right) are:

$$\vec{b_1} = \frac{2\pi}{3a}\,(1, \sqrt{3}),\ \vec{b_2} = \frac{2\pi}{3a}\,(1, -\sqrt{3}) \tag{1.3}$$

In the reciprocal space, the first Brillouin zone of hexagonal shape (Figure 1.12, right) is described by three points: Γ representing the center of the Brillouin zone, K and K' which are the high symmetry points located at the edges, the so-called "Dirac points".

Figure 1.13 represents the calculated band structure of graphene. One can notice that in each Dirac point the conduction band meets the valence band, thus leading to a zero-energy gap between them. This particularity defines graphene as a semi-metal. Besides, there is a linear energy dispersion in graphene in the Dirac points' vicinity, within an energy range of roughly 1 eV.[80] In this region, the effective mass of charge carriers (electrons and holes), which is proportional to the inverse of the energy band curvature, is thus theoretically null. The behavior of charge carriers can be described here as massless fermions which propagate at velocities close to that of light.[81]

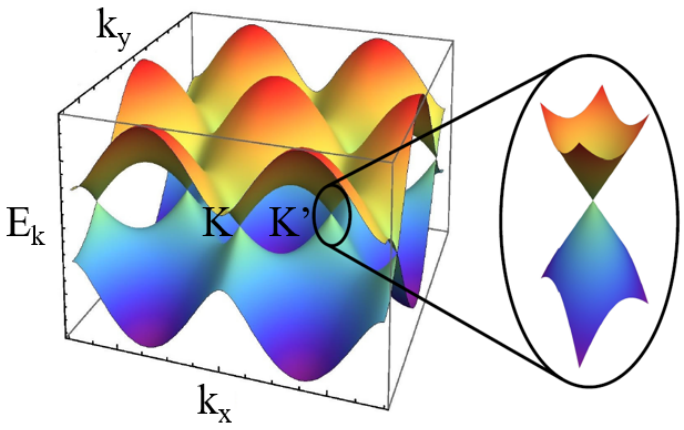

Figure 1.13: Graphene's band structure represented with corresponding energy and momentum axes. The Dirac cones at the edges of Brillouin zone are shown enlarged.[82]

These relativistic particles obey the Dirac energy dispersion law:

$$E = \pm \hbar v_F |k - K| \tag{1.4}$$

where v_F is the Fermi velocity ($v_F \approx 10^6$ m s^{-1}) and $\hbar$ is the reduced Planck constant.[83]

Jin et al. investigated the GO's band gap behavior at different oxidation rates[84]. The graphite precursor was oxidized using the Brodie's modified method for different durations (ranging from 5 to 60 minutes) and then exfoliated by sonication to obtain GO. Obtained band gap values (calculated from UV-visible spectra) were shown to vary from 1.7 eV to 2.1 eV for 5 and 60 minutes of oxidation, respectively, as shown in Figure 1.14.

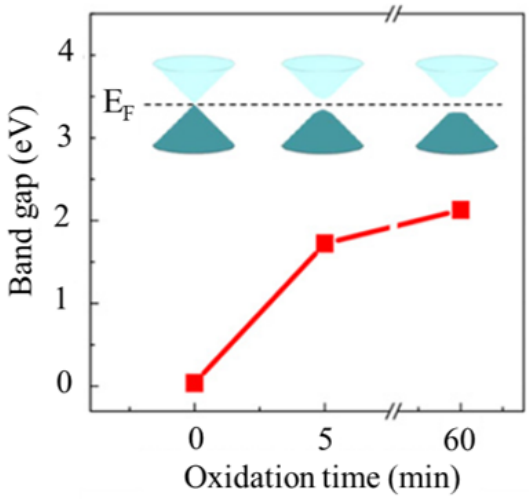

Figure 1.14: Variation of GO's band gap as a function of oxidation time.[84]

The band gap presents a strong relation with the atomic O/C ratio (quantity of

oxygen groups). Also, the more GO was oxidized, the more sp^3 hybridization was observed. Theoretical calculations by Lian et al. demonstrated that the band gap values are also affected by the respective oxygen groups' adsorption position on GO.[85] These results show that the GO's electronic properties are strongly correlated to the synthesis conditions (GO's oxidation degree). The position of Fermi level for pristine graphene represents the energy position of the Dirac point which is around −4.5 eV.[86] Knowing that the density of states near the Fermi level's position is very low, graphene is susceptible to change its electronic properties (hole transport *vs.* electron transport) due to several factors[81]: intrinsic structural defects (e.g., vacancies, grain boundaries, wrinkles) or extrinsic impurities, chemical doping caused by the intercalation or adsorption of ions or molecular species of high charge density and electronic corrugations, i.e. local variations in the charge density (evidenced by scanning tunneling microscope, STM[87]).

The defects can be intentionally introduced by different methods: bombardment of graphene's surface with electron/ion beam, hydrogenation, fluorination, oxidation (hybridization changes from sp^2 to sp^3).[88]

Furthermore, the charge carrier density can be additionally modulated by using an external magnetic or electric field. The metallic behavior of graphene is shown to be present even at high magnetic fields and at low charge carrier concentrations (near charge neutrality point).[89] From quantum hall measurements, the charge carrier densities and charge carrier mobilities can be calculated with the values ranging from $10^{11} - 10^{13}$ cm^{-2} and up to 10^4 cm^2 V^{-1} s^{-1}, respectively.[90]

The research group awarded for the graphene discovery, also showed that the graphene's conductivity and Fermi level position can be modulated using capacitive effects.[91]

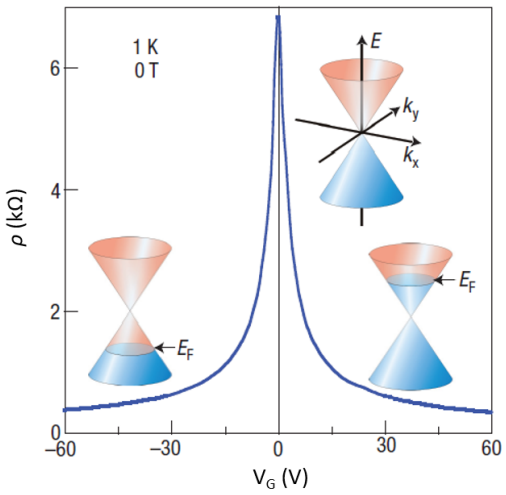

Figure 1.15: Electrical resistivity ($\rho = \frac{1}{\sigma}$) of graphene as a function of applied gate voltage recorded in multiterminal Hall bar device on SiO_2/Si substrate. Insets show the respective Fermi level positions.[92]

This was performed by variation of the applied gate voltage in a field-effect device. As observed in Figure 1.15, the highest resistivity was obtained at zero gate voltage ($V_G = 0$ V). Polarizing the gate electrode positively or negatively leads to a lowering of the graphene's channel resistivity. Concerning the Fermi level, its position coincides with the Dirac point position when no gate voltage is applied ($V_G = 0$ V). On the contrary, when applied gate voltage was varied ($V_G > 0$, $V_G < 0$), the position of the Fermi level was observed to vary too. These amazing properties of graphene opened another field of research which is the study of graphene in field-effect transistors configuration. Some of the latest research work in this field will be discussed in the following section.

1.4 Graphene field-effect transistors (GFETs)

The working principle of a field-effect device is based on the electronic properties control of the transistor's active material (representing the device channel) upon modulation of the electric field, performed by gate polarization. Novoselov et al. first demonstrated the working principle of the Graphene Field-Effect Transistor (GFET).[1] Considering the peculiar properties of graphene, which we have discussed, it is not surprising that its use in electronic devices such as GFET is one of the "hot topics" across the scientific community. Graphene's chemical structure makes it sensitive to any change in its electronic environment (e.g., change of pH, binding of molecules). The possibility of modulating graphene's conductivity through an external electric field, which could originate from a charged molecule, is considered as a reliable mechanism for sensing applications.[93] As the work in this thesis is based on the study of graphene's properties in a field-effect transistor configuration, we will take a look at different GFET structures, their working principles as well as the applications of GFETs in the sensing field.

1.4.1 GFET structures

A field-effect transistor consists of three electrodes: source, drain and gate. The distance between source and drain (S/D) electrodes defines the transistor's channel length. The channel is physically decoupled from the gate electrode by a dielectric layer. The study of graphene's electronic properties can be performed in different FET configurations. Figure 1.16 shows different GFET configurations when the dielectric is in the solid state.

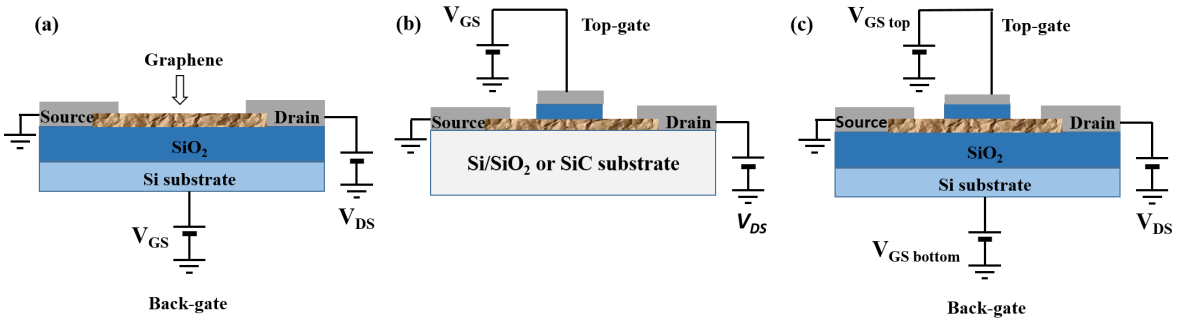

Figure 1.16: Structures of graphene-based field-effect transistors: a) back-gate, b) top-gate and c) dual-gate structure.

Back-gate structure. In the first back-gated GFET, doped Si/SiO_2 was used as the substrate where SiO_2 acted as the dielectric. The polarization of graphene was performed by applying a voltage on the doped Si substrate, located beyond the graphene/SiO_2 supporting layer. Figure (1.16 a.) shows the scheme of a back-gate structure. The thickness of SiO_2 used in the back-gate configuration is usually in the range of $90-300$ nm. Due to the important thickness of the dielectric and its low dielectric permittivity, one should apply significant gate voltages (several tens of volts) to polarize graphene.

The main drawback of the back-gate structure is the occurrence of a leakage gate current. Since the whole substrate is polarized, any contamination (e.g., improper graphene channel shaping; residual graphene at the substrate edges) could result in a gate current leakage. That means that the gate current could mask the current coming from the drain if the device is not properly fabricated.

Top-gate structure. The first top-gated GFET (Figure 1.16 b.) was described by Lemme et al. in 2007.[94] In this work, Ti/Au electrodes (defined by e-beam lithography) were used as the S/D contacts along with the gate on the top of the graphene layer, supported by SiO_2 substrate. The gate was composed of SiO_2, Ti and Au. When the device was probed with a back gate, the charge carriers mobilities were estimated to be $\mu_h = 4790$ cm^2 V^{-1} s^{-1} and $\mu_e = 4780$ cm^2 V^{-1} s^{-1} for holes and electrons, respectively. On the other hand, the charge mobilities recorded in the case of a top-gate structure had lower respective values of $\mu_h = 710$ cm^2 V^{-1} s^{-1} and $\mu_e = 530$ cm^2 V^{-1} s^{-1}. The presence of "standard" gate on graphene was found to reduce both holes and electrons mobilities, probably due to decreased overlap of π orbitals in graphene. Xia et al. proposed the use of an organic seed layer (a derivative of polyhydroxystyrene) between the graphene and a dielectric, to decrease scattering and preserve the intrinsic properties of graphene.[95]

Dual-gate GFETs. The combination of a back-gate and a top-gate (Figure 1.16 c.) was reported as well.[96] Huard et al. used PMMA as a dielectric layer for the top gate along with the Ti/Au contacts and the doped Si substrate as a back gate.[97] As they reported, a tunable potential barrier in graphene was created, where the back-

gate voltage was able to tune the charge carriers in the bulk of the graphene sheet. In contrast, the top-gate voltage tuned the surface charge carriers, located just beyond the gate.

Electrolyte-gated GFET (EG-GFET). The configuration mainly used in this thesis is the electrolyte-gated graphene field-effect transistor configuration (EG-GFET). In a liquid-gated configuration, the graphene and the metallic gate are separated by an electrolyte. Here, the electrolyte covering the surface of graphene acts as a dielectric and replaces a solid one. When a potential is applied to the gate, graphene is polarized through the means of interfacial capacitances. The charge behavior during the polarization process can be described using a Helmholtz model. More precisely, as schematically represented in Figure 1.17, when a positive potential is applied to the gate, the accumulation of negative charges coming from the diffuse layer will take place at the gate surface, forming the so-called Helmholtz layer.

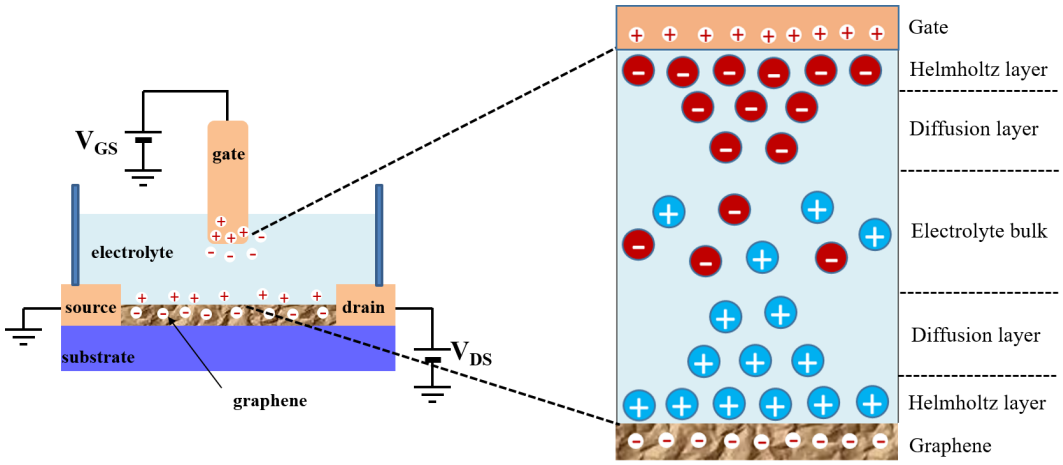

Figure 1.17: Schematic representation of an EG-GFET configuration and the formation of two electrical double layers.

At the same time, the electrons will accumulate in the graphene channel. This gives rise to the formation of two electrical double layers (EDL): one at the gate/electrolyte interface (associated to a capacitance named here as C_1) and another at the electrolyte/graphene interface (associated to a capacitance C_2). The gate/graphene capacitive coupling, caused by the double layer formation, may be modeled as two plate capacitors in series:

$$\frac{1}{C_{\mathrm{EDL}}} = \frac{1}{C_1} + \frac{1}{C_2} \tag{1.5}$$

The distance between the metal (gate or graphene) and the adsorbed ions defines the thickness (d) of the electrical double layer (often called *Debye length*) and is related to the C_{EDL} by the following equation:

$$C_{\mathrm{EDL}} = \frac{\varepsilon}{d} \tag{1.6}$$

where ε represents the electrical permittivity of the electrolyte. As observed from the equation 1.6, the electrical double layer capacitance is not dependent on the gate potential applied. A voltage drop is considered negligible across the diffusive layer of electrolyte, while at the gate/electrolyte and electrolyte/graphene interfaces, the voltage drop is more important, as shown in Figure 1.18.

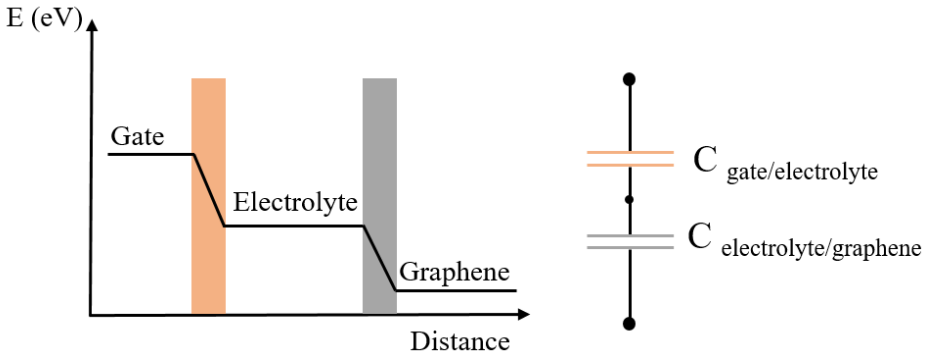

Figure 1.18: Left: Schematic representation of voltage drop across two interfaces of an EG-GFET. Right: Capacitor series model used to describe the contribution of each interface to the capacitive coupling between the gate electrode and the electrolyte due to the double layer formation.

The modification of one of these two interfaces (e.g., graphene or gate functionalization) will result in a significant impact on the effective field-effect. This property of EG-GFET is largely used in the sensing field, which will be discussed later.

The formed double layer is very thin, approximately 1 nm. Compared to back-gate configuration, where the interfacial capacitance is in the order of nF cm^{-2}, the interfacial capacitance in the electrolyte-gated configuration is much higher: in the μF cm^{-2} range. Consequently, the operating voltages for an EG-GFET are in the range of 1 V. Due to the use of low voltages, it is considered that no parasitic electrochemical processes will take place, leading to purely capacitive interfaces.[93]

Also, one should keep in mind that the density of states (DOS) near the Fermi level energy (E_F) in graphene is very low compared to the metal where the DOS at E_F is quite large. Consequently, for the charge introduction in graphene, the E_F should be shifted while in the case of metal there is almost no shift in E_F.[98] This gives rise to another intrinsic property of graphene itself: the so-called *quantum capacitance*(C_Q). The quantum capacitance depends on the charge carrier concentration $n = \sqrt{\frac{e V_{GS}}{\hbar v_F \sqrt{\pi}}}$ induced by the gate potential and charged impurities[99] (e represents electron charge, V_{GS} is the applied gate-source potential, $\hbar$ is reduced Planck's constant and v_F is the Fermi velocity in graphene $|v_F| = 1.1 \times 10^6$ m s^{-1}). While in the case of a back-gated GFET, the C_Q is always neglected (due to the low capacitance of SiO_2), in the EG-GFET the C_Q is in the same order of magnitude as the interfacial capacitances and has to be taken into account when calculating the total capacitance value. Therefore, the

total capacitance between the gate electrode and the graphene layer in the EG-GFET configuration (C_{TOT}) can be calculated by summarizing the two types of capacitances mentioned:

$$\frac{1}{C_{TOT}} = \frac{1}{C_{EDL}} + \frac{1}{C_Q} \tag{1.7}$$

The main electrical characteristics of graphene in the GFET configuration will be discussed in the following subsection.

1.4.2 Electrical characterization of GFETs

The typical measurement of graphene's electrical properties in the field-effect configuration consists in recording the transistor's current when a certain voltage is applied: current-voltage (I-V) characteristics. Two types of electrical characteristics can be obtained: the output curves and the transfer curves.

Output characteristics. Output GFET curves represent the drain-source current (I_{DS}) obtained upon the sweep of drain-source voltage (V_{DS}), for a fixed gate-source voltage (V_{GS}) value.

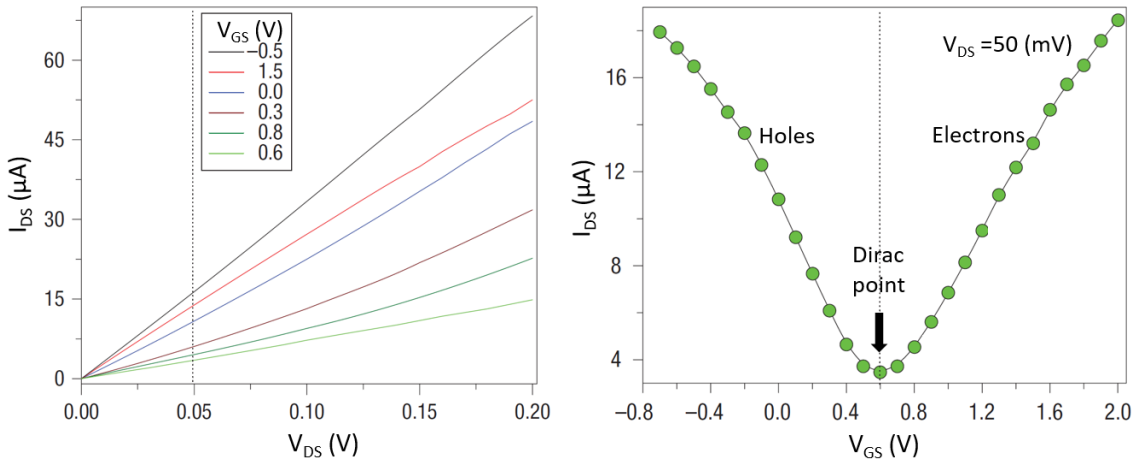

Figure 1.19: Output curves (left) recorded at different gate voltages in EG-GFET configuration and the corresponding transfer curve (right).[100]

Figure 1.19 shows an example of the typical output curves (left) and corresponding transfer curve (right), taken from the literature.[100] The observed current change upon the gate voltage variation is proof of the field-effect presence in the device. The trend of current for the output curve follows the transfer curve trend. Output curves are linear curves with no current saturation observed attesting for the absence of Schottky barriers at the graphene/electrode interface.[100] Compared to MOSFET transistors where two regimes are observed in the output characteristics (saturation and linear regime), the GFET transistors have only linear regime which is a consequence of zero band gap in graphene.

Transfer characteristics. Graphene FETs are characterized by a unique shape of the transfer curve, corresponding to the drain-source current recorded upon the sweep of the gate-source voltage. Drain-source voltage is kept constant while the source is grounded. The V-shaped transfer curve comprises two branches (Figure 1.19, right), separated by the minimum current point. The left branch represents the *holes* as the main charge carriers in graphene, theoretically obtained when the gate is negatively polarized. On the other hand, the right branch of the transfer curve represents the *electrons* as the channel's main charge carriers (positive gate polarization). Due to the conical shape of the electronic band structure in graphene, charge flows subsequently from holes to electrons, which is indicated as ambipolar behavior. Ambipolar transistor behavior is a fingerprint for graphene-based materials. The transition point between the hole and electron branch is called *charge neutrality point* (CNP)[d], which corresponds to the channel's minimum conductivity found at the Dirac point in the band structure of graphene (mentioned above).

ON/OFF ratio. Another consequence of the zero band gap is that the transistor cannot be turned off. The minimum current point observed in the transfer curve represents the transition between two different types of charge carriers. However, when the ON/OFF ratio has to be defined, the current in CNP is taken into account as the minimum current in the system (I_{OFF}). The maximal current in one of two branches is taken as I_{ON}. The ON/OFF ratio observed on transfer curve in Figure 1.19 (right) is about 10.

Extraction of charge mobility

The extraction of electrical parameters such as charge carriers mobility is usually performed through Hall measurements (as mentioned) or through measurements in the FET configuration, in which we are interested. Different methods based on the FET measurements exist, such as the transfer length method (TLM) or direct transconductance method (DTM). Zhong et al. investigated and compared these methods.[101] The TLM method was shown as one of the most accurate methods since the contact resistance effect of the graphene/metal interface is eliminated, enabling precise extraction of mobility values at high carrier densities. The main disadvantage of this method is its complexity since the fabrication of graphene devices with different channel lengths and high uniformity is needed for the extraction of contact resistance.

The DTM method is one of the simplest methods since mobility extraction can be performed directly from the transfer curve characteristics using the following relation:

$$g_m = \frac{\partial I_{\mathrm{DS}}}{\partial V_{\mathrm{GS}}} = \mu \times C_{\mathrm{TOT}} \frac{W}{L} V_{\mathrm{DS}} \tag{1.8}$$

[d]CNP because at one moment the existence of two types of charge carriers at the same time will take place in graphene.

where g_m is the transconductance, μ is the charge carrier mobility and $\frac{W}{L}$ is the channel aspect ratio (W represents the transistor's channel total width and L channel length). This equation represents, at the same time, the charge transport model of FET in the linear regime.[102] However, this method does not consider the contact resistance, which is the main reason why the calculated mobility is always lower than the expected real mobility.[101] Besides, the mobility values depend on the conduction type, channel length and the applied gate voltage.

Another approach to calculate the charge mobility is using the Drude model, where the long range interactions between the electrons are neglected[103]:

$$\mu = \frac{\sigma}{n\,e} \tag{1.9}$$

σ represents the conductivity, n is the charge carrier density and e is the elementary charge. As observed from equation 1.9, this model yields the mobility variation as a function of the charge carrier density. This relation is valid only for high charge carrier densities.

Das et al. calculated the mobilities using the Drude model for the back-gated and electrolyte-gated structure.[100] Figure 1.20 shows the obtained mobility *vs.* charge carrier concentration.

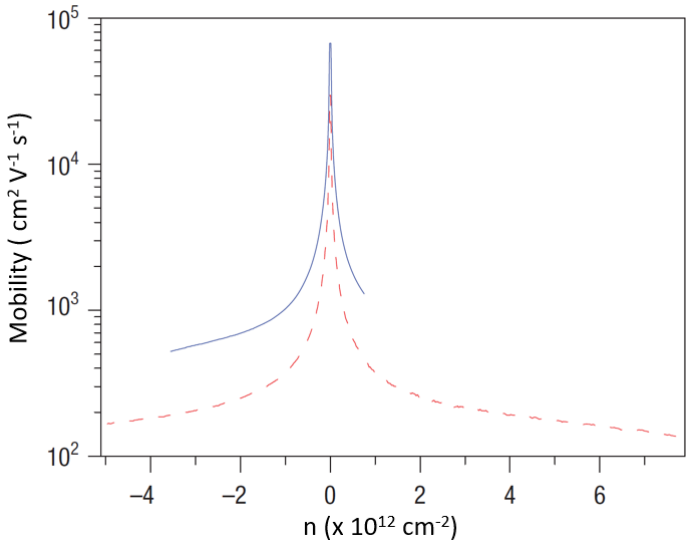

Figure 1.20: Charge carrier mobility as a function of charge carrier density for an electrolyte-gated (dashed red line) and back-gated configuration (blue line).[100]

The charge carriers mobilities in the liquid gated structure were found to be lower than in the case of a back-gated structure. The creation of charged impurities due to the addition of an electrolyte was mentioned as one of the explanations. These charged impurities act as scattering centers, resulting in a decrease of observed charge mobility. The Drude model was used for the mobility extractions in this work, which

will be discussed in Chapter 3. In the following subsection, the control of graphene's electronic properties through molecular functionalization will be discussed as well as its detection in the GFET configuration.

1.4.3 Graphene functionalization

Depending on the research needs and the application, different approaches of molecular functionalization can be undertaken. Graphene can be functionalized to obtain better solubility or better reactivity. As one part of this thesis is based on the study of doping effects in graphene, we will take a more in-depth look at the functionalization of graphene for band-gap opening and the doping purposes.

Graphene doping

Graphene can be functionalized through the means of covalent (chemisorption) or non-covalent interactions (physisorption). Physisorption is considered as a mild way to functionalize graphene, as its properties and structure are not affected. The main drawback of the non-covalent approach is weak molecular adsorption. On the other hand, modification of graphene's electronic properties using the covalent means is more robust than the non-covalent approach. The bond formation between the adsorbate and a graphene plane induces a change from sp^2 to sp^3 hybridization, which directly influences graphene's unique electronic band structure.[104]

A molecular dopant can be an acceptor or donor of electrons, according to the position of its HOMO/LUMO (highest occupied/lowest unoccupied molecular orbital position) with respect to graphene's Fermi level, schematically represented in Figure 1.21.

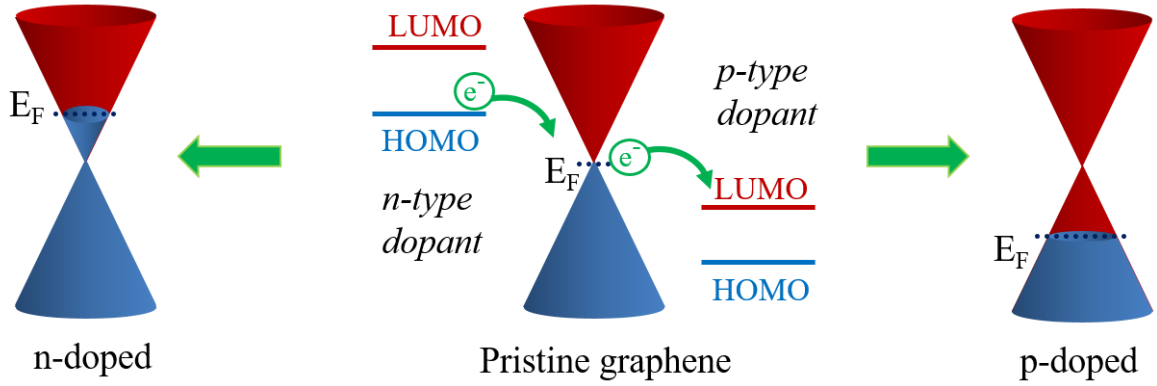

Figure 1.21: Schematic representation of HOMO/LUMO position of doping molecule with the respect to the position of graphene Fermi level.

Two cases are possible:

1. The HOMO level of the doping molecule is higher than graphene's Fermi level. In this case, electrons may flow from the molecule to graphene, which becomes n-doped. The Dirac point is situated below the Fermi level.

2. The LUMO level of the doping molecule is lower than graphene's Fermi level. In this case, electrons may flow from graphene to the accepting molecule. Having lost a part of its electrons, graphene becomes p-doped and the Dirac point is situated above the Fermi level.

These effects can be followed through electrical characterizations in the GFET structure. For pristine graphene, the Fermi level and the Dirac point lie at the same energy. Therefore, the CNP position on the transistor's transfer characteristics is expected at $V_{GS} = 0$. The presence of either charged impurities or dopants in the graphene's vicinity will move the CNP toward positive or negative gate potentials. This effect and the control of graphene's electronic properties through covalent and non-covalent functionalization will be discussed in the following text.

Covalent approach

One of the most used methods to tune graphene's electronic properties through the covalent approach is graphene oxidation, described above. On the other hand, one can perform the introduction of a single type of atom in graphene lattice. The advantage of a single atom use is the modification of graphene lattice structure on the local, well-controlled level. Among different atoms that could be potentially used for graphene doping, nitrogen was showed to be an excellent candidate since its atomic size is comparable to that of carbon.[105] On the other hand, nitrogen electronic configuration with five valence electrons allows for the formation of a covalent bond with carbon atoms. The introduction of nitrogen atoms is achieved by nitrogen-plasma exposure, where the doping percentage can be easily controlled by adjustment of the exposure time.

Joucken et al. investigated the charge transfer in N-doped graphene using STM and scanning tunneling spectroscopy (STS).[106] Graphene grown on SiC was exposed to nitrogen flux generated by radiofrequency plasma source. Figure 1.22 shows the STM image of graphene before (a) and after (b) the nitrogen treatment. A defect-free lattice was transformed into the lattice with many bright features, as revealed by STM. The appearance of the bright features was assigned to the presence of nitrogen and the induced charge transfer between the nitrogen and carbon atoms. Outside the trigonal patterns observed, (Figure 1.22 b., inset) the graphene lattice structure was preserved, suggesting very locally induced perturbations.

In another study, the authors investigated the doping effects by adjusting the nitrogen exposure time.[107] STS spectra (Figure 1.22 c.) revealed a progressive shift

of the Dirac point (depicted in spectra by the vertical line) with increased nitrogen concentration.

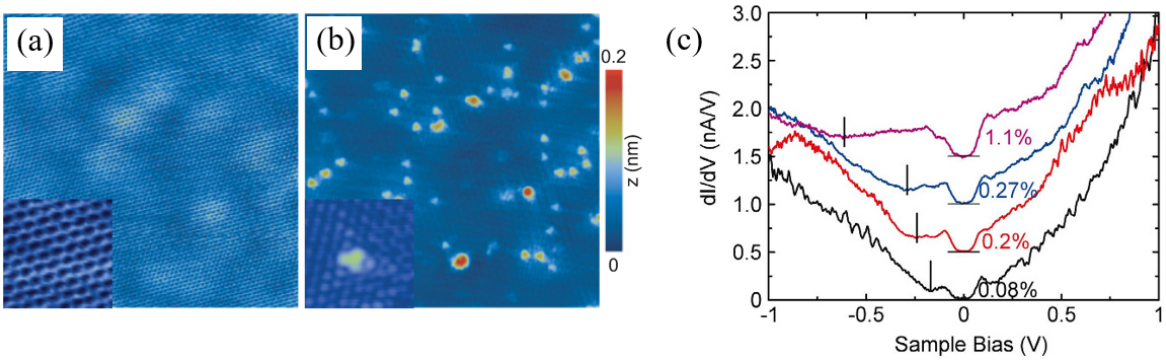

Figure 1.22: STM characterization of pristine graphene (a) before and (b) after N-doping. (c) STS spectra for N-treated samples. The concentration of nitrogen is given below each curve in %. The Dirac point is marked by horizontal lines and vertical lines indicate the points where $\frac{dI}{dV} = 0$.[106;107]

These variations of the Dirac point were attributed to the widening of Dirac cones due to the increased accumulation of electrons in graphene caused by nitrogen presence.

Among different carbon-based materials, graphene possesses the lowest chemical reactivity due to its flat π-conjugated structure. Through the means of chemisorption, graphene's reactivity could be increased. One of the approaches is the covalent attachment of aryl radicals obtained by the reduction of diazonium salts, which can be performed in aqueous solutions of diazonium compounds.[108;109] The radical can attack the graphene plane and form a new bond: C (sp^3)-aryl bond (Figure 1.23).

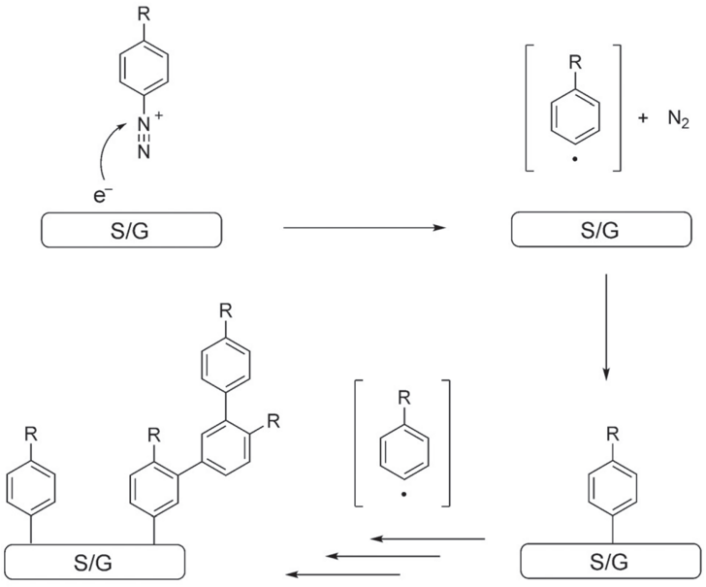

Figure 1.23: Aryl diazonium bonding on a graphene supported by a substrate (S/G).[108]

Furthermore, the functional group (R) located on the aryl group can be an attachment site for further functionalization (e.g., binding of a bio-molecule).

Non-covalent approach.

Graphene's planar structure and extended aromatic system are very accessible for $\pi-\pi$ interactions, which goes hand in hand with a wide range of organic aromatic molecules such as benzene, pyrene, naphthalene. Figure 1.24 schematically represents these kind of interactions.

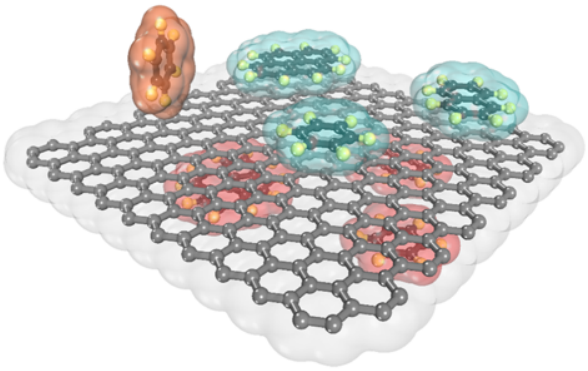

Figure 1.24: Ideal $\pi-\pi$ or C$-$H-π interactions between graphene and aromatic molecules: pyrene, benzene or naphtalene.[48]

Possible CH-π interactions can be present as a hydrogen atom may be found at the graphene edge.

Compared to graphene, rGO has a less π-conjugated system due to the increased number of defects induced by the reduction. However, the type of interactions is still the same as for graphene. Graphene can also interact with some polymers, biomolecules, nanotubes, quantum dots and nanoparticles.[48]

One of the most studied p-type dopants on graphene is tetrafluoro-tetracyanoquinodimethane (F4-TCNQ) shown in Figure 1.25 (left).

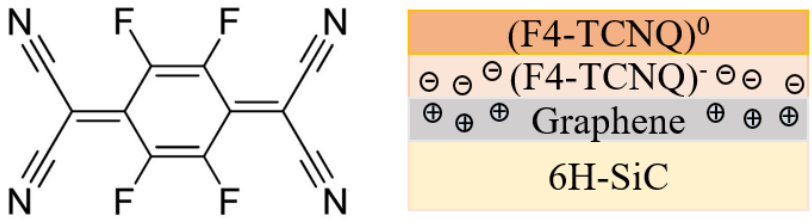

Figure 1.25: Left: Molecular structure of F4-TCNQ. Right: Charge transfer representation at the F4-TCNQ/graphene interface. Adapted from[110].

As F4-TCNQ's LUMO level (-5.2 eV) lies deep below the graphene's Fermi level, a strong charge transfer is expected to take place from graphene to F4-TCNQ. Chen et al. demonstrated for the first time the doping effect of F4-TCNQ on epitaxial

graphene (EG) grown on SiC, by synchrotron-based high-resolution photoemission spectroscopy.[110] The thickness of the studied graphene was about 1-3 monolayers. The deposition of doping molecules was performed by evaporation in a ultrahigh vacuum chamber, and the thickness influence of deposited molecules was studied. The hole concentration in EG was found to be controlled by the presence of F4-TCNQ, since a strong charge transfer took place by the electron withdrawing (electron acceptor) ability of F4-TCNQ. The molecule was found to become negatively charged only at the graphene/molecule interface (Figure 1.25, right). This behavior was compared with C_{60} which is another electron acceptor molecule. With its LUMO position of about -3.7 eV, C_{60} was not able to dope graphene.

Dong et al. investigated the doping effect of different aromatic molecules on single-layer graphene (SLG) obtained by mechanical exfoliation of HOPG.[111] Among others, molecules used were tetra-sodium 1,3,6,8-pyrene tetra-sulfonic acid (TPA) and 1,5 naphthalene diamine ($Na-NH_2$), depicted in Figure 1.26 a. TPA and $Na-NH_2$ were dissolved in deionized water and ethanol, respectively, and subsequently drop-casted on graphene.

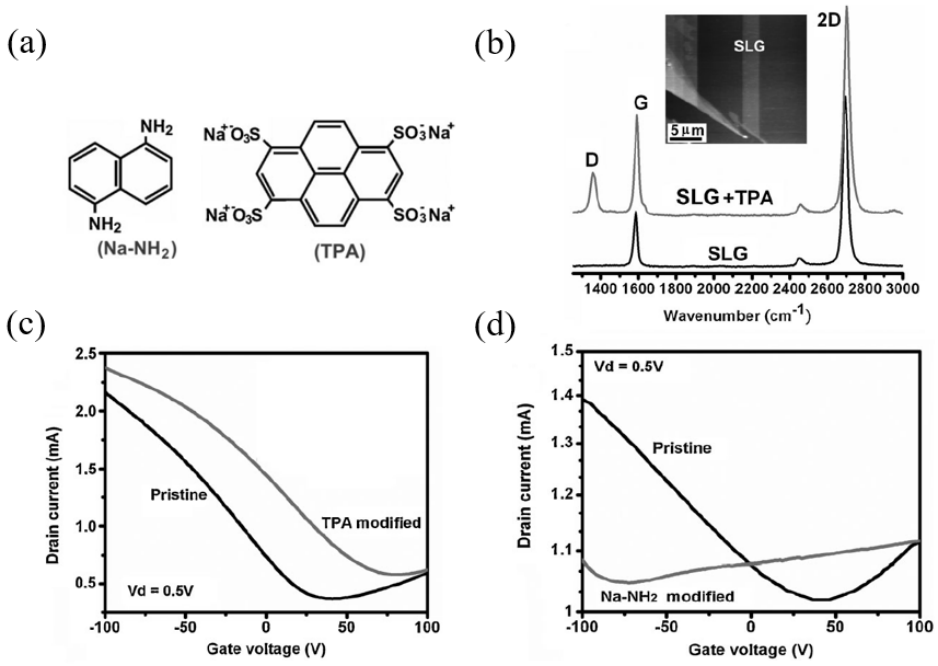

Figure 1.26: a) Aromatic molecules used for graphene functionalization. b) Raman spectra of single layer graphene (SLG) and functionalized graphene (SLG+TPA). Transfer curves of pristine graphene and graphene functionalized with c) TPA and d) $Na-NH_2$.[111]

In Raman spectra (Figure 1.26 b.) the appearance of D band is observed upon the addition of TPA. The TPA induced increased disorder in the graphene basal plane. The ratio of 2D/G bands was also found to change, indicating the existence of doping effects. Doping effects were confirmed through electrical characterizations in the

back-gate transistor configuration, shown in Figure 1.26 (c. and d.) before and after the addition of TPA and $Na-NH_2$, respectively. The transfer curves revealed the initial Dirac point position for pristine graphene at around $V_{GS} \approx +30$ V, suggesting the presence of an initial p-doping. This behavior is commonly observed in the case of electrical measurements performed in ambient conditions due to the moisture and oxygen doping.[112] Upon the addition of TPA and $Na-NH_2$ the Dirac point was found to shift even more toward more positive and negative values, respectively. This shift of the Dirac point position reflected a presence of doping effects induced by the nature of doping molecules: TPA as an electron acceptor induced the p-doping effects and $Na-NH_2$ as an electron donor induced n-doping effects in the graphene layer.

In another approach, De Feyter and co-workers used physisorbed molecular self-assembled monolayers to tune the doping levels in CVD grown graphene.[113] The molecule used for this purpose was oleylamine (OA, Figure 1.27 a.) which possesses an NH_2 functional group serving as an electron donor group. The long alkyl chain is able to self-assemble on graphene.

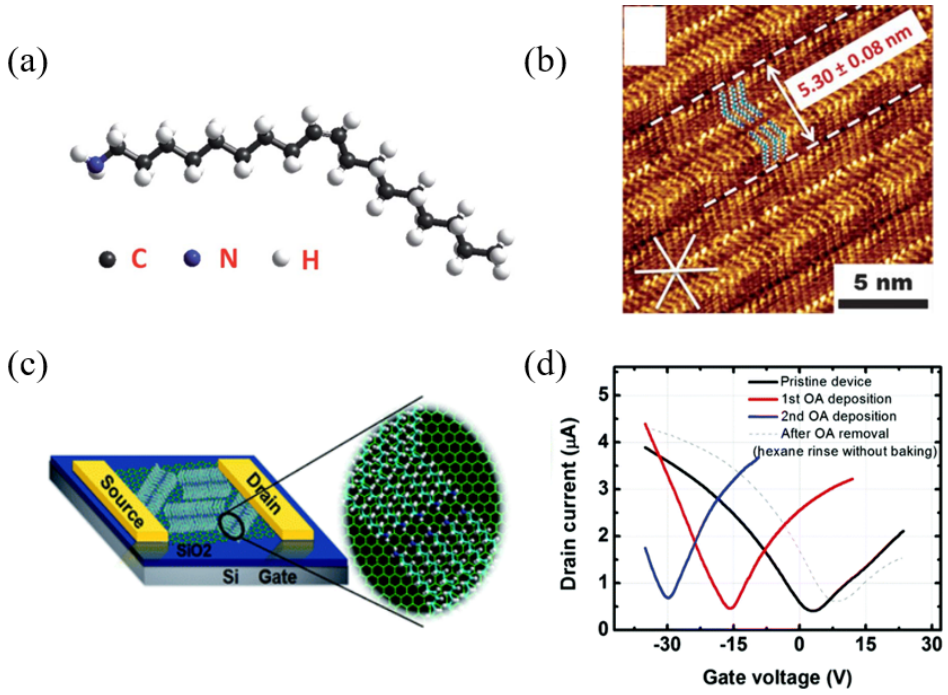

Figure 1.27: a) Oleylamine structure. b) STM characterization of HOPG functionalized with OA. c) Schematic representation of CVD graphene device functionalized wtih OA. d) Transfer curves obtained for pristine device, functionalized graphene and after the removal of OA.[113]

The assembling behavior of OA (dissolved in n-hexane and spin-coated) was studied by the STM technique on HOPG (considered as a "model" substrate since it possesses atomically flat terraces and the underlying layer is another graphene layer). The STM image shows the ordered self-assembled structure of OA, with the boomerang geometry

due to the cis-double bond in the alkyl chain (Figure 1.27 b.). The influence of OA self-assembled on graphene's electronic properties was studied in the back-gate transistor configuration (Figure 1.27 c.). After the deposition of OA and subsequent baking (found to be necessary to promote the interactions OA-graphene), the Dirac point was found to shift (Figure 1.27 d.) from $V_{GS} \approx +3$ V initially to $V_{GS} \approx -16$ V, leading to overall n-doping in graphene (total amount of charge induced by the presence of OA: $\Delta n = 7.4 \times 10^{12}$ cm^{-2}). The spin-coating of another molecular layer was found to introduce more electrons ($\Delta n = 7.7 \times 10^{12}$ cm^{-2}) and further shift the Dirac point position to $V_{GS} \approx -28$ V. Initial properties of pristine graphene were shown to be recoverable upon rinsing the device in hexane. In another work and similar approach with a self-assembled network, the authors tuned the doping effects in graphene by tuning the density of amine groups, which is inversely proportional to the alkyl chain length.[114]

These examples are the evidence of graphene's electronic sensitivity to the presence of dopants. Besides, this characteristic makes graphene a good platform for potential sensing applications, which will be reviewed in the next section.

1.5 Graphene toward sensing applications

The combination of graphene's electronic sensitivity and FET configuration is one of the promising approaches toward reliable sensors. Comparing the two most used structures, a back-gate and a top-gate structure, the top-gate structure has more than three orders of magnitude larger capacitance value than the back-gate structure[115], which was one of the motivations to use EG-GFET in this thesis. Some other advantages of EG-GFET configuration for sensing purpose are[116]:

- The transistor acts as a sensor and an amplifier. Gate voltage and channel current are sensitive to every change at the gate electrode/electrolyte interface and the electrolyte/graphene interface. If the reaction were to occur at the gate surface, it will be amplified by transistor's transconductance.

- Low working voltages of up to 1 V go hand in hand with the integration in wearable electronics and the detection of biological events.

- The device could be easily miniaturized and the transistor channels could be confined into microfluidic systems, which can refresh the analyte flow on the graphene surface.[117]

Some of the examples of EG-GFET applied to (bio)sensing field will be reviewed in the following subsection.

1.5.1 EG-GFET (bio)sensing working principle

For the recognition of a target biomolecule, the graphene surface should be first functionalized with the receptor molecule able to interact with graphene.[93] Figure 1.28 schematically represents the biosensing working principle in the GFET configuration with the corresponding representation of transfer and chronoamperometric curves.

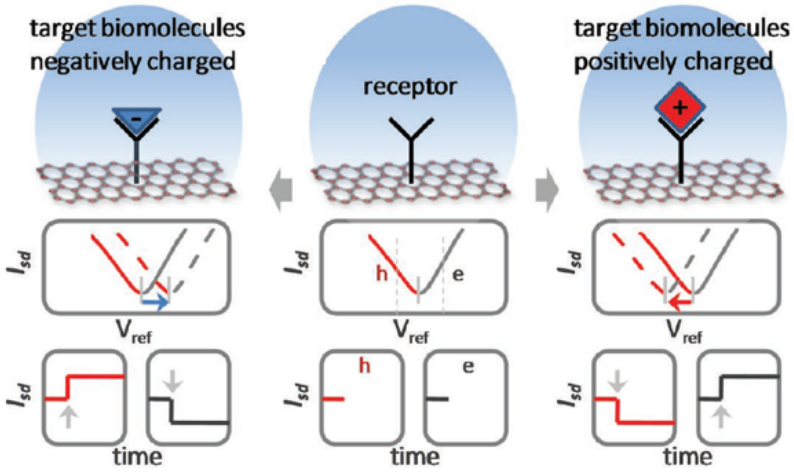

Figure 1.28: Sensing principle in GFET biosensor.[93]

At the starting point, the Dirac point position obtained upon the immobilization of the receptor molecule represents the "reference" position (in volts). Charged biomolecules act as a local gate able to modulate the charge carriers in the graphene channel through a capacitive effect. Negatively charged biomolecules will induce the accumulation of positive charges in graphene, resulting in a shift of the Dirac point position toward more positive gate voltage values. This shift is measured with respect to the "reference" Dirac point position. On the other hand, the positively charged biomolecules will induce a negative shift of the Dirac point gate voltage and the accumulation of electrons. In the chronoamperometric measurements (drain current vs. time), binding of a negatively charged molecule will result in the current decrease and increase for the electron and hole regime, respectively. Inversely, for the binding of a positively charged biomolecule. Graphene's current modulation is directly related to the charge carrier's density change Δn and the total number of immobilized biomolecules N[93]

$$\Delta I_{\mathrm{DS}} = \frac{W}{L} V_{\mathrm{DS}}\, e\, \mu\, \Delta n \propto N \tag{1.10}$$

where e represents the electron charge (1.602×10^{-19} C) and Δn is expressed in cm^{-2}.

One of the recent works by Jin et al. is a demonstration of the biosensing working principle here explained.[118] The authors investigated the specificity of rGO functionalized with ebola virus (EBOV) corresponding antibodies (Anti-EBOV Ab) in the EG-GFET configuration represented in Figure 1.29.

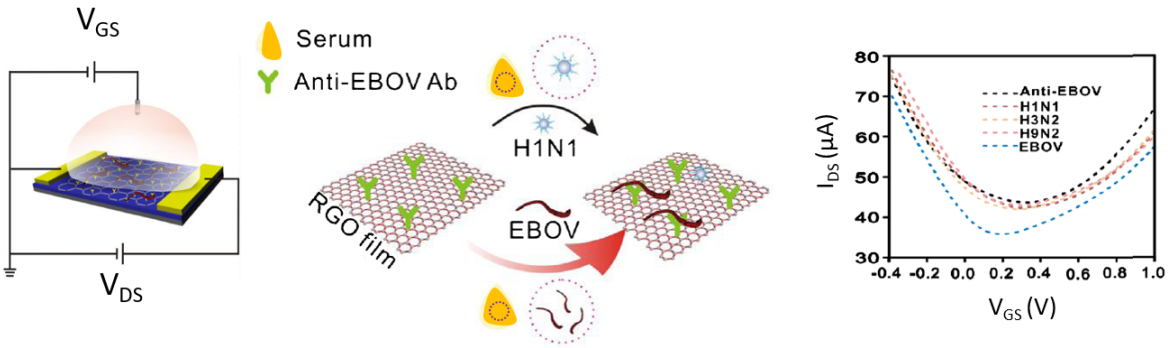

Figure 1.29: Scheme of the rGO EG-FET used for ebola virus detection (left), functionalization step (middle) and obtained transfer curves (right).[118]

The biosensor's specificity was probed by the immobilization of other viruses (H1N1, H3N2, H9N2), causing similar symptoms as EBOV. An important shift of the Dirac point was observed only in the case of EBOV, showing excellent specificity and high binding affinity between the EBOV and corresponding antibody, which can be used in clinical diagnosis.

pH sensing. Lee at al. used an electrolyte gated-reduced graphene oxide transistor (rGO EG-FET) for pH sensing applications.[119] The GO dispersion was spin-coated and reduced in hydrazine monohydrate vapor for 12 h at 60°C, in order to obtain a conductive channel. Different pH buffer solutions were prepared by mixing a 0.1 M HCl and 0.1 M phosphate buffer (NaH_2PO_4 and Na_2HPO_4). As shown in Figure 1.30 (left), the Dirac point position was observed to be pH-dependent.

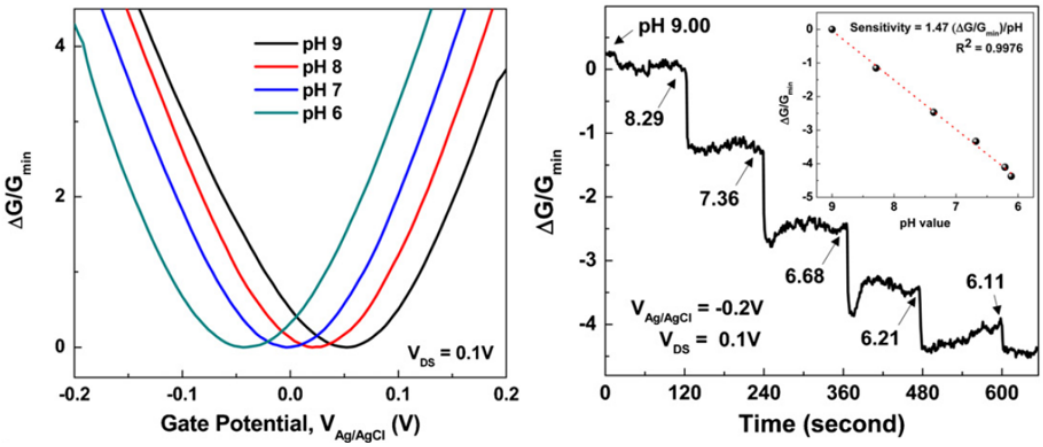

Figure 1.30: Left: Transfer characteristics obtained at different pH values represent the changes of channel conductance ($\frac{\Delta G}{G_{\min}}$) upon variation of gate voltage. Right: Real-time measurement upon the additions of different pH solutions. Inset: Linear response of current to the pH changes.[119]

For lower pH values the Dirac point was found at more negative gate potentials, while for higher pH values the Dirac point was shifted toward more positive gate potentials. The rGO surface was shown to be legitimate for pH sensing, since the

residual functional groups like OH, COOH can interact with the H^+. For lower pH values, more H^+ binding with O^- and COO^- resulted in electron accumulation in the rGO channel. The real-time monitoring of pH was performed under a fixed gate voltage of $V_{GS} = -0.2$ V and a drain bias of $V_{DS} = +0.1$ V (Figure 1.30, right). Every injection of lower pH solution resulted in a current decrease (achieved sensitivity: 1.47 $\frac{\Delta G}{G_{min}}$ per pH unit, where G_{min} represents channel's minimum conductance in the transfer curve). One should note that compared to pristine graphene, rGO used as a channel in GFET leads to lower charge mobilities. In this work, an average charge mobility of $\mu = 0.5$ cm^2 V^{-1} s^{-1} was obtained. Lower charge mobilities were not shown to influence the sensing properties and the ambipolar behavior was preserved. The advantage of using rGO for pH sensing was clearly shown here since pristine graphene does not have binding sites for H^+ bonding, which is the reason why it cannot be used for pH sensing.[120]

DNA sensor. Kim et al. fabricated GFET devices on glass substrates with coplanar array structures and microfluidic channels (Figure 1.31 a.) to detect the cancer-related gene TP53 DNA (target DNA).[121] The conductive channel made of CVD graphene was functionalized with DNA aromatic nucleobases, able to physisorb on graphene. Upon immobilization of probe DNA, the Dirac point position was found to shift toward more negative gate potentials (Figure 1.31 b.) due to the presence of negatively charged phosphate backbone in the DNA molecule. The negative shift induced here cannot be explained by pure capacitive effects (because the positive shift will be expected in this case), but by the electron transfer between DNA molecules and graphene.[122]

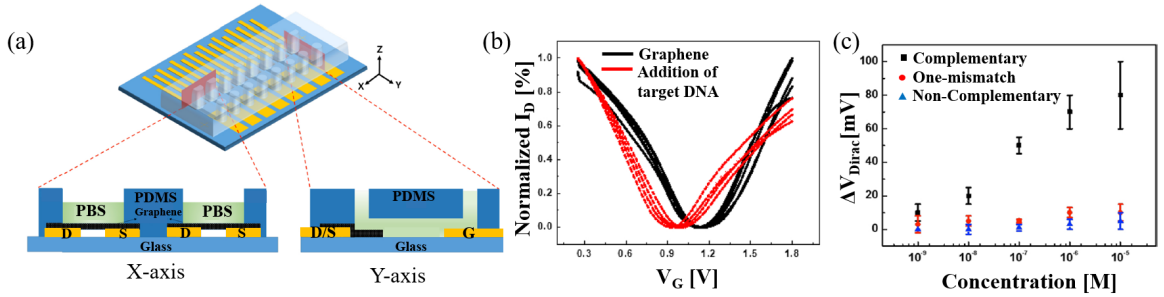

Figure 1.31: a) Schematic presentation of microchannel used and the cross-section view in the X and Y axis. b) Transfer curves obtained before and after the immobilization of DNA. c) Average Dirac point shift data obtained from three different devices for complementary, one mismatch and non-complementary DNA.[121]

The target DNA was immobilized in different concentrations (1 nM−10 μM). With each injection of target DNA, the shift in the Dirac point was observed (Figure 1.31 c.). To validate the selectivity, a control experiment was performed with one mismatched and non-complementary DNA. No significant shift in the Dirac point was observed. The detection limit of 1 nM was achieved.

Real-time tracking of perspiration process. Samori and co-workers reported using rGO conductive channel in flexible liquid-gated transistor configuration, operating in

artificial sweat.[5] The devices were fabricated on polyethylene terephthalate substrates (PET), and the electrodes were patterned using laser ablation. For the application in wearable electronics, the authors proposed two different device layouts. In the first layout (Figure 1.32 a.), the sweat goes from the reservoir to the collector (absorbent textile).

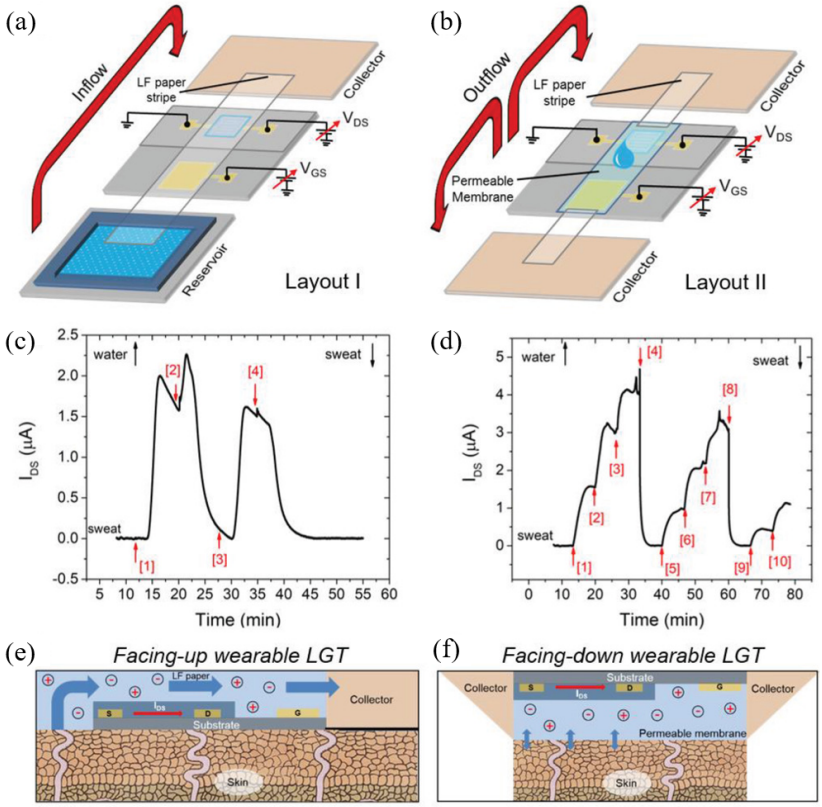

Figure 1.32: Schematic representation of lateral-flow strategy for fluid transportation in the liquid-gated transistor configuration: a) Layout I and b) Layout II, with the respective real-time measurements c), and d), and potential applications e), and f).[5]

The device is placed in the middle and bridged to the opposite sides with the lateral flow paper. This configuration is similar to a microfluidic cell where the reservoir acts as the inlet, while the collector acts as the outlet. In the second layout (Figure 1.32 b.), the sweat is drained out from the top of the device. The confinement of liquid is achieved by the use of a sweat-permeable membrane instead of a frequently used PDMS reservoir. Two collectors are connected by lateral flow paper. Real-time measurements (Figure 1.32 c. and d.) showed both of the layouts eligible for potential sweat tracking applications on the human skin (Figure 1.32 e. and f.) with a faster electrical response in the second layout configuration due to the direct contact between the device and the transducer.

This recent work is an example of how EG-GFET configuration can be practically adapted for applications even in wearable electronics, which is very promising for the future of graphene electronics.

1.6 Conclusions

As seen in this chapter, graphene production can be achieved through different methods and techniques. However, each of these methods has its pros and cons, which have to be taken into account. Since the inkjet printing technique was used for graphene deposition in this work, we opted for solution-processable graphene-based material: graphene oxide.

Among different ways to obtain the conductive, reduced graphene oxide, the electrochemical reduction seemed to be the one with the best control of the overall reduction process and easily applicable to an *in-situ* configuration. In addition, the electrochemical reduction can be performed in a time-effective manner and is considered as a "green" method since there is no use of harsh chemicals. Thus, the presence of potential contaminations can be excluded. Therefore, for the reduction of graphene oxide, we employed here the electrochemical reduction method.

Graphene's remarkable physical properties were shown to be the consequence of its particular electronic properties which can be easily modulated and measured in different field-effect transistor configurations. The EG-GFET configuration was shown as the most sensitive configuration and was presented as very convenient for sensing applications, notably for biosensing, due to the use of low working voltages in aqueous media. This goes hand in hand with sensitive biological samples and our goal to use EG-GFET for bio-sensing applications.

Moreover, graphene's chemical structure was shown to be eligible for different functionalizations methods (covalent or non-covalent) allowing a control over its electronic properties, which is also one of the aspects investigated in this thesis.

Chapter 2

Materials and methods

Chapter 2

Materials and methods

This chapter will describe the main fabrication and characterization techniques, protocols and configurations used throughout this work. The fabrication of transistor structures, as well as the fabrication of electrodes used in the electrochemical and electrical characterizations, will be presented. The elaboration of the transistor's channel will be described along with the GO ink formulation, inkjet printing technique working principle and the *in-situ* GO reduction. Finally, the experimental protocols used for monitoring the photosynthetic activities of cyanobacteria will be discussed.

2.1 Electrode preparations

2.1.1 Fabrication of transistors electrodes

The transistors electrodes were entirely fabricated in the clean room using a standard photolithography process. Silicon substrates (n-doped with phosphorus) of 280 µm thickness with 200 nm thermal oxide (SiO_2) were purchased at BT electronics (wafer diameter: 2"; total electrical resistivity: $3 - 9$ Ohm cm^{-1}). Before any further use, substrates were thoroughly cleaned by bath-sonication in acetone and isopropanol (5 minutes each) and dried under argon flow. To avoid any possible organic contamination, substrates were treated in the plasma cleaner (Diener electronics Pico; gases available: O_2 and Ar) using the oxygen plasma for 3 minutes (working pressure between 0.6 and 0.8 mbar; generator frequency: 40 kHz; power: 160 W). For proper dehydration, substrates were baked at 120 °C for 10 minutes. Reversal photo-resist (AZ 5214 E) was then spin-coated (spinner: Delta 10 Süss Microtec; 500 rpm for 3 seconds and 4000 rpm for 30 seconds) and baked at 110 °C for 60 seconds just before the UV irradiation. A chromium/quartz mask (Toppan photomasks) with 18 defined transistor structures (Figure 2.1, left) was used for the UV photolithography.

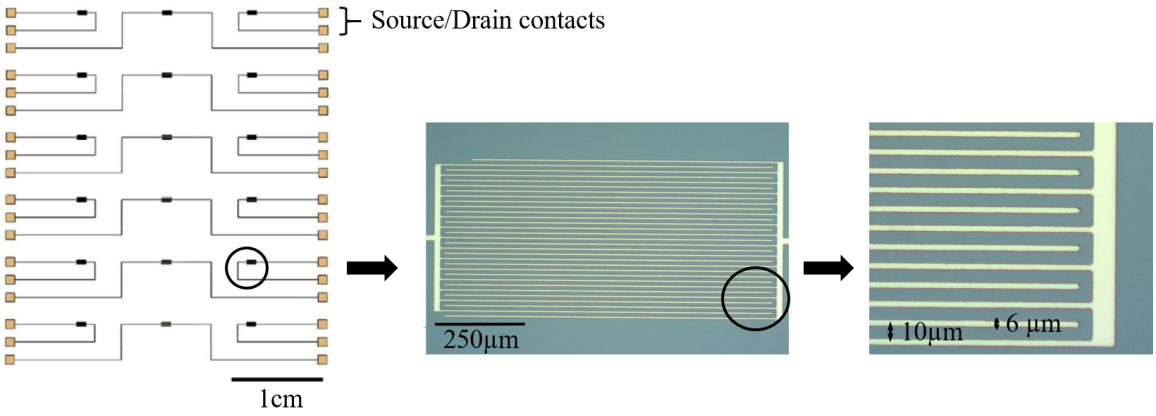

Figure 2.1: Detail of chrome photomask (left) with the zoom on the interdigitated structure.

Photoresist exposure to light was performed using the vacuum contact technique where the mask comes in very close contact with the surface of the silicon substrate. In the case of an inhomogeneity of the spin-coated photoresist, its residuals may appear on the mask's surface. After the mask/substrate alignment (Mask aligner MJB4 simple face, Süss Microtec), substrates were UV exposed for 1.8 seconds (P= 12 mW cm^{-2}, $\lambda = 365$ nm). Reversal bake at 120 °C was applied for 2 minutes and flood exposure for 60 seconds. Development was done in 726 MIF (Metal Ion Free) for 15 seconds. Substrates were then cleaned in distilled water for 1 minute.

Deposition of metallic contacts was performed using an electron beam evaporator (Plassys MEB 550s) with a 10 keV electron gun under high vacuum conditions ($\approx 5 \times 10^{-7}$ mbar). A thin layer of titanium (Ti) was first deposited as an adhesive layer for the gold (Au) deposition (Ti: 10 nm, deposition speed: 0.1 nm s^{-1}; Au: 100 nm, deposition speed: 0.2 nm s^{-1}).

The lift-off process was performed in an ultrasonic bath at 40 °C in acetone and isopropanol (5 minutes each). The final look of the interdigitated structures is presented in Figure 2.1. This structure defines a rectangular area of 1 mm by 0.5 mm which is the total channel area. The distance between two adjacent drain/source digits (defining the transistor channel length L) is 10 µm and the total channel width (W) is 30.000 µm.

2.1.2 Ag/AgCl pseudo-reference electrode

Silver wires of 250 µm diameter (Sigma Aldrich) were used for the preparation of Ag/AgCl reference electrodes. The wires were polished with abrasive paper and rinsed with acetone before use. The experiment was performed in a conventional 3-electrode electrochemical cell, using an inox wire as counter electrode and a saturated calomel electrode (SCE) as reference electrode. Oxidation of silver wires was performed in 0.1 M HCl by running a current of 1 mA (Autolab potentiostat, PGSTAT 302N) for

1 minute through 1 cm of wire. Immediately after, a black thin film deposition of $Ag/AgCl/Ag_2O$ was observed.

2.1.3 Fabrication of microelectrodes

The gate electrodes used for the electrical characterizations of photosynthetic organisms (cyanobacteria *Anabaena flos-aquae*) were "home-made" glass-sealed microelectrodes. The wires of Pt ($\varnothing = 100$ µm) and Au ($\varnothing = 250$ µm) were purchased from Good fellow (France). The equipment used for the fabrication of microelectrodes was a Laser-Based Micropipette puller (P-2000, Sutter instruments). Micropipettes made of borosilicate glass having a 1 mm diameter and 10 cm length were used. The microelectrodes were polished, as a final fabrication step, until the metallic wire was well observed under the optical microscope. Carbon powder was inserted in the micropipette along with the iron wire to facilitate further electrical contact.

2.2 Ink formulation and inkjet printing

2.2.1 Preparation of GO suspension

Commercially available single-layer graphene oxide powder (ACS Materials, modified Hummer's method[54]) was used for preparation of GO suspension.

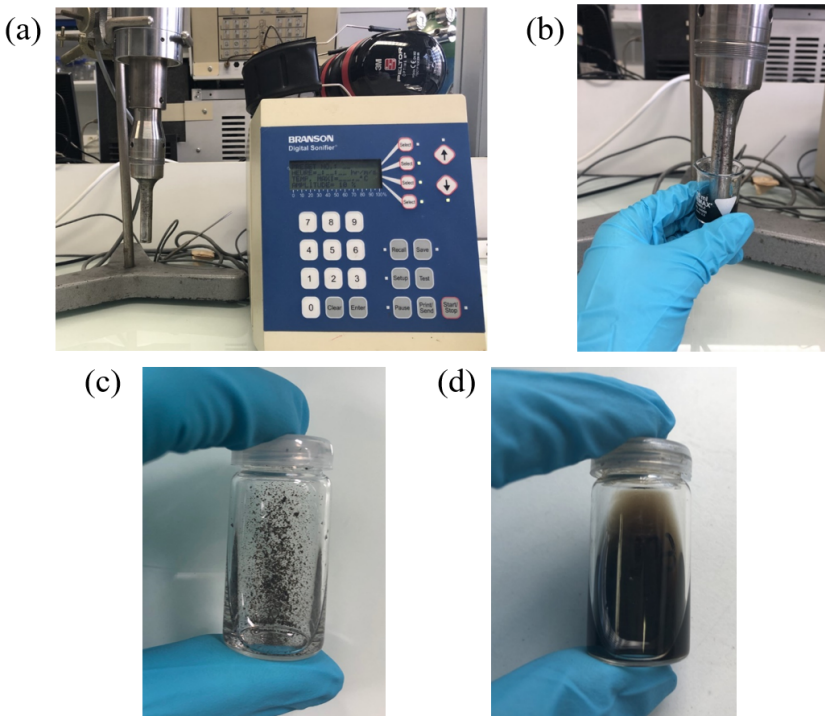

Figure 2.2: a) Branson Digital sonifier with sonication tip; b) Sonication tip position during the sonication process; Aqueous suspension of GO flakes c) before and d) after sonication.

Starting concentration for all suspensions was 1 mg mL^{-1} in distilled water (1 mL of solution was prepared each time). Suspensions were prepared using the BRANSON Digital Sonifier 450 (Figure 2.2 a.) composed of a sonication tip and its user interface. The sonication tip was immersed directly into the GO suspension (Figure 2.2, b.). The applied parameters were 30 seconds sonication using a power of 200 W (50% of the machine's maximum power). The look of GO suspension before and after sonication is shown in Figure 2.2 c. and d., respectively. The final dark brown solution was well dispersed and remained stable for months.

2.2.2 Ink formulation

Starting from an aqueous GO suspension, a printable GO ink was developed. For the optimum performance of the printing process, an ink formulation has to satisfy some fluid requirements such as surface tension and liquid viscosity. To ensure the emission of single, spherical droplets with no satellite drops, the values of these parameters are provided by the printer supplier (Fujifilm).

The ink's surface tension should be in the range of 28 to 42 mN m^{-1} at jetting temperature. If the surface tension is too low, the ink will spontaneously drip from the nozzles. On the other hand, if the surface tension is too high, the separation of drops from the nozzles' surface will not be possible.

Concerning the dynamic viscosity, the ink should be within the range of 10 to 12 cP at jetting temperature. Proper setting of dynamic viscosity helps avoid the formation of satellite drops and "splashing" phenomena when the drops hit the substrate's surface.

Besides, the final ink is expected to have low volatility (boiling points higher than 100 °C are preferred).

The final ink formulation contained a mixture of GO stock solution, ethylene glycol and 1-propanol (50% v/v, 20% v/v and 30% v/v, respectively). The ethylene glycol and 1-propanol were added as a part of the formulation process to improve the compatibility of GO ink with the ideal ranges of the rheological parameters listed above. Surface tension and viscosity of each solvent used are given in Table 2.1.

	Surface tension (mN m^{-1})	Dynamic viscosity (cP)
distilled water	72.80	0.89
ethylene glycol	48.40	16.10
1-propanol	20.90	1.95

Table 2.1: Surface tension and viscosity values of pure solvents used in GO ink formulation.

2.2.3 Rheological characterizations of ink

Surface tension measurements

Surface tension is the fluid's ability to minimize the occupied surface caused by the surface forces acting on the fluid's molecules. For the surface tension measurements, a portable Aqua Pi tensiometer was used with a remote controller (purchased from Kibron). The measuring range of this tensiometer was $10 - 100$ mN m^{-1} with a measuring accuracy of 0.1 mN m^{-1}. A measuring probe (needle) is placed exactly above the liquid's surface. The volume used was approximately 2 mL. When the measurement was launched, the probe was inserted in the liquid and subsequently pulled out (Figure 2.3).

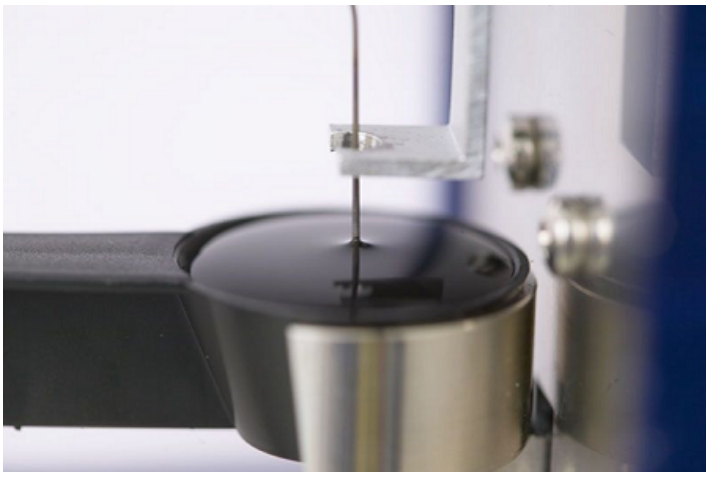

Figure 2.3: Representation of the probe position during the surface tension measurements.[123]

When pulled out of the liquid, the needle's oscillation frequency is translated into the liquid's surface tension value. The surface tension value of the GO ink described above was (28.30 ± 0.06) mN m^{-1} measured at the ambient conditions (c.a. 22 °C).

Viscosity measurements

Dynamic viscosity is the measure of fluid's resistance to flow. The more viscous the fluid is, the thicker it is. On the contrary, a fluid with less important values of viscosity will be more liquid. The equipment used for the viscosity measurements is a Viscometer DV-II+ purchased from Brookfield. After appropriate calibration, the viscosity measurement was performed with approximately 1 mL of the liquid of interest. The rotation speed applied for the measurement was 80 rpm.

Measured dynamic viscosity of GO ink was (3.650 ± 0.006) cP at ambient temperature (c.a. 22 °C). The GO ink showed non-Newtonian behavior and the viscosity value reported here is the plateau value of the viscosity *vs.* speed curve.

2.2.4 Inkjet printing technique

The inkjet printing technique was used for the elaboration of GO transistor channels. The inkjet printer used here was a *Dimatix materials printer 2850* (DMP 2850) from Fujifilm, schematically represented in Figure 2.4.

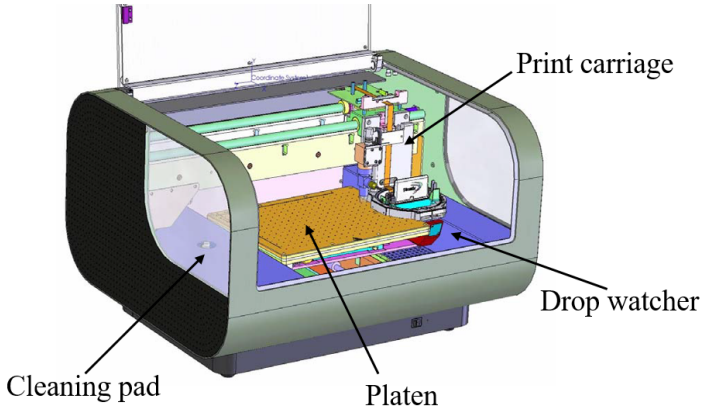

Figure 2.4: Inkjet printer-Dimatix materials printer 2850.[124]

More details about this printer can be found in the DMP user manual ("FUJIFILM Dimatix Materials printer DMP-2800 Series User Manual") and the printer's principal components are presented in Appendix B.

The printer used in this thesis is based on a piezoelectric *Drop on Demand* approach, where a piezoelectric crystal is the center of the event as the transducer of user's demands. Piezoelectric materials are known for their ability to deform in the presence of an electric field. The jetting waveform describes the evolution of the voltage applied to each nozzle with time. When the applied voltage increases, the reservoir walls deform, thus creating a pressure wave inside the reservoir itself. This pressure increase is responsible for the ejection of drops. Figure 2.5 a. represents a deflected piezoelectric crystal and the corresponding waveform. The dashed blue line in the waveform represents a region where the applied voltage increases with time.

The jetting speed can be modified by adjusting the applied voltage. For good printing resolution, setting a proper jetting speed is crucial. If the drop velocities are too high, the undesired effects such as splashing may occur, resulting in the formation of satellite drops which can decrease printing process resolution. For GO ink, the applied voltage was 15 V leading to a jetting speed of 7 m s^{-1}. Drop formation at the printing nozzles is shown in Figure 2.5 b. As observed, all printing nozzles worked properly thanks to the proper GO ink formulation. The printing was fluid without hardly clogged nozzles.

For homogeneous printing features, it is important that the printed drops are neither too far from each other nor too close. If the printed drops are too distant, printed layers could look like interrupted lines. On the contrary, complete overlapping of printed drops

will result in the agglomeration of printed features. Before any printing process, it is crucial to have an insight into the printed drop diameter. Figure 2.5 c., shows the GO ink printed drops on the clean Si wafer's surface.

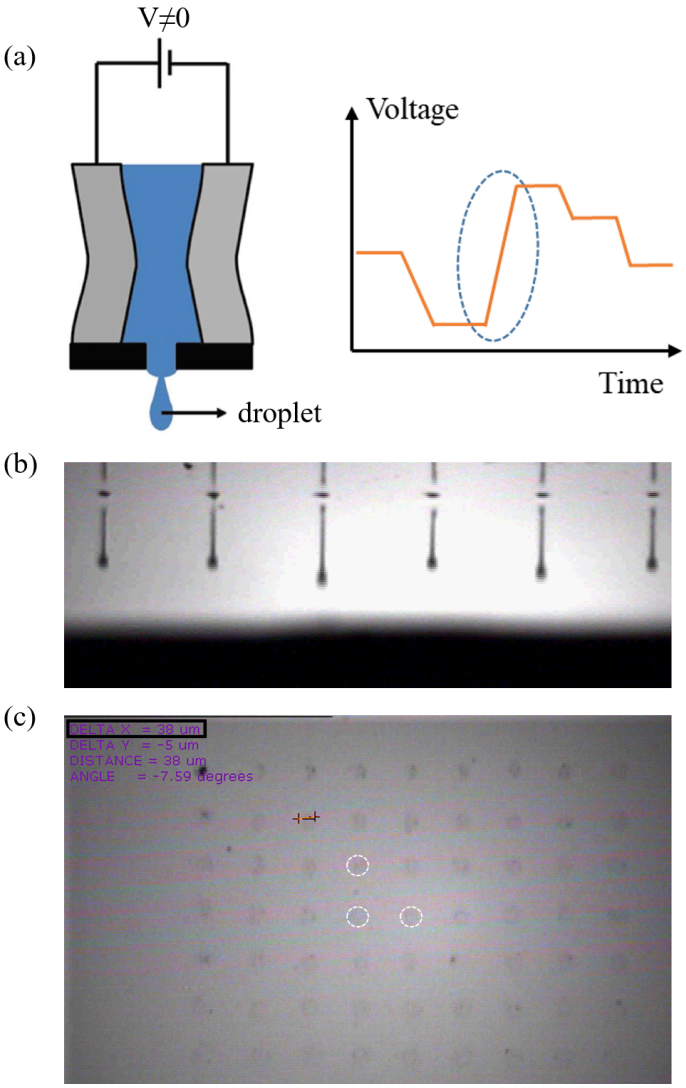

Figure 2.5: a) Schematic representation of deflected piezoelectric crystal and drop formation[125] with its corresponding waveform. b) A screen-shot from a video showing the ejection of GO ink from the printing nozzles. c) GO printed drops on silicon wafer. For the sake of clarity, white dashed circles are highlighting the drops presence.

Due to the almost optically transparent GO ink and very low volumes of printed drops (10 pL), the drops are barely visible. The drops had a diameter (D) ranging approximately from 30 to 40 µm. Now, an important parameter called drop spacing (d) can be defined. Drop spacing is the distance between two adjacent printed drops, which is a parameter that the user can fix. The following formula:

$$d = \frac{D}{2} \tag{2.1}$$

defines an empirical method used to set the best possible drop spacing after the measurement of average drops' diameter. Nevertheless, deviations from this empirical formula frequently occur. For the GO inkjet printing, the average drop spacing used was 15 µm. To improve the final homogeneity, three subsequent layers were printed one on the top of the other.

2.3 Electrochemical reduction of GO

The GO printed film was electro-reduced using an *in-situ* approach developed in this thesis. Figure 2.6 represents the scheme of the 3-electrode setup used here.

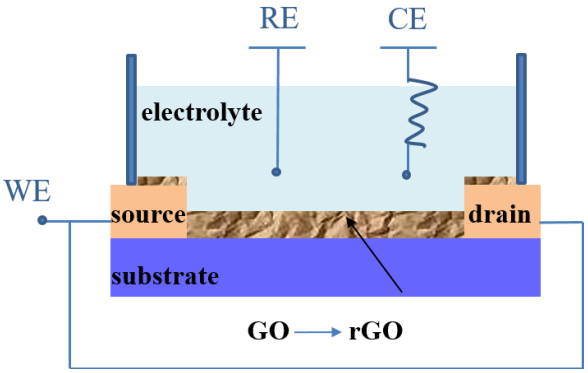

Figure 2.6: Setup for the *in-situ* electrochemical reduction of GO printed film.

For both the electrochemical reduction of GO and the impedance measurements, the potentiostat used was a Biologic SP-200. The reduction was performed directly on the transistor's bottom-contact structure, previously described. The source and drain interdigitated gold contacts were short-circuited, serving as a working electrode. The *home-made* Ag/AgCl electrode was used as reference electrode and an inox wire as counter electrode. The electrolyte used for all electrochemistry experiments was phosphate-buffered saline (PBS) purchased in the form of tablets (Sigma Aldrich) and prepared in distilled water (pH=7.4; concentrations: 137 mM NaCl, 8 mM Na_2HPO_4, 2 mM KH_2PO_4 and 2.7 mM KCl).

The electrolyte was contained by lab-made polydimethylsiloxane (PDMS) wells. The $3D$ printed support was used to ensure good adhesion of the PDMS wells onto the substrate as schematically represented in Figure 2.7. These wells ensured the electrolyte's volume to be kept constant for each experiment (150 µL).

The reduction was performed using chronoamperometry. The constant potential of −1.3 V was applied for reduction times ranging from 1 to 100 seconds.

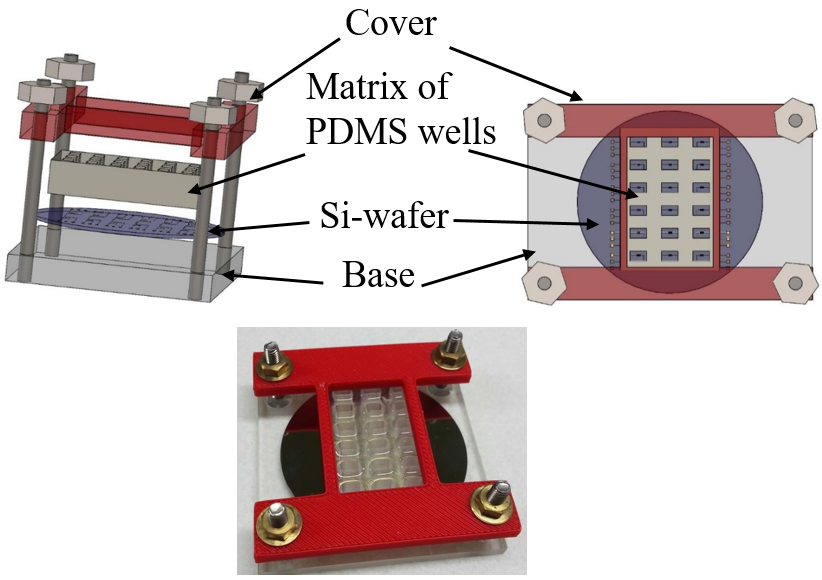

Figure 2.7: PDMS wells with the 3*D* printed support.

2.4 Characterization techniques

The characterization techniques used in this work are mainly based on surface topography investigations and electrical characterizations. The morphological surface characterizations were performed by atomic force microscopy (AFM) on both drop-casted and inkjet-printed GO inks, as well as on the GO flakes after molecular functionalization. Following the reduction of GO layers, the electrical characterizations were performed. These techniques and used configurations will be described in the following sections.

2.4.1 Morphological characterizations

(AFM) is one of the most widely used scanning probe microscopy (SPM) techniques for the surface characterizations at the nanometric scale. The main components of an AFM are a local probe mounted on a flexible cantilever, a piezoelectric scanner which moves the tip relatively to the sample surface in the three space directions, a laser beam reflected by the rear side of the cantilever and a four-quadrant photo-detector which detects and amplifies the probe's vertical movements (Figure 2.8, left). The cantilever is usually made of silicon or silicon nitride and possesses a spring constant of $10 - 100$ N m^{-1} for tapping (used here) and non-contact mode, which enables the piezoelectric actuator to scan the surface with the atomically sharp probe ($20 - 60$ nm radius of curvature).[126] For contact mode, the spring constant is below 1 N m^{-1}. The working principle of an AFM is based on the detection of forces (van der Waals force mainly but also: capillary, frictional, chemical, electrostatic, and magnetic forces) between the probe and the sample's surface within an atomic distance (Figure 2.8, right).[127] The

force exerted on the probe will vary with the surface topography differences leading to the cantilever deflection.

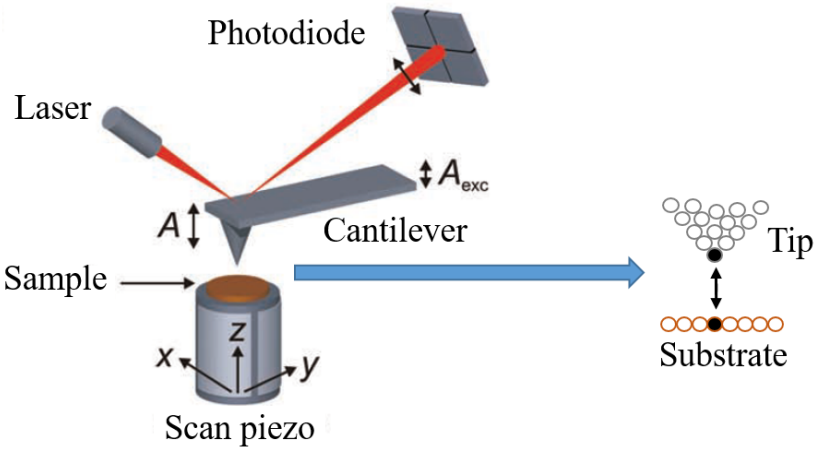

Figure 2.8: Schematic representation of an AFM setup. Adapted from[127].

Cantilever's constant bending is maintained by adjusting the piezoelectric actuator's vertical position through a feedback loop on the position of the laser beam reflected by the local probe onto the photo-detector. Every deflection of the cantilever following the surface topography is recorded within a vertical accuracy of typically 1 Å. The overall force (F) between the sample and the tip can be calculated using Hooke's law from the cantilever deflection (Δ z) and its spring constant (k):

$$F = -k\Delta z \tag{2.2}$$

AFM can be operated according to three different modes:

- *Contact mode*: a sample and a probe are in contact and a gap in between them is less than a few angstroms (Å). The prevalent force exerted on the scanning tip is the van der Waals attractive force.
- *Non-contact mode* comprises a more important distance between the tip and the sample, which is about several tens to several hundreds of Å. The attractive van der Waals force is exerted on the tip.
- *Tapping* or intermittent mode is in between contact and non-contact mode. Term *tapping* is used because there is a very light contact between the tip and the sample.

The device used in this work was an AFM NT-MDT Solver P47 along with the standard silicon probes (Nanosensors, model PPP-NCHR). Tapping mode is used for the morphological characterizations of samples. Free software WSxM was used for data analysis.[128]

2.4.2 Electrical characterizations

Electrical characterizations of field-effect devices were performed using a semiconductor characterization system Keithley 4200 along with a probe station: Süss MicroTec PM5. The electrolyte-gated field-effect transistor configuration used here is shown in Figure 2.9. A gold wire ($\varnothing = 1$ mm) was used as a gate electrode.

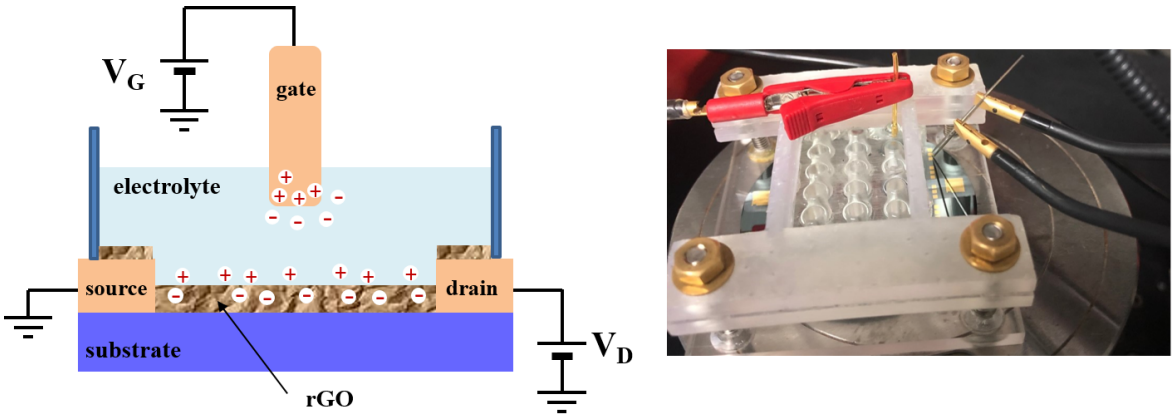

Figure 2.9: Left: Schematic representation of the electrolyte-gated field-effect transistor configuration with rGO as the active layer. Right: EG-GFET configuration with the gate electrode above the PDMS wells and micro-manipulators on the source/drain contacts.

The transistor's transfer characteristics were acquired by sweeping the gate voltage from 1.9 V to 0.9 V, depending on the experiment (voltage step: 0.02 V, sweep delay: 0.5 s, hold delay: 3 s). The drain voltage for the transfer characteristics was kept constant at 0.9 V. For the output characteristics, drain voltage was swept from −0.1 V to 0.9 V keeping the gate voltage at a fixed value in the range of 1.3 to 1.9 V (with a step of 0.1 V).

2.5 Experimental section: rGO EG-FET as a biosensor

2.5.1 Cellular medium preparation

The cyanobacteria *Anabaena flos-aquae* used for biosensing purposes were provided by the National Museum of Natural History in Paris. The photosynthetic organisms were kept and grown in aqueous Bold's basal medium (B_{3N}) at pH= 7.4. For each liter of B_{3N} solution, 1 mL of vitamin solution (0.11 nM vitamin B_12, 1.02 nM vitamin H, 2.97 µM vitamin B_1) is added. Preparation of B_{3N} was performed using ultra pure distilled water (MilliQ) and contained: 2.16 µM $VOSO_4 \cdot 2\,H_2O$, 17 mM $CaCl_2 \cdot 2\,H_2O$, 0.34 mM NaCl, 0.641 µM $CuSO_4 \cdot 5\,H_2O$, 0.43 mM K_2HPO_4, 0.819 µM $(NH_4)Mo_7O_{24} \cdot 4\,H_2O$,

0.125 mM $MnCl_2 \cdot 4H_2O$, 0.034 mM EDTA, 7.65 µM $ZnSO_4 \cdot 7H_{20}$, 8.8 mM $NaNO_3$, 1.29 mM KH_2PO_4, 3.2 µM $CoSO_4 \cdot 7H_{20}$, 0.39 mM H_3BO_3, 3 mM $MgSO_4 \cdot 7H_2O$. Before use, B_{3N} was sterilized in an autoclave at 120 °C.

2.5.2 Gate functionalization

The platinum microelectrode used as gate in the rGO EG-FET configuration was functionalized in a conventional 3-electrode electrochemical setup using an inox mesh as counter electrode and a commercial Ag/AgCl as reference electrode. The electrolyte (0.1 M tetrabutylammonium hexafluorophosphate, $TBAPF_6$ purchased at Sigma Aldrich) was dissolved in pure ethylenediamine (Sigma Aldrich). Cyclic voltammetry was performed in the range of $0 - 1.4$ V (scan rate 50 mV s^{-1}).

2.5.3 Preparation of hydrogel containing cyanobacteria

The alginate hydrogel was prepared by making a 2 % (w/v) sodium alginate solution in MilliQ water. The cyanobacteria solution was sampled each time in 2 mL eppendorfs and subsequently centrifuged at 1500 rpm for 90 seconds. The obtained float was mixed in a 50/50 ratio with the alginate hydrogel. For the gate functionalization, the gate electrode was dipped in the cyanobacteria/hydrogel mixture and reticulated in 0.1 M $CaCl_2$ for 5 minutes. For the hydrogel used as a solid electrolyte in rGO EG-FET, the mixture of cyanobacteria/hydrogel was sampled (10 µL) and the drops were ejected into 0.1 M $CaCl_2$ for the reticulation.

2.6 Conclusions

Fabrication and characterization methods described in this chapter, toward experimental conditions used in biosensing applications, lead to the development of an EG-GFET device based on reduced graphene oxide further used as a biosensor. The inkjet printing technique, introduced here, was employed for the elaboration of GO transistor channels using an inkjet-printable GO-based ink, formulated in this work. The presented *in-situ* approach for electrochemical reduction allowed us to obtain conductive channels directly on the interdigitated source/drain structures. Additional details about the elaboration of the rGO transistor's channels and the in-depth study of its electrical characteristics in the EG-GFET configuration are discussed in the next chapter.

Chapter 3

Control of GO electronic properties in EG-GFET configuration

Chapter 3

Control of GO electronic properties in EG-GFET configuration

In this chapter, we present the inkjet printing deposition of GO on the transistor's bottom contact photolithographed structure. As graphene oxide (GO) is known as a material that can be deposited from liquid suspensions, we used it here in the ink formulation. The reduction of graphene oxide (rGO) is also discussed. Before any sensing application on rGO, we aimed to explore and control the rGO's charge transport properties using two different approaches: on the one hand, by an electrochemical tuning of the reduction state of rGO, and on the other hand, through molecular functionalization of its basal plane. These studies were performed mainly by electrical tests (current/voltage characteristics). The influence of the electrochemical reduction rate on the electronic behavior of rGO in the EG-GFET configuration is discussed. We also demonstrate that self-assemblies of original nitrogen-rich aromatic molecules adsorbed on rGO can tune its Fermi level.

3.1 Elaboration of printed GO channels

As a printable ink has to satisfy some essential parameters like surface tension and viscosity in a certain range of values (described in Chapter 2), another important parameter to take into account is the size of the GO flakes contained in the ink.

Nozzles diameter being around 21 µm, we aimed to obtain an average size of GO flakes of 1 µm (for proper printing, GO's flakes lateral size should not exceed $\approx$ 10 % of the nozzle diameter). The ultrasonic fragmentation process, here used, is known to reduce the size and adjust the shape of GO flakes.[129] This was an essential step to avoid the flakes agglomeration in the printing nozzles. We undertook a study of sonication power and sonication duration influence on the GO flakes morphology. Figure 3.1 a., shows the results for combining these two parameters: the morphology evolution with

sonication time at fixed power (P=200 W, row of AFM images) *versus* the morphology evolution with sonication power at fixed duration (t=30 s, column of AFM images).

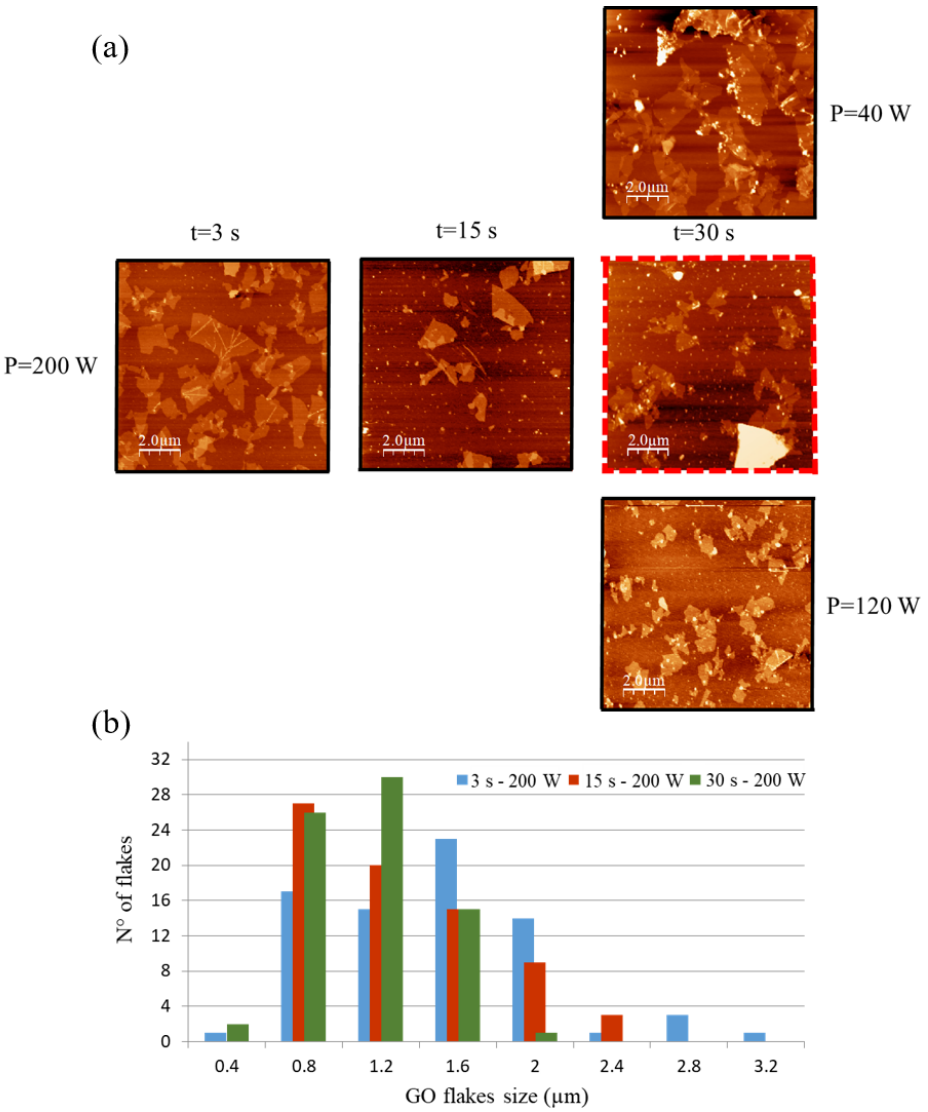

Figure 3.1: a) Typical AFM images of drop-casted aqueous GO solutions (0.1 mg mL^{-1}) obtained for two different series: by fixing sonication power (P=200 W, images in row) or sonication time (t=30s, images in column). Dispersions were drop-casted on the SiO_2/Si substrate; b) Size distribution of GO flakes obtained under constant sonication power (P=200 W) and variable sonication time (t=3 s, 15 s, 30 s).

GO aqueous dispersions were drop-casted onto the SiO_2/Si substrate. AFM characterizations were performed right after drying in air. One can observe that the GO flakes' shape vary for both series. However, it seems that by increasing the sonication power, the GO flakes become more fragmented resulting in an important size reduction. In Figure 3.1 b., the distribution of GO flakes is shown for a fixed sonication power of 200 W and different sonication times. To construct the histogram, on average, 12 AFM images were analyzed (on average, $\approx$ 75 GO flakes were measured per each sonication time). One can observe that the sonication duration of t= 30 s contained $\approx$ 80 % of

flakes with an adequate size for printing ($\approx 0.8 - 1.2$ µm, to prevent nozzle clogging). From this statistical study we concluded that the best sonication parameters are t= 30 s and P= 200 W. These parameters are used in the further elaboration of transistor's channel through the inkjet printing process.

Figure 3.2 shows the AFM topographical characterizations of drop-casted GO aqueous solution on the SiO_2/Si substrate and the inkjet-printed layer on the bottom contact photolithographed transistor's structure with their respective height profiles.

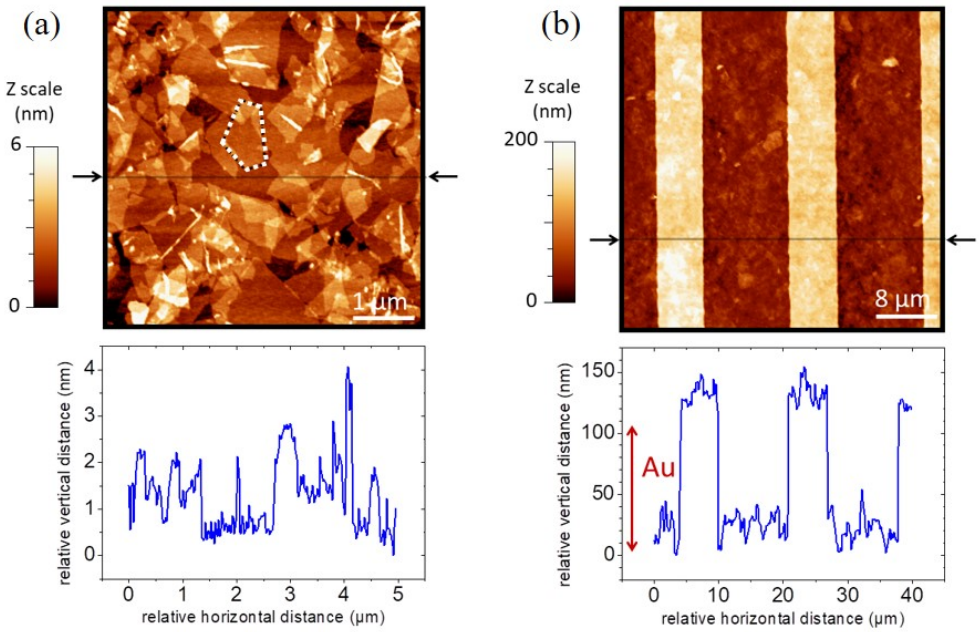

Figure 3.2: AFM characterizations of: a) drop-casted GO aqueous dispersion (0.1 mg mL^{-1}) on SiO_2/Si wafer (for the sake of clarity, one of the GO flakes is bordered with white/black dotted line); b) GO inkjet-printed layer (0.5 mg mL^{-1}) on the interdigitated photolithographed Au contacts. The height profiles' positions are indicated by arrows.

Regarding the drop casted layer (Figure 3.2 a.) one can observe the partial overlapping of GO flakes. The majority of flakes lie parallel to the surface. Moreover, a limited wrinkles density is observed, appearing as the bright straight lines in the AFM image. The average estimated thickness of drop-casted GO flakes was found in the range of $0.5 - 2$ nm. Knowing that the interlayer spacing in graphite is 0.34 nm, the thickness of rGO flakes varies from the single-layer up to ≈ 6 monolayers. Regarding the inkjet-printed GO layer (Figure 3.2 b.), the overlapping GO flakes are observed to cover the Au electrodes and silica substrate between the electrodes. A roughness of 12 nm is found on silica (RMS value). The average estimated thickness of the printed layer is found to be ≈ 30 nm.

Before any further electrical characterizations of the printed layer, GO had to be transformed into its conductive form: reduced GO (rGO). This step will be discussed

in the next section.

3.2 GO reduction

Among the different methods to reduce GO, we focused on the electrochemical reduction. The electrochemical approach allows us to obtain rGO in a 'green' way without the use of any harsh chemicals, thus avoiding potential contaminations. The electrochemical reduction was performed in a conventional 3-electrode electrochemical setup to explore the reduction potential. Furthermore, the electrochemical reduction was adapted to an *in-situ* configuration, allowing us to obtain rGO directly on the transistor's bottom-contact structure. The electrochemical studies of GO on the macroscopic electrodes will be presented in the next part, followed by the results obtained by the *in-situ* reduction approach.

3.2.1 Electrochemical investigations (in the electrochemical cell)

The electrochemical reduction of GO was investigated in a nitrogen-saturated electrolyte PBS (pH=7.4). Aqueous GO dispersion (1 mg mL^{-1}) was drop-casted (20 µL) onto the surface of the macroscopic glassy carbon electrode (GCE). The voltage was swept from 0 to -1.8 V for five cyclic voltammetry (CV) scans (scan rate 50 mV s^{-1}).

Figure 3.3 (left) shows the cyclic voltammograms obtained for bare and GO functionalized GCE, respectively.

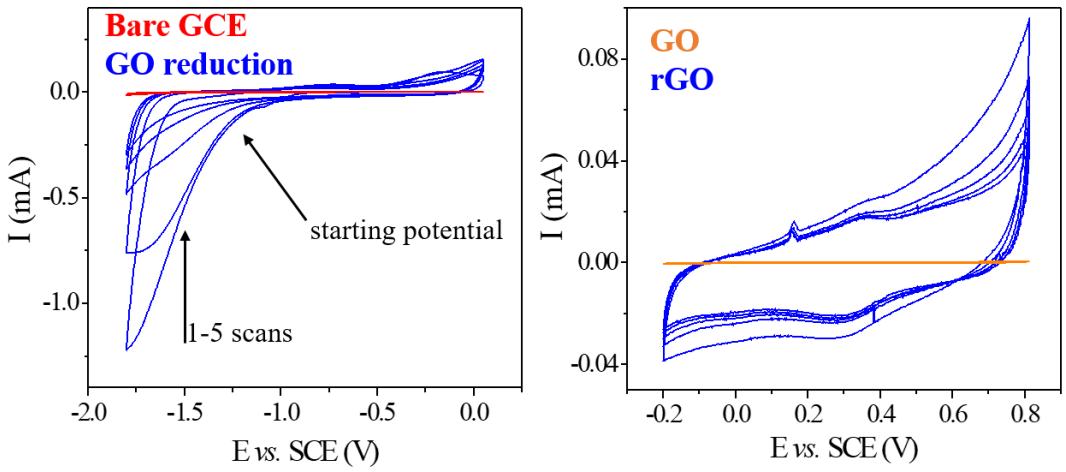

Figure 3.3: Left: Cyclic voltammograms of bare GCE (red) and GO reduction (blue) performed in PBS, scan rate 50 mV s^{-1}. Right: Electrochemical characterization in 1 M H_2SO_4 of GO before (orange) and after (blue) reduction on GCE.

As it can be noticed, with each scan, the current tends to decrease which indicates the progressive GO reduction. The maximum reduction current was found at ≈ -1.7 V with starting reduction potential in the range of -1.2 V to -1.3 V.

The electrochemical characterizations of both GO and rGO films in 1 M H_2SO_4 are shown in Figure 3.3 (right). The low capacitive current observed for GO is related to oxygen groups' presence, which makes GO insulating. In the deoxygenation process, as the material's conductivity increases, the capacitive current increases too.[130] The observed redox peak can be attributed to the transition between quinone/hydroquinone groups, typical for carbon-based materials, indicating the possible presence of residual oxygen in rGO.[131] As we aimed to perform an *in-situ* reduction approach on the gold transistor's contacts, the reduction behavior was investigated as well on the Au macroscopic electrode, with a similar observed behavior (Appendix C.1).

3.2.2 *In-situ* reduction and optical characterizations

Following the GO inkjet printing on the transistor's bottom-contact structure, the GO was electrochemically reduced. An *in-situ* approach for electrochemical reduction developed here is described in detail in Chapter 2. By applying a potential of -1.3 V (*vs.* Ag/AgCl) on the short-circuited gold source and drain contacts, acting as the working electrode, GO was successfully reduced. Moreover, the reduction process duration was controlled.

Figure 3.4 a., shows the same GO printed layer exposed to different reduction durations. As it can be noticed, the GO reduction resulted in a color change, which was a visual indication of successful reduction.[60] In fact, this color change is the consequence of the restored π-conjugated system. Moreover, the increased reduction duration was followed by the progressive darkening of the rGO layer. First, the darkening of the printed layer occurred on the Au interdigitated electrodes (1 s) and then progressed out of the interdigitated pattern (10 s). A similar behavior was observed in the literature.[73]

Besides, one could observe the inhomogeneous contrast in the rGO film. These local color changes are even more pronounced upon prolonged reduction. Nevertheless, one should keep in mind that inkjet deposition inherently brings some thickness fluctuations. Therefore, we assign the local color changes to the thickness fluctuations, rather than to the inhomogeneous reduction process. For the sake of comparison, Figure 3.4 b., depicts the same drop-casted GO layers before and after *in-situ* electrochemical reduction. For both GO and rGO layers, the thickness variations are much less pronounced. Consequently, the rGO layer presents a homogeneous dark contrast, which attests the uniform reduction process.

The effect of the reduction process on the electronic properties of rGO was investigated in the rGO EG-FET configuration.

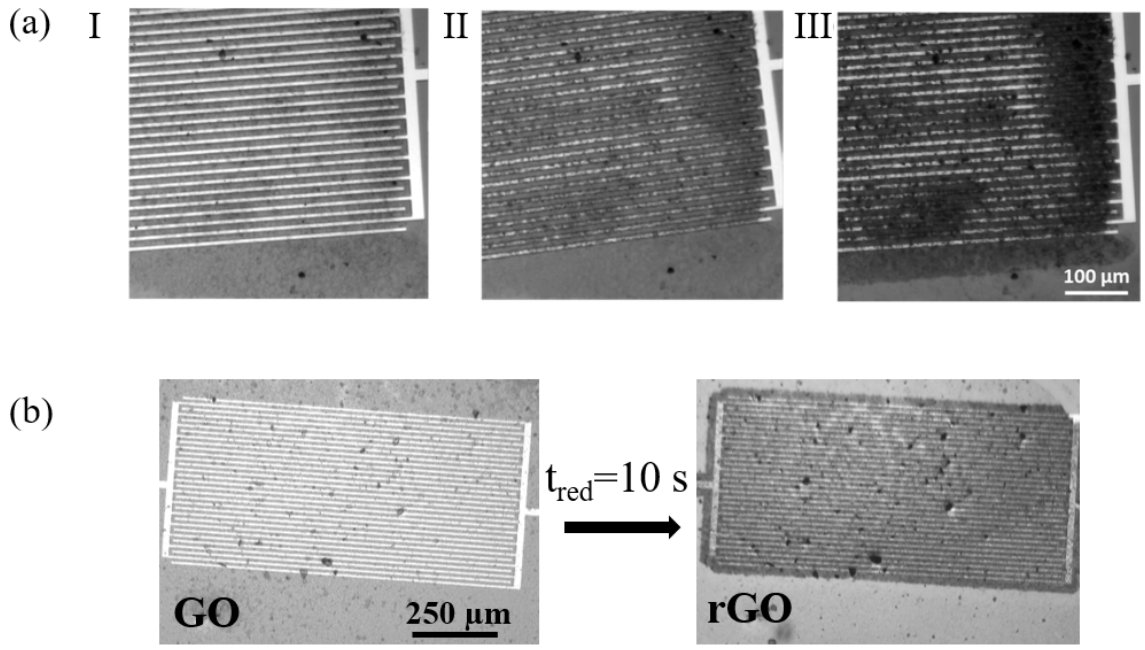

Figure 3.4: a) Optical microscopy image of the same GO inkjet printed layer on the interdigitated transistor's structure I) before reduction and after II) 1 s and III) 10 s of reduction; b) Drop casted GO film on the interdigitated structure before (left) and after (right) 10 s of electrochemical reduction.

To achieve this, the GO was electrically characterized at different reduction stages, which will be discussed in the following section.

3.3 Electrical characterization of rGO

Following electrochemical reduction, rGO printed layers were subjected to characterizations of their electronic properties in the EG-GFET configuration, using PBS as electrolyte (Figure 3.5 a). The electrical characteristics obtained after 1 s of reduction are shown in Figure 3.5 (b, c, d).

The output curves (I_{DS}-V_{DS}, Figure 3.5 b.) show the variation of current with applied drain voltage at fixed gate potential. The shift of the output curves for each gate voltage step evidences the presence of a field effect in our device, and the possibility for its modulation through variation of the applied gate voltage. The drain current is found to vary linearly with the drain voltage, suggesting a linear conduction regime present in rGO.

Transfer curves (I_{DS}-V_{GS}, Figure 3.5 c.) recorded in the back (sweeping V_{GS} from 1.9 to 1 V) and forth (sweeping V_{GS} from 1 to 1.9 V) direction for the same device (same rGO layer, t_{red}=1 s) reveal a typical V-shaped curve obtained for graphene-based materials, with two branches that intersect at the minimum current defined as the Dirac point "position".

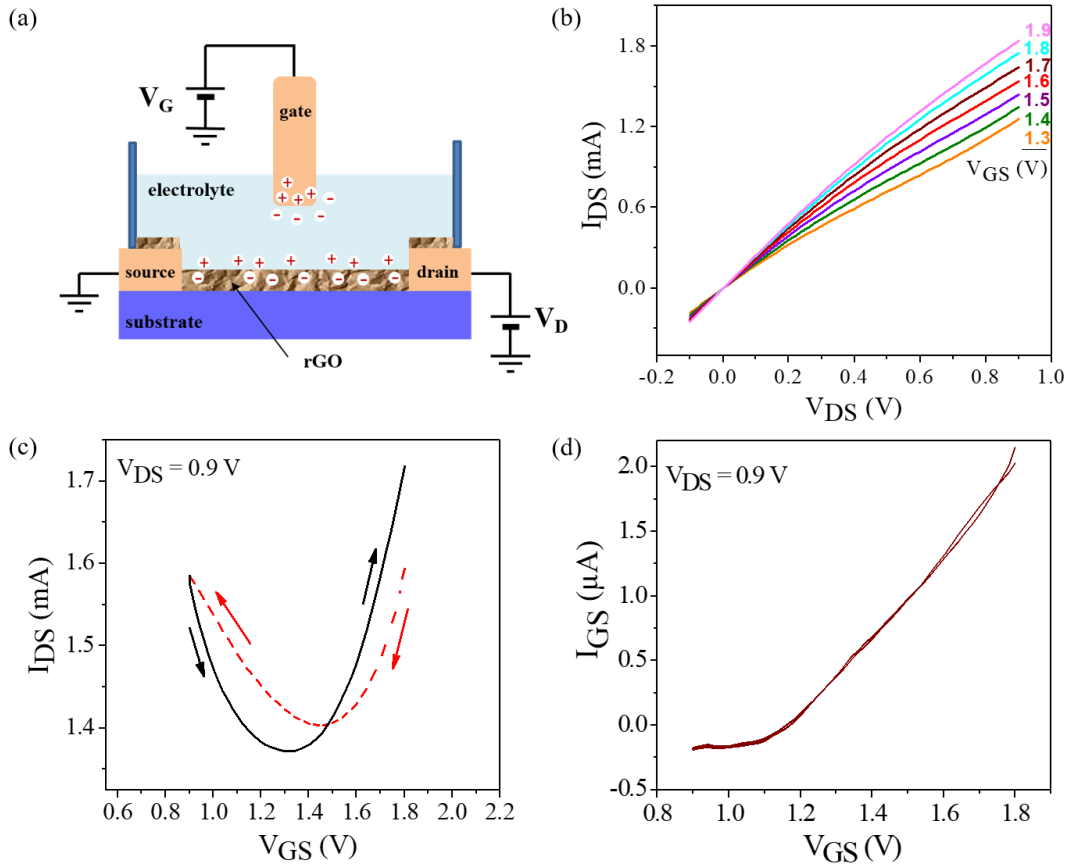

Figure 3.5: a) Schematic representation of the rGO EG-FET configuration; Electrical characteristics of printed rGO layer upon 1 s of electrochemical reduction: b) Output curves recorded by fixing the gate-source voltage (V_{GS}) and sweeping the drain-source voltage (V_{DS}). c) Transfer curves recorded for the fixed drain voltage value (V_{DS}=0.9 V) in the back (V_{GS} from 1.9 to 1 V; red dashed line) and forth (V_{GS} from 1 to 1.9 V; black solid line) direction. Arrows indicate the sweeping directions. d) Gate current variations with V_{GS} corresponding to the transfer curve.

Here, the Dirac point is situated at $V_{GS} \approx 1.3$ V (forth sweep). The stability of the device was verified by consecutive current/voltage acquisitions on the same rGO layer (Appendix C.2.1), evidencing the stability and robustness of charge transport in the rGO layer itself. As discussed in Chapter 1, if the Dirac point position is found at a gate voltage different from 0 V, a possible doping effect could be present. In our case, the minimum current point is found at positive gate voltage suggesting that the rGO is p-doped. Similar behavior was remarked in the literature.[132] It was attributed to the presence of both positively charged impurities, and a charge transfer between graphene and the underlying substrate.

Also, the transfer curve reveals the presence of hysteresis between the back and the forth sweeps, causing a roughly 100 mV shift of the Dirac point position. According to the litterature, two possible mechanisms can explain this behavior: charge trapping from/to graphene or capacitive gating effects, which are believed to coexist and compete

in graphene-based transistors.[133] Possibly, charges stay trapped between the substrate and the graphene layer, and act as a local floating gate that partially screens the effective applied gate potential.

The gate current is another important parameter of EG-GFET electrical characteristics. As the gate electrode is often considered as a 'counter' electrode in the EG-GFET configuration, if some parallel/parasitic reactions (Faradaic process) occur in the system, they can be reflected by important variations of gate current. That is the reason why the gate current should always be taken into consideration. Figure 3.5 d., shows the gate current *versus* gate voltage related to the transfer characteristic of Figure 3.5 c. Here, the gate current (I_{GS}) is found to be 3 orders of magnitude lower than the recorded drain current (I_{DS}), showing that the drain current is not interfered with parallel reactions occurring at the gate electrode.

Previous theoretical and experimental research works showed that the band gap closure, which occurs upon reduction of GO into rGO, can be controlled through the tuning of the 2D material's oxidation state.[134;135;136;84] To our knowledge, there are no studies that addressed the rGO's electrical properties in EG-GFET configuration upon different reduction states. The study of rGO's charge transport behavior as a function of the reduction degree will be presented in the following subsection.

3.3.1 Effect of the reduction time on rGO in EG-FETs

In order to investigate the influence of the reduction degree on the rGO's electrical properties, the reduction potential was kept constant and the duration of the process was carefully controlled.[137]

Figure 3.6 shows the rGO's transfer characteristics obtained for different reduction times, ranging from 1 to 10 s. The progressive increase in reduction time was reflected on the transfer curves both in terms of the Dirac point position and the slopes of both hole and electron branches. The Dirac point position was found to shift toward less positive potentials with increased reduction time, while both branches' slopes were found to decrease. The possible origin of this behavior will be discussed in the section 3.3.2.

Although the slope damping and the Dirac point shift are systematically observed upon increased reduction duration on all tested devices, one should keep in mind that the current and voltage at the Dirac point are not strictly the same from one rGO EG-FET to another. To illustrate this, additional data from another inkjet printed sample are shown in Appendix C.2.2. Bearing in mind that the GO channel is ink-jetted with inherent thickness fluctuations, as previously mentioned, consequently the overlapping of GO flakes is not the same for each sample.

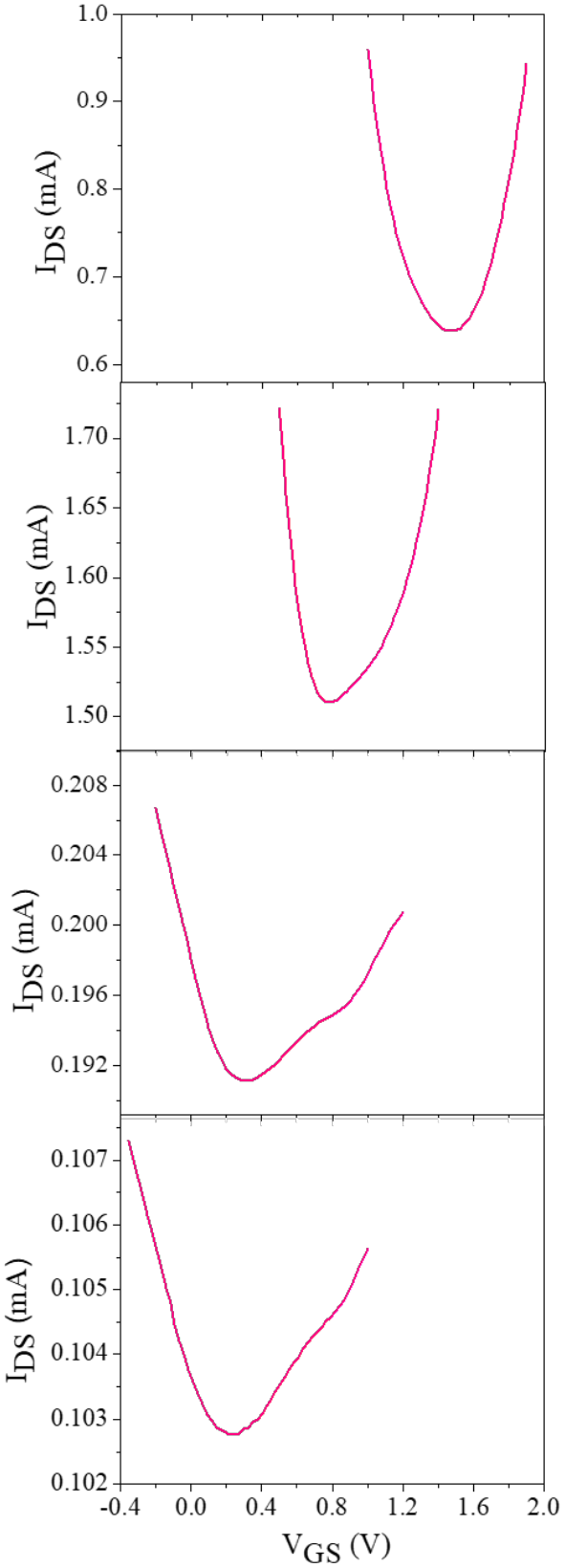

Figure 3.6: Transfer curves recorded upon the progressive increase of the electrochemical reduction duration (from up to down: $t_{red} = 1$ s, 3 s, 6 s, 10 s) over the same rGO EG-FET sample ($V_{DS} = 0.9$ V).

This leads to variations of both the overall current and the Dirac point position.

The gate currents related to the transfer characteristics obtained after different reduction times are shown in Figure 3.7.

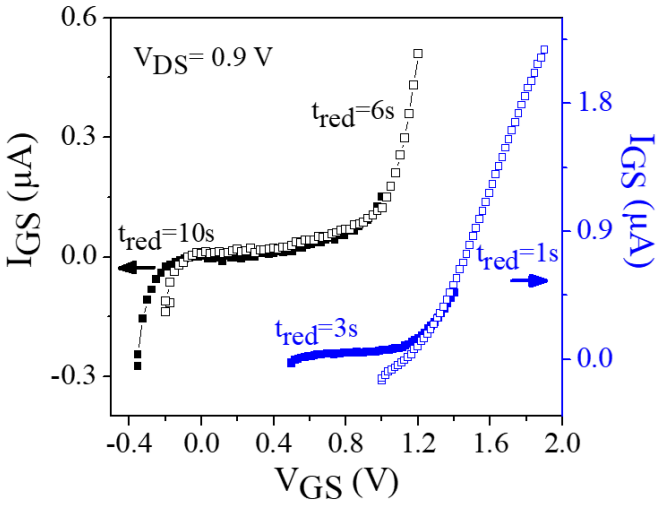

Figure 3.7: Gate currents *versus* gate voltage characteristics obtained for rGO upon different reduction times (related to Figure 3.6). The arrows indicate the reading scale of each characteristics.

The gate current is observed to be in the μA range for each reduction time and do not interfere with the drain current (in the mA range).

From the presented electrical characteristics, the extraction of electronic parameters is performed and is discussed in the following text.

3.3.2 Extraction of electronic transport parameters and discussion

As discussed in Chapter 1 (paragraph: "Extraction of electrical parameters") from the following equation: $g_m = \frac{\partial I_{DS}}{\partial V_{GS}} = \mu \times C_{TOT} \frac{W}{L} V_{DS}$, one can observe that the slope variations are linearly dependent on the product of mobility and the total capacitance (where the total capacitance is expressed as: $\frac{1}{C_{TOT}} = \frac{1}{C_{EDL}} + \frac{1}{C_Q}$). Considering that the gate electrode area is much larger than the overall rGO's channel area, here the gate/electrolyte interface has a negligible contribution to the overall C_{EDL}.

On the contrary, the electrolyte/rGO interface is the interface that drives the overall C_{EDL}. Bearing this in mind and by taking into account the values found in literature for liquid-graphene interface, we used the capacitance value of $C_{EDL} \approx 8$ μF cm^{-2} in further calculations.[138;139]

To describe the behavior of a GFET in the electrolyte-gated configuration, one has to take into account the EDL capacitance and the quantum capacitance (C_Q) of

graphene itself.[99] As discussed in Chapter 1, C_Q depends on both the charge carriers induced by the gate and the charge impurities. The contribution of these two capacitances (C_{EDL} and C_Q) can be modeled as two capacitors connected in series as schematically represented in Figure 3.8.

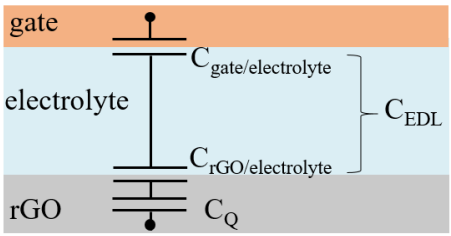

Figure 3.8: Schematic representation of interfacial capacitance model used to describe the behavior of an EG-GFET. The two capacitors in series: capacitance of the double layer (C_{EDL}) and the quantum capacitance of graphene (C_Q).

The potential drop through the device is described as[140;100]:

$$(V_{GS} - V_{Dirac}) = \frac{\hbar\,|v_F|\,\sqrt{\pi\,n}}{e} + \frac{n\,e}{C_{EDL}} \tag{3.1}$$

where V_{Dirac} is the gate potential at the Dirac point (minimum current of the transfer characteristics), v_F is the Fermi velocity in graphene ($|v_F| = 1.1 \times 10^6$ m s^{-1}) and n is the total charge carrier density per cm^2. The charge carrier density includes both the charge carriers induced by gate polarization and charge impurities (where charge impurities are known to vary from $1 \times 10^{11} - 1 \times 10^{12}$ cm^{-2}).[99] By including the C_{EDL} value, the equation 3.1 is simplified to:

$$(V_{GS} - V_{Dirac}) = 1.17 \times 10^{-7}\sqrt{n} + 2 \times 10^{-14}\,n \tag{3.2}$$

where n is expressed in cm^{-2}. By solving equation 3.2, one can convert the gate voltage range of the experimental transfer characteristics into a charge carrier density variation. Doing so, we could represent the 2D conductivity (σ_{2D}) of rGO as a function of the charge carrier density by using the following relation:

$$\sigma_{2D} = \left(\frac{W}{L}\right)^{-1} \times \frac{I_{DS}}{V_{DS}} \tag{3.3}$$

where W and L in our case are 30000 µm and 10 µm, respectively. The conductivity *versus* charge carrier density characteristics are shown in Figure 3.9. The conductivity at the CNP was found to increase dramatically for higher charge densities induced by the gate potential. Furthermore, the conductivity at the CNP was found to double its value between 1 s and 3 s of reduction. With prolonged reduction duration (6 s and 10 s), the conductivity decreased by ten times.

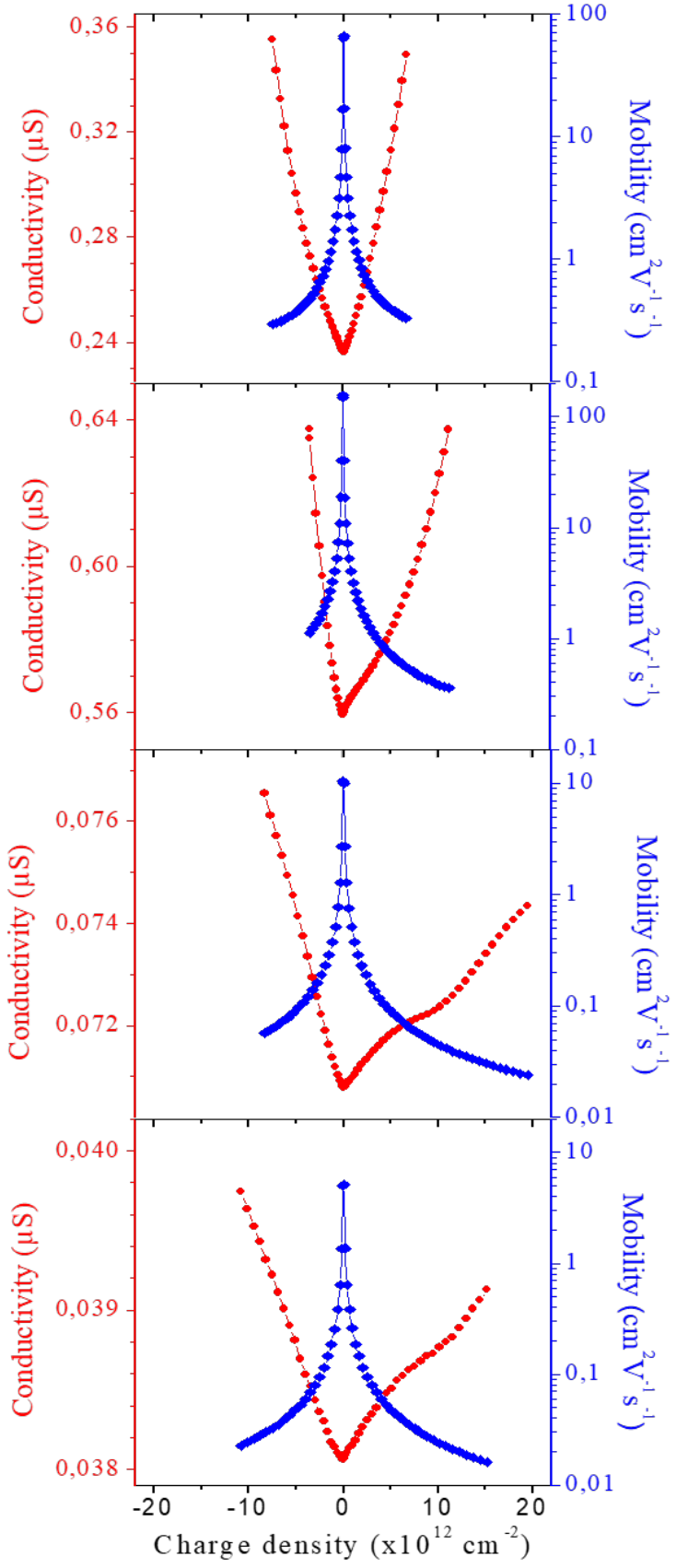

Figure 3.9: Conductivity (red) and charge mobility (blue) corresponding to each transfer curve from the Figure 3.6. From up to down: $t_{\text{red}} = 1$ s, 3 s, 6 s, 10 s.

Finally, the charge carrier mobilities can be extracted from the semi-classical Drude's model ($\mu = \frac{\sigma}{ne}$). Charge carrier's mobility related to the data in Figure 3.6 are also shown in Figure 3.9 as a function of the total charge density. The charge mobility values were found to diverge at $n = 0$, as theoretically expected. The charge transport at low charge densities can be attributed to the presence of charged impurities under the rGO layer.[140] This explanation goes hand in hand with the conductivity value for $n = 0$ observed to be different from zero whatever the reduction time is, confirming the presence of charged impurities in rGO. Outside of the CNP, for both holes and electrons, the charge mobilities were found to decrease and reach a "plateau" value at higher charge densities (typically when $n = 4 \times 10^{12}$ cm^{-2}). At this plateau, the charge transport is dominated by the carriers coming from the gate effect and thus can be used to evaluate the mobility of both charge carriers. Mobility values in function of the reduction time are shown in Table 3.1.

t_{red} (s)	μ_e (cm^2 V^{-1} s^{-1})	μ_h (cm^2 V^{-1} s^{-1})
1	0.45±0.05	0.42±0.05
3	0.86±0.07	1.10±0.07
6	0.10±0.01	0.11±0.01
10	0.06±0.01	0.06±0.01

Table 3.1: The charge carrier's mobilities calculated for electrons (μ_e) and holes (μ_h) at the edge of mobility plateau (for charge density of $n = 4 \times 10^{12}$ cm^{-2}). Reduction time is indicated for each value.

According to Drude's model, mobility variations follow the conductivity variation trend. Maximal mobility value ($\mu \approx 1$ cm^2 V^{-1} s^{-1}) was observed after 3 s of reduction where subsequently mobility dropped by a factor of 15 for increased reduction time. The mobility values obtained here for rGO are comparable with literature values from other *in-situ* reduction methods and deposition techniques.[72;71;141]

The mobility drop with the reduction time increase could be a consequence of the progressive reduction process. During the GO reduction, the oxygen groups are removed.[59] Removal of oxygen groups leaves, as a result, some defects in rGO's structure. These defects can act as scattering centers, lowering the overall apparent charge mobility for both holes and electrons.

Furthermore, the Dirac point position is observed to shift toward less positive potentials with progressive reduction. This behavior evidences the possibility of oxygen groups to act as 'dopant' species on rGO. The oxygen groups removal subsequently diminish their doping effects which, as a consequence, leads to the rGO's dedoping resulting in a Dirac point position shift. Similar behavior is described in literature in the case of graphene doping with potassium.[142] Chen et al. showed that with increased

K-doping duration, the charge mobility decreases and the Dirac point position shifts toward more negative potentials (as K atoms act as electron donors toward graphene).

For the sake of comparison, the electrical behavior of graphene flakes based transistors was studied and is presented in the following section.

3.3.3 Comparison with the graphene EG-FETs

Here, we choose to investigate the behavior of graphene flakes in the EG-FET configuration, as a reference system for our study. However, the dispersibility issue of graphene in water-based inks should be first overcome. Graphene powder was dispersed using the same procedure and the same mixture of solvents used in the GO ink formulation. The graphene flakes were drop-casted onto the interdigitated structure and characterized in the EG-GFET configuration. The obtained transfer curve is shown in Figure 3.10.

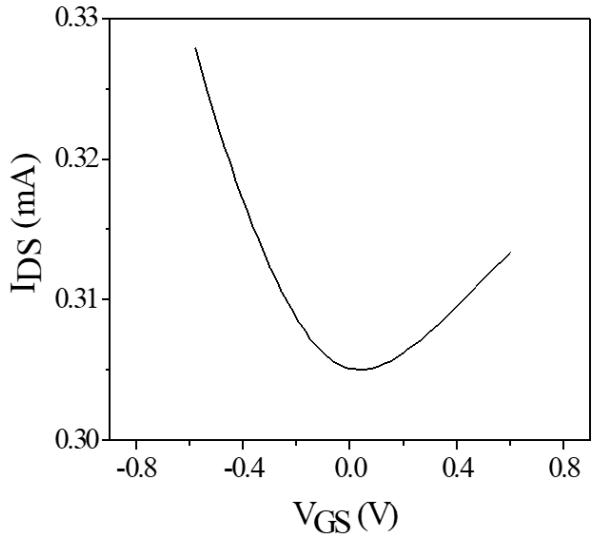

Figure 3.10: Transfer curve obtained in EG-GFET configuration (PBS as electrolyte) of drop-casted graphene flakes (V_{DS}=0.1 V).

The Dirac point position for graphene flakes FETs is found close to $V_{GS} = 0$ V ($V_{GS} \approx +50$ mV). Compared to rGO EG-FETs, where the initial Dirac point position was found close to $V_{GS} \approx 1.3 - 1.4$ V, it seems that the possible "doping effects" are much less pronounced here. The clear difference between rGO and graphene distinguished here is an additional proof that these two materials have different electrical properties. Note that for this experiment, the gate voltage window was extended toward more negative potentials, in order to clearly observe both branches of the transfer characteristics. Consequently, to avoid important difference between V_{GS} and V_{DS}, the value of V_{DS} was decreased to 0.1 V.

The data related to the characterization of graphene flakes is extracted in the same way as for the rGO samples by taking into account the contribution of C_{EDL} and C_Q

in the overall capacitance. The obtained results are shown in Figure 3.11.

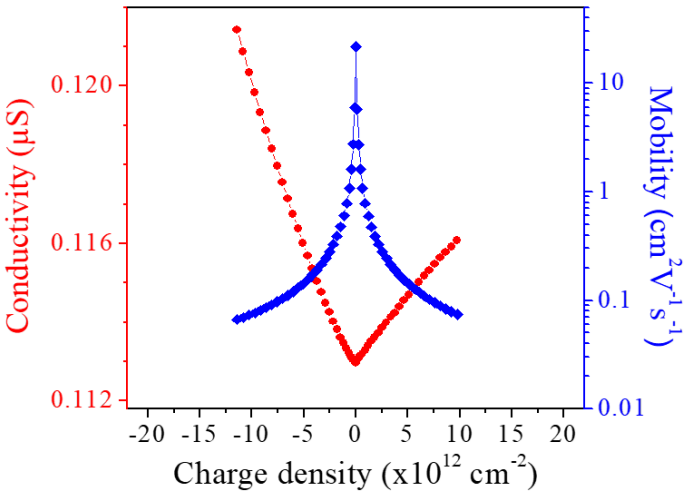

Figure 3.11: Sheet conductivity (red) and charge carriers' mobility (blue) *versus* charge carrier density related to the transfer curve obtained on graphene flakes (Figure 3.10).

The charge carriers' mobilities calculated here are 0.17 cm^2 V^{-1} s^{-1} and 0.12 cm^2 V^{-1} s^{-1} for holes and electrons, respectively. These values, situated in the range of mobilities obtained for GO reduced between 3 s and 6 s, suggest that rGO is being degraded with extended reduction to 10 s and more. This tends to confirm the assumption we made previously, about the introduction of defects in the rGO structure for long reduction times. All in all, our results show that there exists an optimum reduction duration for obtaining the maximum mobility value in rGO EG-FETs. One should note that the mobility values extracted from EG-GFETs made of graphene or rGO flakes may appear far below the ones obtained with pristine graphene GFETs. However, one should also keep in mind that the transistor's channel is elaborated here through the inkjet printing process. Consequently, the charge carrier mobilities may be limited by the hopping process between the rGO flakes, which is not the case when single-layer graphene is used as channel. Moreover, one cannot neglect the possibility of electrolyte ions penetration in between the rGO flakes. Additional studies would be needed for further understanding of the real mechanism lying behind the observed behavior.

In the next section, the effect of the organic adsorbates on rGO's electronic properties will be discussed.

3.4 Effect of nitrogen-rich molecular adsorbates on rGO

As mentioned in Chapter 1, graphene's electronic properties can be controlled through the means of molecular functionalization. Here, we envisaged the rGO doping by using non-covalent two-dimensional molecular assemblies deposited on rGO. The type of molecule designed and synthetized for this purpose is represented in Figure 3.12. The molecule is composed of two triazine groups bi-substituted by alkyl chains and separated by a phenyl group.

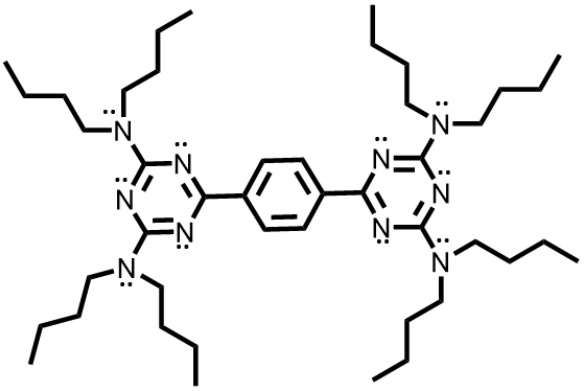

Figure 3.12: Triazine-based molecule bi-substituted by alkyl chains (here, BTZ-C_4).

Based on the same bis-triazine (BTZ) central group we have investigated two molecular structures which differ only by the length of the alkyl chains, i.e. a linear chain comprising 4 carbon atoms (labeled as BTZ-C_4) and one with 6 carbon atoms (BTZ-C_6). However, no significant differences were noticed in terms of electrical characteristics between these two molecules. In the following, the acronym BTZ-C_n will be used to represent this type of molecule, where n represents the length of the alkyl chain.

This structure was chosen to promote the two main types of non-covalent interactions: the π-stacking interactions between the plane of rGO and molecule's aromatic rings[143], and the London dispersion force between the alkyl chains and the rGO[48]. These interactions help to establish a molecular monolayer on rGO. London forces can help create intermolecular interaction. On the other hand, thanks to the presence of triazine groups, this molecule is rich in electrons coming from nitrogen atoms. As a result, we expect that a charge transfer could be established between rGO and BTZ-C_n.

As the doping effect depends on the molecule's HOMO/LUMO position with respect to the graphene's Fermi level, we were interested in extracting the HOMO/LUMO values of BTZ-molecule through electrochemical measurements. Figure 3.13 shows the cyclic voltammograms of BTZ-C_4 molecule obtained in a conventional 3-electrode electrochemical cell.

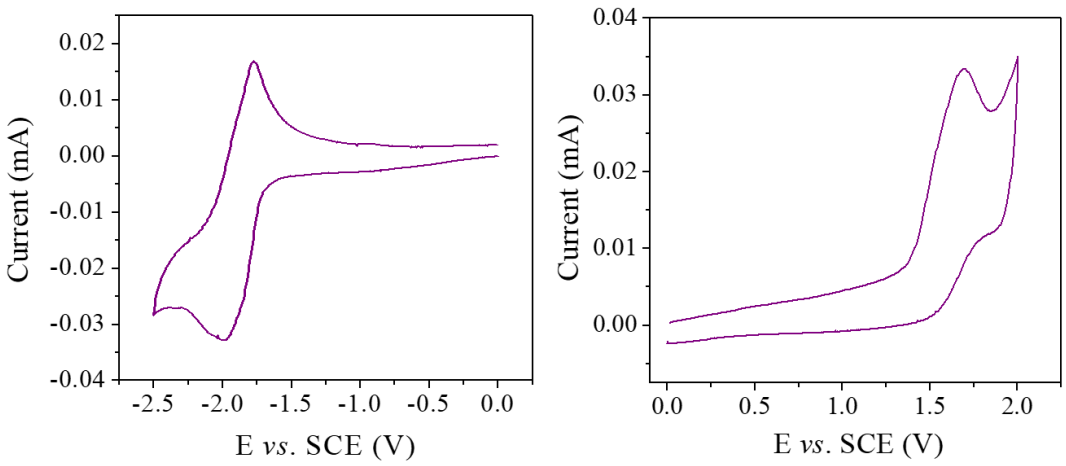

Figure 3.13: Cyclic voltammograms showing the reduction (left) and oxidation (right) waves of 1 mM BTZ-C_4 dissolved in 0.1 M $TBAPF_6$/ACN. The scan rate is 100 mV s^{-1}.

The HOMO/LUMO position can be extracted using the following relations[144;145]:

$$E_{\text{HOMO}} = -(V_{\text{onset-ox}} - V_{\text{ref}} + 4.8)\, eV \tag{3.4}$$

$$E_{\text{LUMO}} = -(V_{\text{onset-red}} - V_{\text{ref}} + 4.8)\, eV \tag{3.5}$$

where $V_{\text{onset-ox}}$ and $V_{\text{onset-red}}$ are the oxidation and reduction onsets, respectively, and V_{ref} is the ferrocene's halfwave potential (0.4 V). V_{onset} values are extracted from the reduction (Figure 3.13, left) and oxidation (Figure 3.13, right) waves: $V_{\text{onset-red}} = -1.5$ V and $V_{\text{onset-ox}} = 1.4$ V. By replacing these values in the equations 3.4 and 3.5 the HOMO/LUMO values are estimated:

$$E_{\text{HOMO}} = -5.8\, eV$$

$$E_{\text{LUMO}} = -2.9\, eV.$$

Moreover, another important information was deduced from these electrochemical measurements: the potential range within which the molecule is redox-inactive. The redox peak was observed at ≈ -2 V. As the working potential in EG-GFET is up to 1 V, we were sure that no parallel parasitic electron transfer would occur in our measurements, which could potentially interfere with the rGO's typical electrical transfer and output characteristics.

3.4.1 Functionalization of rGO

Before any electrical characterization of the BTZ-C_n influence on rGO, we were interested in studying the molecular deposition behavior through the means of AFM surface

characterization. In the case of the inkjet-printed layer, the study of molecular adsorption is tricky to achieve, since the GO layer is printed in a way to maximize the density of overlapping GO flakes. This leads to a relatively important surface roughness which may prevent the unambiguous visualization of thin molecular layers adsorbed on GO. To clearly identify the molecular adsorbates on the GO flakes, we chose to deposit the molecules on specific samples where the flakes are well dispersed on the substrate.

To achieve the proper conditions for morphological study, GO ink was diluted and drop-casted on the silicon wafer's surface. Subsequently, the BTZ-based molecules, soluble in 1-propanol, were deposited on GO by drop-casting. Figure 3.14 shows the GO dispersion before (a) and after (b) liquid-phase functionalization with the BTZ-C_6 molecule.

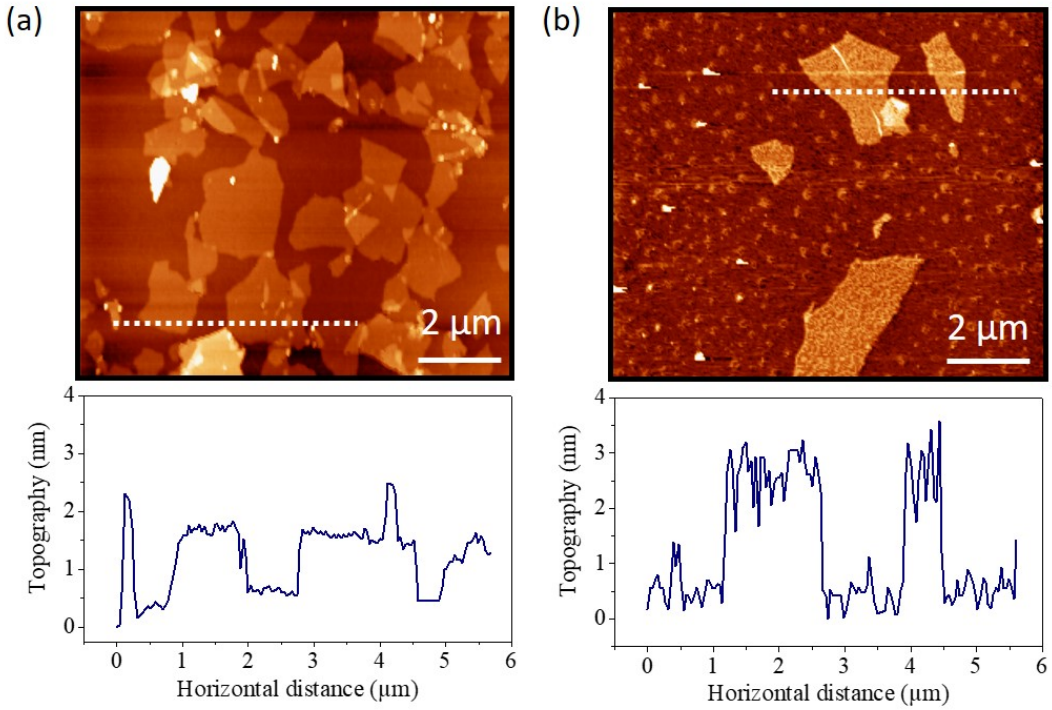

Figure 3.14: GO ink 0.1 mg mL^{-1} drop-casted on the SiO_2/Si substrate (a) before and (b) after functionalization with BTZ-C_6 (0.5 mM).

Before the functionalization step, one can observe very flat GO flakes without significant overlap. The average thickness of GO flakes is between $0.5-1.5$ nm, equivalent to approximately 1 to 5 GO monolayers. The height profile shows no significant roughness fluctuations. On the other hand, with the BTZ-C_6 addition, the roughness fluctuations became more important (in the range of ≈ 2 nm) suggesting the presence of adsorbed molecular domains of up to ≈ 3 molecular layers. Also, one can observe that the silicon substrate is entirely covered by the molecule.

Besides, the molecular adsorption of BTZ-C_6 was investigated on HOPG through thermal evaporation, which is presented as Appendix C.3. We used highly oriented pyrolytic graphite (HOPG), a model substrate with atomically flat terraces, to mimic

the molecular adsorption on graphene, which is also very flat. Moreover, the molecular deposition from the gas phase enables to obtain molecular monolayers. The presence of molecular agglomerates is observed without molecular islands, evidencing the eligibility of the BTZ-based molecules for molecular functionalization of rGO.

The morphological characterizations confirmed the successful non-covalent adsorption of BTZ-based molecule on rGO's surface. In the following subsection, the molecular influence on rGO's electronic properties will be discussed.

3.4.2 Electrical characterizations of rGO functionalized with BTZ-C_n

The BTZ-C_n molecules are expected to modify the electronic properties of rGO. Here, the goal is to detect the modification of rGO's electronic properties through the means of electrical characterizations in the EG-GFET configuration. The experiments are performed in two steps: first, GO is reduced for a fixed duration and electrically characterized. In the second step, the rGO is functionalized with BTZ-C_n and subsequently characterized.

Figure 3.15 shows a typical transfer curve obtained before and after the molecular functionalization of rGO.

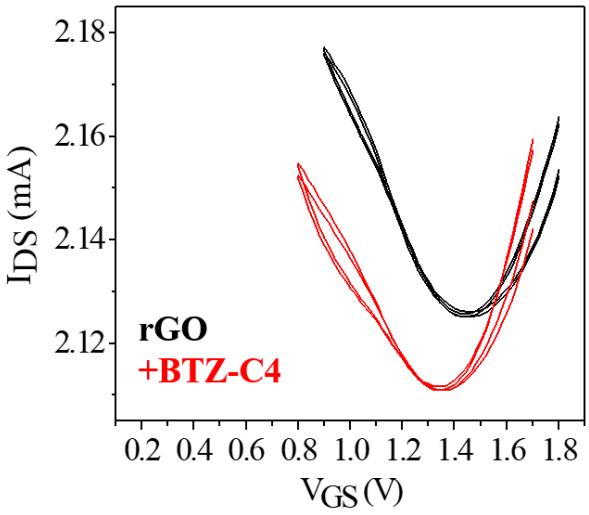

Figure 3.15: Transfer curves of rGO electrochemically reduced for 5 s (black curve) and rGO functionalized with BTZ-C_4 (red curve).

The Dirac point position after 5 s of rGO reduction is found at $V_{GS} \approx 1.45$ V. Following the molecular functionalization, the Dirac point position is found to shift toward less positive potentials, at $V_{GS} \approx 1.35$ V.

In order to discard any Dirac point shift due to the solvent in which the molecules are dissolved (1-propanol), blank experiments were performed and analyzed statistically. The printed and reduced GO layer, previously electrically characterized in MilliQ

water, was rinsed with distilled water. A small quantity of 1-propanol (0.5 µL) was subsequently drop-casted on the dry rGO layer. This step was followed by MilliQ addition for further electrical characterization. The statistical studies were performed for each step, including the molecular functionalization and are shown in Figure 3.16.

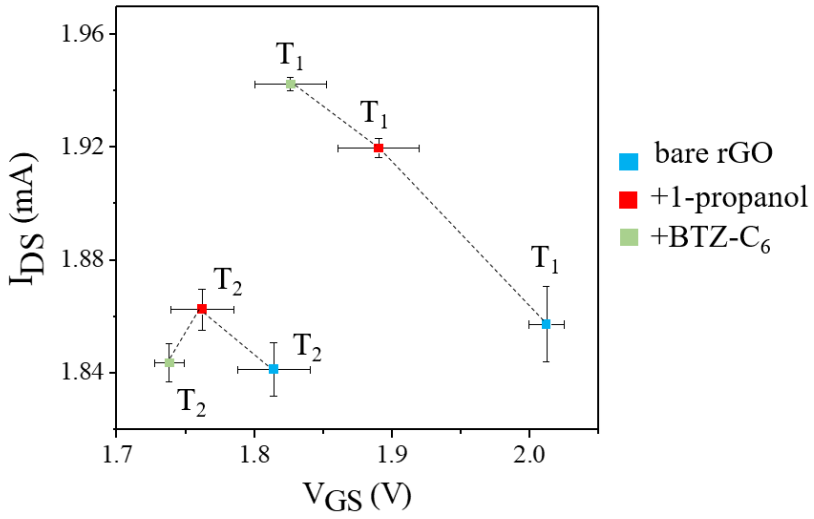

Figure 3.16: The Dirac point variations with respective current variations for bare rGO, rGO with 1-propanol and rGO functionalized with BTZ-C_6. The data is presented here for two different transistors, labeled as T_1 and T_2. Black dotted lines are given as eye guides for each transistor.

For each characterization, at least five transfer curves were recorded successively in the same conditions. Detailed data used for the statistical analysis are represented in Table C.1 and Table C.2 of Appendix C.4. The Dirac point positions for each electrical characterization are defined by taking the average of two points close to the minimum current. At first sight, the variations of current at the Dirac point are observed to occur for each step (solvent or molecule addition) without following a clear trend. For two transistors presented here, the addition of 1-propanol was followed by the shift of the Dirac point toward less positive potentials. We suppose that the residual 1-propanol caught in between the rGO flakes is the cause of this behavior. Probably due to its polarity, 1-propanol is able to influence the field-effect in the rGO's vicinity, which is the reason why we cannot entirely neglect the solvent effect (the dipole moments of 1-propanol and water are 1.68 D and 1.84 D, respectively).

With the addition of BTZ-C_6, a supplementary Dirac point shift occurs. The effect of the molecules on the Dirac point shift is observed to be larger than the one of the polar solvent. Moreover, the error bars coming from bare rGO and rGO functionalized with BTZ-CC_6 are not overlapping, which shows that it is possible to efficiently influence the rGO's electronic properties through molecular adsorption. The Dirac point shift in the presence of the molecule, could be explained by two possible effects: the

establishment of a charge transfer between the rGO and the BTZ-C_n or/and a purely capacitive effect.

The former explanation (charge transfer) relies on the fact that the Fermi level of pristine graphene is around −4.5 eV[145], although we couldn't determine precisely the Fermi level of rGO. Nevertheless, knowing that the rGO is p-doped in our case, we can be sure that the rGO's Fermi level is located in its valence band (below −4.5 eV). Taking into account previously calculated molecule's HOMO and LUMO energies, which are −5.8 eV and −2.9 eV respectively, it is possible that the HOMO level of the molecule may be higher than the rGO's Fermi level. If so, charge transfer should occur from the molecule toward rGO leading to its dedoping (i.e. increase of Fermi level), as represented in Figure 3.17.

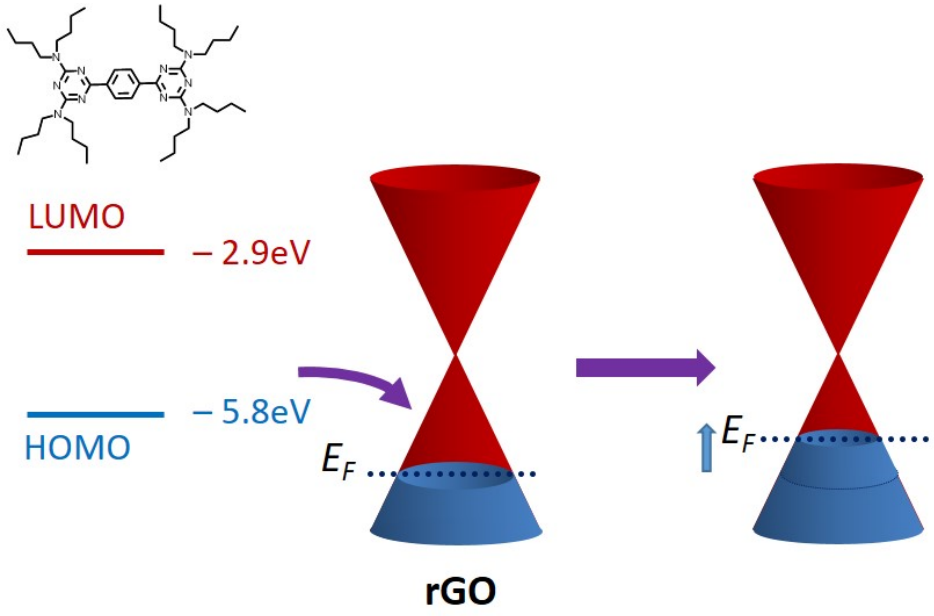

Figure 3.17: Schematic energy band structure representation of expected HOMO/LUMO BTZ-C_6 position according to the estimation of respective rGO's Fermi level position.

For the latter possible explanation, the BTZ-C_n molecule, as previously mentioned, is very rich in electrons. Due to this, the layer of BTZ-C_n can act as a local gate able to influence the rGO's electronic properties through capacitive effects. The adsorption of negatively charged BTZ-C_n molecule is supposed to cause the accumulation of positive charges in rGO. As rGO is initially p-doped, that would cause a further Dirac point shift toward more positive potentials, which is not observed to occur here. For this reason, the assumption of the charge transfer is more likely to explain the observed Dirac point upon the functionalization of rGO with BTZ-C_n.

3.5 Conclusions

In this chapter, the study of rGO's electronic properties in the EG-GFET configuration was presented. The formulation of GO printable ink, here described, allowed us to use the inkjet printing technology for device fabrication and to obtain an EG-GFET in a timely, efficient manner. The as-printed GO layer was subsequently electrochemically reduced using an *in-situ* approach, where the rGO was obtained directly on the gold bottom-contact photolithographed structure.

The reduction process was shown to have an important influence on the rGO's electrical properties. Notably, the Dirac point position and apparent charge mobility of both holes and electrons were observed to change. The Dirac point shift toward less positive potentials with increased reduction duration was correlated to the change of possible doping effects coming from the oxygen groups, which are removed through the progressive reduction process. In addition, the appearance of new scattering centers induced by defected rGO structure could be the cause of damping charge carriers' mobility. However, at this stage, we cannot be completely sure of the actual process which occurs here. Further investigations would be needed to discriminate the actual process, which can be one of the future studies' perspective.

Even though single-layer graphene is not used here, we were able to obtain the typical electrical characteristics of graphene-based materials on the inkjet-printed rGO layer. Moreover, we were able to modulate the rGO's Fermi level through the adsorption of BTZ-based molecules. As a perspective, the electrochemical reduction tuning combined to the molecular doping could be further investigated. The rGO's band gap could be firstly modulated through the electrochemical approach (by controlling the reduction duration) followed by the molecular functionalization step.

Thus, the rGO EG-FET device developed here is ready to operate in the liquid media. We have used it as a biosensor to monitor the life cycle of photosynthetic organisms, which will be discussed in the next chapter.

Chapter 4

rGO EG-FET as a biosensor

Chapter 4

rGO EG-FET as a biosensor

In this chapter, the rGO EG-FET device will be described in the light of a biosensing application. More precisely, this device was used for the life-cycle monitoring of photosynthetic organisms, in particular through the monitoring of an electron transfer process. We will then take a look at how electron transfer processes could be transduced by electrolyte-gated transistors. For that, the photosynthetic activity was investigated in three different transistor configurations, which will be discussed in the following sections. As a perspective, the device was shown as potentially eligible for the qualitative detection of water pollutants.

4.1 Light-induced electron transfer detected in transistor configuration

The electron transfer is a "heart reaction" of every photosynthetic activity. Transistors' properties, described previously, could be used to amplify and detect these kinds of reactions occurring at the gate/electrolyte or at the electrolyte/channel interface.

Di Lauro et al. reported on the integration of the bacterial reactive center acting as the photoactive material in an electrolyte-gated organic transistor (electrolyte gated organic field-effect transistor (EGOFET) and an organic electrochemical transistor (OECT).[146] Schematic representation of their light-responsive electrolyte-gated (LEGOT) device is given in Figure 4.1 a. It was composed of an indium tin oxide (ITO) gate electrode functionalized with the photoreactive center and separated by an electrolyte from the semi-conducting channel. Upon device illumination, a charge distribution was induced and was found to modulate the drain-source current (I_{DS}). As shown in Figure 4.1 b., upon photon adsorption, an overall increase in the device current is recorded as a result of the charge accumulation in the organic semi-conductor active layer. A similar behavior was observed in the OECT configuration (Figure 4.1 c.), but with a different current evolution trend. For the EGOFET, the current satu-

ration is observed earlier than in the case of an OECT.

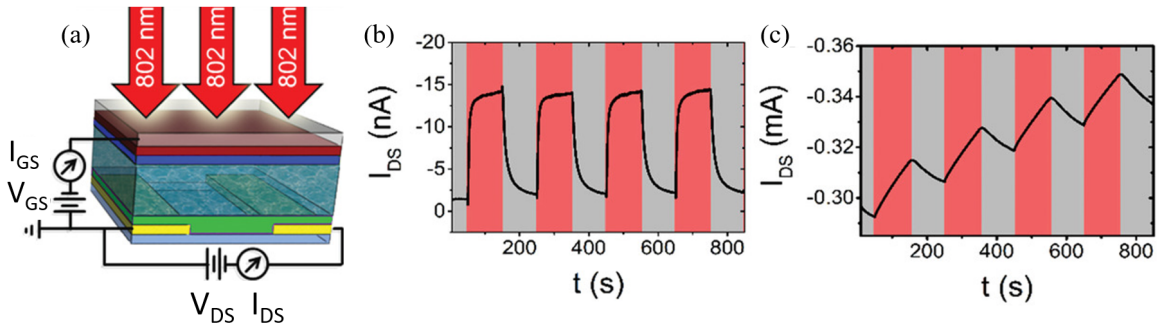

Figure 4.1: a) LEGOT device; Chronoamperometric measurements recorded upon the dark-light cycles in the b) EGOFET and c) OECT configurations.[146]

The authors described this behavior as a result of different gating mechanisms in these two configurations. In the case of an EGOFET, the applied gate voltage causes charge accumulation in the semi-conductor, while in the case of an OECT it is the charge depletion which takes place. Since charges have to penetrate and physically leave the semi-conductor in the OECT, the kinetics is slower than in the case of the interfacial processes occurring in the EGOFET.

Concerning graphene-based field-effect transistors, in a recent work, Nishiori et al. presented a first solution-gated GFET serving as a photosensing system based on proteins.[147] In their approach, CVD graphene was functionalized with gold nanoparticles (AuNPs) for the biological photosystem attachment (Figure 4.2, left).

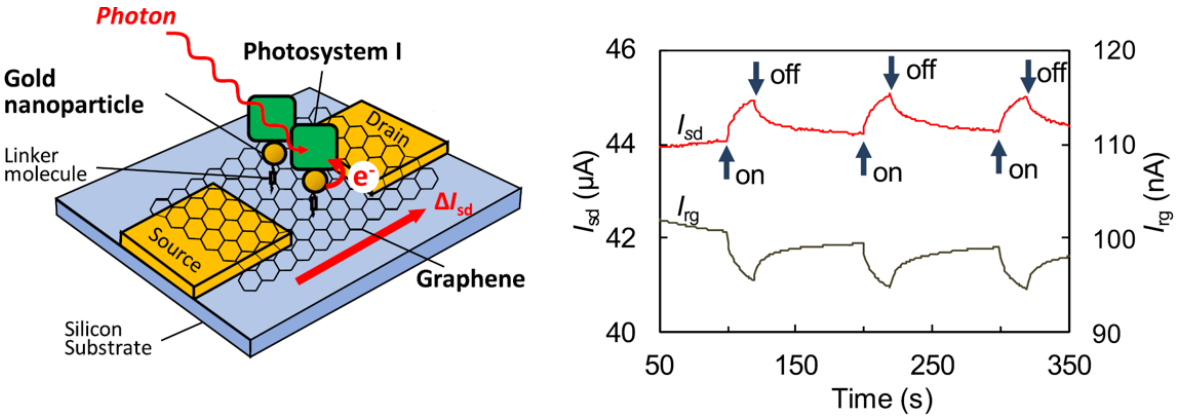

Figure 4.2: Left: Schematic representation of a graphene-based FET device for photosensing. Right: Photoresponse of the graphene-based gated FET upon alternation of ON/OFF cycles (V_{GS} = 0.1 V, V_{DS} = 0.1 V).[147]

The device illumination resulted in an overall device current increase, while the current decrease was observed in the absence of light (Figure 4.2, right). The observed electrical behavior upon exposure to light was attributed to the established electron transfer between the photosystem and the AuNP then to graphene. Besides, the au-

thors suggested a possibility of graphene doping effects caused by the light-induced electron transfer. There is no other example so far in the literature.

One part of the work of this thesis was performed using a similar approach: the CVD graphene layer covered with molecular carpet for the attachment and the detection of biological samples, but this time in the back-gated GFET structure. The research project and the obtained results are presented in Appendix A.

In this chapter, we were not interested in studying internal electron transfer processes occurring inside the multi-protein complex of the photosystem II in microorganisms. Instead, we monitored one of the photosynthetic activity results, namely oxygen production.

4.2 Cell monitoring generalities

Here, the idea is to monitor the life-cycle of photosynthetic organisms with the goal of probing the environmental quality, notably the quality of waters. Indeed, safe and good quality waters are an essential need for humans. Nevertheless, contaminated or chemically polluted waters are causing numerous deaths around the world. According to the World Health Organization (WHO), about 829.000 people are estimated to die each year as a consequence of polluted waters.[148] Rapid detection of polluted water is, therefore, an important necessity.

Commonly used methods for this purpose, such as liquid and gas chromatography, are among the most accurate.[149] However, at the same time, signal acquisitions are very time-consuming. Due to large equipment that is hard to make portable, such traditional methods are usually based on the analysis of samples collected in the field but analyzed later in a remote laboratory. The use of biosensors bring the advantage of possible device miniaturization according to one's need, providing a small and portable device for rapid on-site and *in-situ* analysis of small sample volumes. Besides, biosensors allow to couple the analysis of biological samples and microelectronic systems, which enables the rapid and accurate detection of different substances in, for example, waters.[150] The photosynthetic organisms such as micro-algae are widely used in environmental monitoring thanks to their efficient photosynthetic activity and their easy-growing and cost-effective maintenance.[151] Moreover, algae do not require special sample-pretreatments, can adapt to diverse environments and can be easily integrated into biosensing devices.[152] Environmental monitoring using photosynthetic organisms can be achieved in an optical-biosensor setup where the changes in chlorophyll fluorescence are tracked[153;154] or through the photocurrent monitoring as a result of electron transport during the photosynthesis.[155].

Like all photosynthetic organisms, micro-algae are able to convert carbon dioxide and water into sugars using sunlight energy. The following overall equation describes

the process:

$$6CO_2 + 6H_2O \longrightarrow C_6H_{12}O_6 + O_2 \tag{4.1}$$

According to equation 4.1, oxygen is released through photosynthetic activity, which is catalyzed by light. On the other hand, oxygen is consumed by photosynthetic organisms in the process of cell breathing, which occurs anytime, but is the only process occurring in the absence of light:

$$C_6H_{12}O_6 + O_2 \longrightarrow 6CO_2 + 6H_2O \tag{4.2}$$

By following the variations of O_2 concentration in the microalgae's surroundings, one can estimate their photosynthetic activity. The presence of pollutants, such as heavy metals or herbicides, could disrupt the photosynthetic activity, resulting in oxygen production decrease, itself transduced into a biosensor's output signal change.

Electrochemical biosensors based on monitoring the algal metabolisms (respiration and photosynthesis) have already been described to detect herbicides such as diuron, triazine, atrazine.[156;157;158;159] In a recent work, Tucci et al. reported on amperometric biosensors following the life-cycle of cyanobacteria *Anabaena variabilis* immobilized on carbon felt electrodes using an alginate gel.[160] A redox mediator was used to enhance the electron transfer between the living cells and the electrode surface. Figure 4.3 (left), shows the amperometric signal obtained in the presence (red) and the absence (blue) of the cyanobacteria.

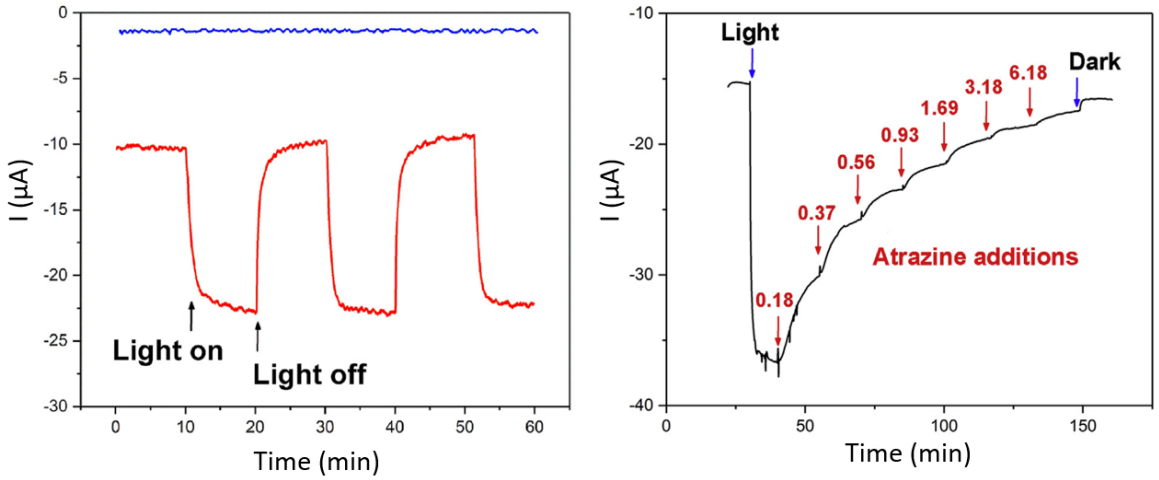

Figure 4.3: Left: The chronoamperometric measurements (E=0.5 V *vs.* SCE) in the presence of cyanobacteria *Anabaena variabilis* (red curve) and in its absence (blue curve). Right: The effect of atrazine additions on the cyanobacteria's photocurrent (concentrations of atrazine are indicated by red numbers and are expressed in µM).[160]

Upon the cyanobacteria illumination the current is observed to increase, while in the obscurity the current decreases. The presence of herbicides, such as atrazine and

diuron, was investigated as well. Figure 4.3 (right), shows the cyanobacteria amperometric monitoring with atrazine additions. The current was observed to drop with each addition of increased atrazine concentration. For the highest atrazine concentration, the current dropped almost to the value obtained in the dark. The herbicide inhibits the photosynthetic electron transport, which is observed to be concentration-dependent.

Besides, living cells have already been studied as a part of the "living" electrolyte or "living" gate in transistors such as OECTs and EGOFETs for monitoring the release of cells' biochemicals (e.g., neurotransmitters, glucose).[161] Our idea here is to merge the two approaches in an EG-GFET.

In a recent work, Le Gall et al. described, for the first time, the use of an EGOFET for the monitoring of photosynthetic microorganisms.[162] The living cell culture, the cyanobacteria *Anabaena flos-aquae*, was used here as an electrolyte where the photosynthetic activity was monitored through oxygen reduction at a platinum gate electrode surface. Transistor's channel was made of poly(N-alkyldiketopyrrolopyrolle dithienylthieno[3,2-b]thiophene) (pDPP-DTT). Figure 4.4 shows an amperometric measurement in the EGOFET configuration.

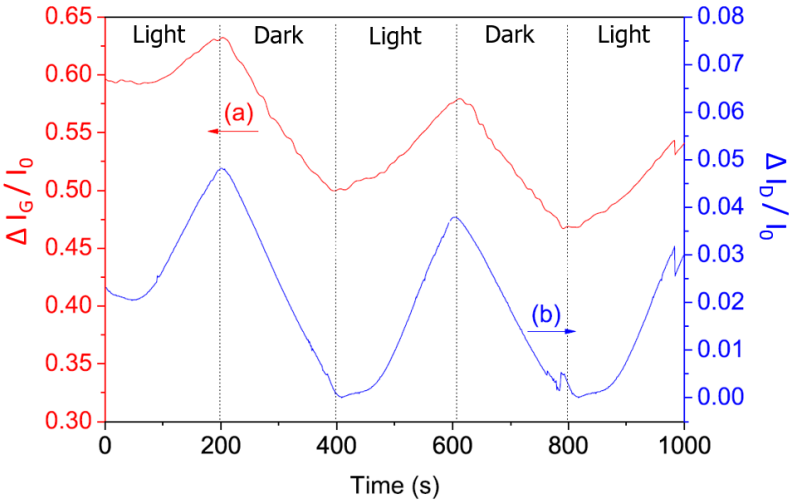

Figure 4.4: Amperometric measurements in the EGOFET configuration with cyanobacteria in the electrolyte, recorded upon the "day/night" cycles ($V_{GS} = -0.8$ V, $V_{DS} = -0.6$ V). The red curve (a) and the blue curve (b) represent the variation of gate and drain current, respectively.[162]

The results show that there is an immediate increase of the device gate current upon cell illumination due to the oxygen release in the solution and its reduction at the gate surface. On the other hand, under dark conditions, the gate current was found to decrease, which indicates that the oxygen concentration decreased as a result of the cell breathing process. The gate current was amplified on the drain with an amplification factor of $\Delta I_{DS}/\Delta I_{GS} \approx 750$. In addition, the advantage of the EGOFET configuration is a very low operating voltage (below 1 V) allowing to work with sensitive

biological samples, avoiding their degradation due to the applied voltage.

To our knowledge, the EG-GFETs have not been described yet for this purpose. However, as discussed in Chapter 1, graphene was shown to be a sensitive platform for bio-detection purposes. The results presented in Chapter 3 showed that the amplification factor I_{DS}/I_{GS} obtained in our device based on rGO EG-FET is up to the million, which is much larger than in the case of the EGOFET. Another advantage of rGO over semi-conductors is its stability, in particular in aqueous media.

In the following section, cell monitoring will be presented in a classic electrochemical configuration (conventional 3-electrode electrochemical cell) as well as in the rGO EG-FET configuration.

4.3 Toward monitoring of photosynthetic activity in the rGO EG-FET configuration

The oxygen reduction reaction (ORR) is one of the most important reactions as a part of the breathing process in the living world around us. As the ORR kinetics is very slow, this reaction needs the support of a catalyst to be well detected.[163] The most suitable catalytic material for ORR is platinum. The oxygen reduction on platinum involves the transfer of 4 electrons according to the reaction[164]:

$$O_2 + 4H^+ + 4e^- \rightarrow 2H_2O \tag{4.3}$$

In the first study of the photosynthetic activities in EGOFET configuration, platinum electrodes with an area significantly smaller than that of the semiconductor, were the most efficient for detecting oxygen reduction at the gate/electrolyte surface. This is explained by the fact that the potential drop across the gate/electrolyte interface is much larger than the one at the electrolyte/channel interface by using small gate diameters. As discussed in Chapter 1 (section 1.4.1, paragraph "Electrolyte-gated GFET") the overall double layer capacitance within the transistor $\frac{1}{C_{EDL}} = \frac{1}{C_1} + \frac{1}{C_2}$ is driven by the contributions of the gate/electrolyte (C_1) and electrolyte/graphene (C_2) interfaces. If the potential drop at the gate/electrolyte interface is large, then the potential drop at the other interface is small, meaning that the gate voltage seen by the semiconductor is low and ineffective. Therefore, for a sensing mechanism which occurs on the gate, one must find a trade-off between a very small gate providing good sensitivity and a large gate providing high drain currents.

The oxygen reduction on a Pt electrode in aqueous media is expected to occur between -0.5 and -0.8 V (*vs.* Ag/AgCl), with an optimum value of -0.6 V *vs.* Ag/AgCl.[162] To be able to determine the best values of V_{GS} and V_{DS} to apply on our EG-GFET, we measured the real electrochemical potential of the gate electrode E_G

versus Ag/AgCl pseudo-reference electrode for gate voltages (i.e., a potential difference between gate and source) between −0.5 V and −1.7 V. The illustrating scheme of the setup used is represented in Figure 4.5, left.

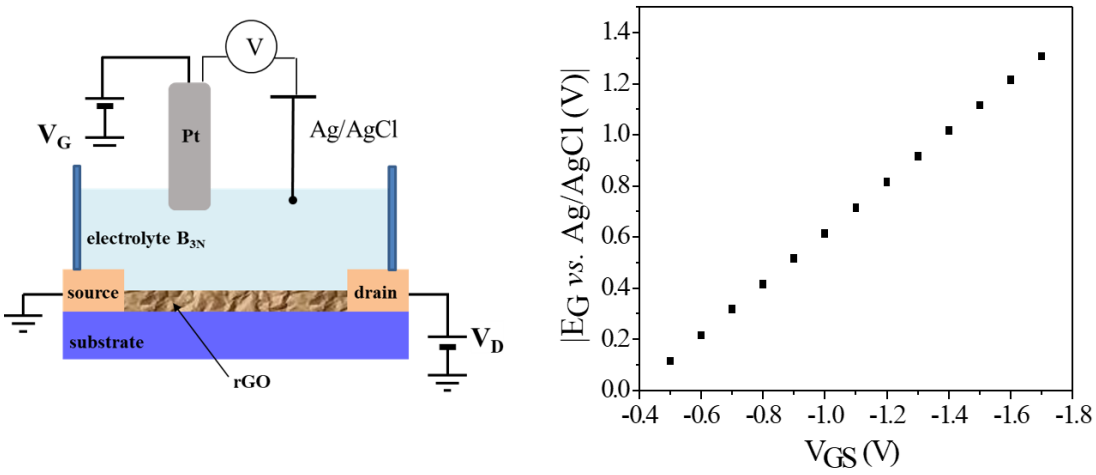

Figure 4.5: Left: The configuration used for the measurement of electrochemical potential. Right: The electrochemical potential of the Pt gate electrode ($\varnothing$ = 100 µm) measured *vs.* an Ag/AgCl pseudo-reference electrode in the rGO EG-FET configuration ($V_{DS} = -0.9$ V).

For this experiment, the platinum electrode served as a gate electrode ($\varnothing$=100 µm) and a fourth electrode Ag/AgCl wire is exceptionally added as a reference electrode. The electrolyte used was the aqueous Bold's basal medium (B_{3N}). Knowing the fact that the transfer curves in Chapter 3 were recorded by keeping constant the V_{DS} value of 0.9 V, we kept here the same, but negative value. The goal is to prevent too large voltage drops between the applied gate and drain voltages, which may cause some parasitic reactions. The obtained results are presented in Figure 4.5, right. These results show the linear variation of the electrochemical gate potential ($E_G = V_{GS} - V_{ref}$) with the applied gate voltage (the data used in this plot and I_{DS} and I_{GS} values for each point can be found in Table D.1). The optimal potential for O_2 reduction ($E_G \approx$ 0.6 V) is deduced from the plot, corresponding to $V_{GS} = -1$ V.

4.4 Life cycle monitoring of photosynthetic cyanobacteria

The photosynthetic monitoring was conducted in three different rGO EG-FET configurations to probe the sensitivity of different interfaces for cell monitoring: 1) when the cyanobacteria are added in a liquid electrolyte, 2) with the gate electrode functionalized with immobilized cyanobacteria and 3) with an alginate gel containing cyanobacteria

used as electrolyte. The details concerning the cyanobacteria's preparation, gate functionalization and the alginate gel preparation can be found in Chapter 2 (section 2.5). In the next paragraph, the study of cyanobacteria's photosynthetic activity when added in a liquid electrolyte will be discussed.

4.4.1 Cyanobacteria as electrolyte in the rGO EG-FET configuration

The rGO EG-FET configuration used here is represented in Figure 4.6.

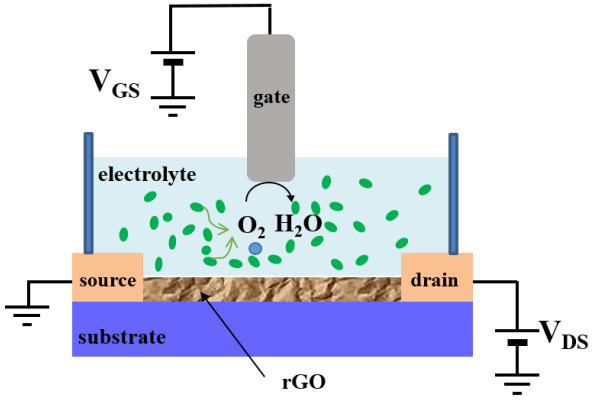

Figure 4.6: Schematic representation of the rGO EG-FET configuration with the Bold's basal medium containing cyanobacteria, used as electrolyte.

Compared to the configuration used in Chapter 3, here the gate electrode material is Pt and the electrolyte was replaced with the aqueous Bold's basal medium (B_{3N}) containing cyanobacteria. The printed GO layer was reduced for a given duration (1 s or 5 s) and the photosynthetic activity was investigated through the alternation of "day/night" cycles using a white light lamp. As demonstrated in the case of the very first EGOFET used to follow the algal photosynthetic metabolism, the oxygen release is expected to be detected via its reduction at the gate surface. Figure 4.7 (left) shows the amperometric study of the algae's metabolic activity. For the sake of clarity, the results are rescaled and the raw data can be found in the Appendix D. Upon illumination, one can observe the overall increase of both drain and gate currents. On the other hand, when the device is kept in obscurity, an overall current decrease is observed. If we compare the drain (mA range) and gate (nA range) currents, we can conclude that the amplification factor is of one million. Compared to the EGOFET, the rGO EG-FET device seems much more sensitive for this application.

As a reference, the same experiment is performed but in the B_{3N} culture medium without cyanobacteria (Figure 4.7, right). From the obtained results, we can see that both drain and gate currents' behavior is now different since the cyanobacteria are not present in the solution. We can also discard the contribution of the photocurrent under

illumination. Finally, we can be sure that the current variations observed in Figure 4.7 (left) are coming from the photosynthetic activity of cyanobacteria, i.e., oxygen production.

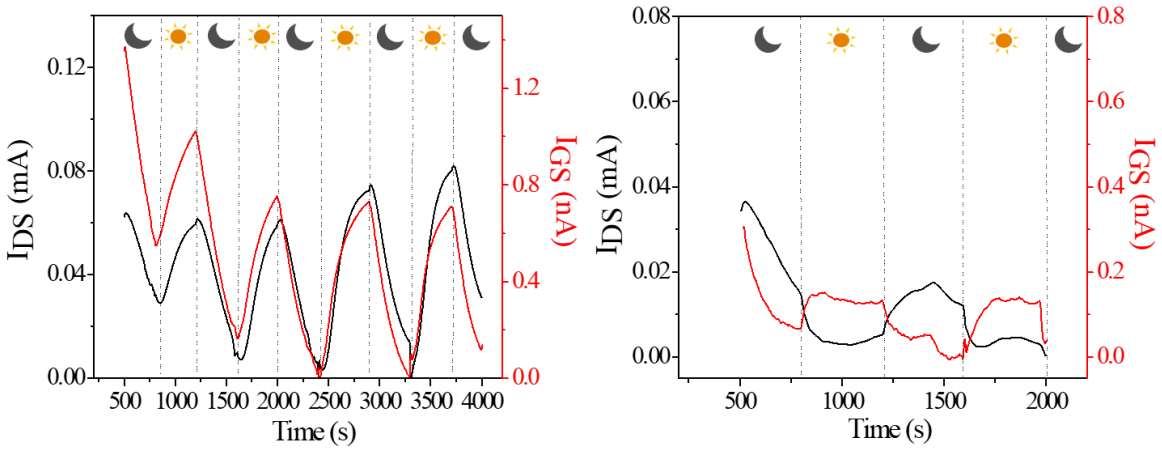

Figure 4.7: Drain (black curve) and gate current (red curve) recorded in the rGO EG-FET amperometric measurement ($V_{GS} = -1$ V, $V_{DS} = -0.9$ V, $t_{red} = 1$ s) by using cyanobacteria as electrolyte (left) and the B_{3N} culture medium without cyanobacteria (right). Presented curves are rescaled, the raw data is presented in Appendix D.1. The day/night cycles are represented with sun/moon schemes, respectively.

These results are the proof of concept of a successful algal's metabolic monitoring in the rGO EG-FET configuration.

Besides, the photosynthesis was also probed upon a gate voltage V_{GS} of -0.5 V, significantly lower than the voltage needed to reduce oxygen on the gate. As shown in Figure 4.8, it resulted in a negligible gate current.

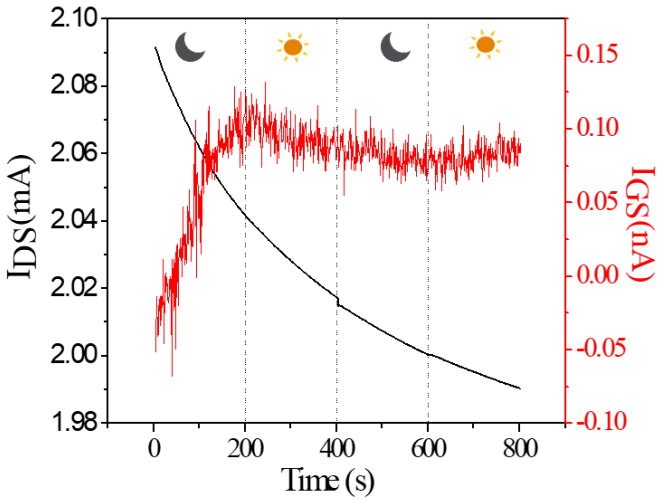

Figure 4.8: Amperometric measurement in cyanobacteria electrolyte, at a gate potential for which no oxygen reduction can occur ($V_{GS} = -0.5$ V, $V_{DS} = -0.9$ V, $t_{red} = 1$ s).

4.4.2 Electrode functionalization with cyanobacteria

As in our case there is a possibility of oxygen reduction at the graphene surface, we wanted to change the localization of algae to see if the gate/electrolyte interface is more sensitive for cell monitoring. To do so, the algae were immobilized at the gate electrode surface through gate functionalization.

The gel entrapment technique is one of the most used for the immobilization of algae. Algal gel entrapment can be achieved by using anchoring materials such as proteins (egg white, collagen or gelatine), polymers (polyurethanes, photocrosslinkable resins or acryl amide) or natural polysaccharides (alginates, carrageenans, agars).[165;166]. In this work, calcium alginate was used as a biocompatible encapsulation matrix. The system was first investigated in a classic electrochemical cell followed by electrical characterizations in the rGO EG-FET configuration.

The proof of concept of cyanobacteria's life-cycle monitoring in an electrochemical cell was described too by Le Gall et al.[162] In collaboration with Dr. Le Gall (former PhD student in the team), the photosynthetic activity was investigated on functionalized macro and microelectrodes in a classic 3-electrode electrochemical cell.[167] As the alginate hydrogel is not supposed to naturally stick onto the Pt surface, the idea was to functionalize the electrode by electroreduction of diamines. At neutral pH (our operating conditions with algae, pH≈ 7.4), it would ensure the presence of positively charged amine groups (NH_3^+) once the electroreduction is performed. On the other hand, the negatively charged COO^- groups from alginate hydrogels would allow the cyanobacteria's electrostatic immobilization at the Pt surface.

Detection in a conventional electrochemical 3-electrode setup

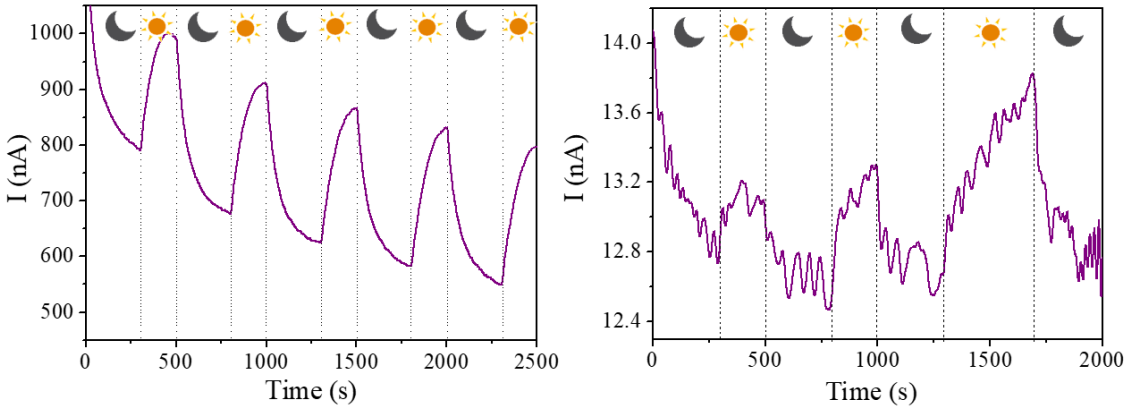

Figure 4.9: Amperometric study of the photosynthetic activity in the electrochemical cell using commercial functionalized Pt macroelectrode (left, ⌀ = 2 mm) and the functionalized Pt microelectrode (right, ⌀ = 100 µm).

Figure 4.9 shows the amperometric study of functionalized macro and micro Pt electrodes in a conventional 3-electrode setup. In the macroelectrode case, the photosynthetic activity was well detected, while in the case of the microelectrode, the photosynthetic activity signal is weaker and noisy. This demonstrated the importance to find an amplification strategy when small electrodes are used.

Detection in the rGO EG-FET upon gate functionalization

Following the gate functionalization, the electrical characterizations were performed in the setup schematically represented in Figure 4.10 (left) using the B_{3N} culture medium as electrolyte. Figure 4.10 (right) shows the gate and drain current obtained in the rGO EG-FET configuration upon alternating "day/night" cycles.

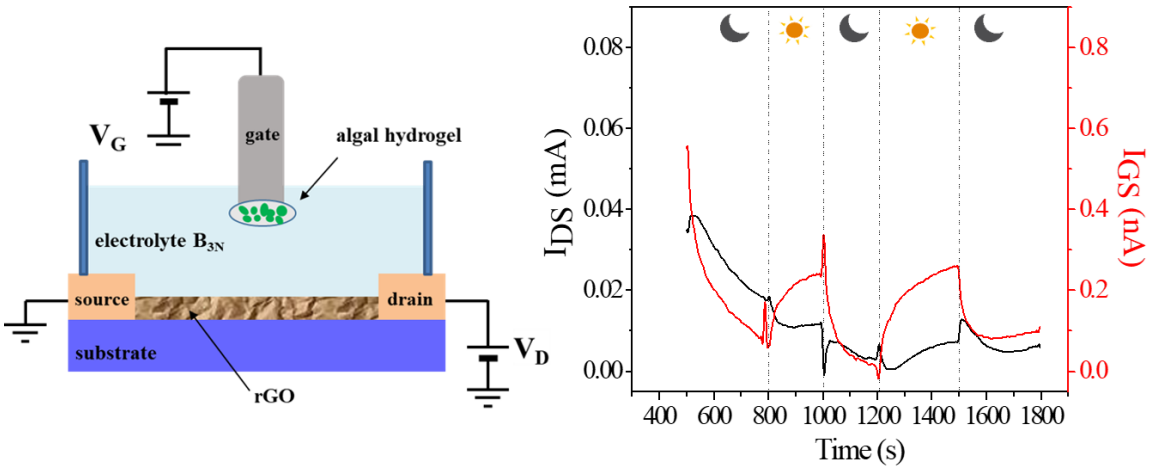

Figure 4.10: Left: Schematical representation of rGO EG-FET configuration with functionalized Pt gate electrode. Right: Rescaled amperometric characteristic upon gate functionalization with algal hydrogel. $V_{GS} = -1$ V, $V_{DS} = -0.9$ V, $t_{red} = 1$ s. The raw data is presented in Appendix D.2.

In these conditions, one could observe a gate current increase upon illumination, but very weak drain current variations. These results made us suspect the possibility that part of the drain current measured in the case of cyanobacteria added in the electrolyte (and not on the gate only) could be due to direct electroreduction of oxygen on the rGO channel. However, this has to be further investigated.

For this reason, the photosynthetic activity was also probed with the cyanobacteria hydrogel acting as an electrolyte which may be a more convenient configuration for investigating pollutants' influence, as discussed in the following subsection.

4.4.3 Cyanobacteria alginate hydrogel as electrolyte in rGO EG-FET

Solid-state electrolytes, such as polyelectrolytes or polymer electrolytes, were already described for use in field-effect devices, displaying fast electrical response and low working voltages (<1 V) like in the case of liquid electrolyte.[168;169;170;171]. The use of hydrogels was reported for biodetection applications in FET configuration, such as bulk DNA hydrogel for aptamer recognition which were shown to work with and without a liquid electrolyte.[172]

Here, the idea is to perform the electrical measurements in a gel electrolyte into which are entrapped the cyanobacteria. The rGO EG-FET configuration used here is shown in Figure 4.11 a.

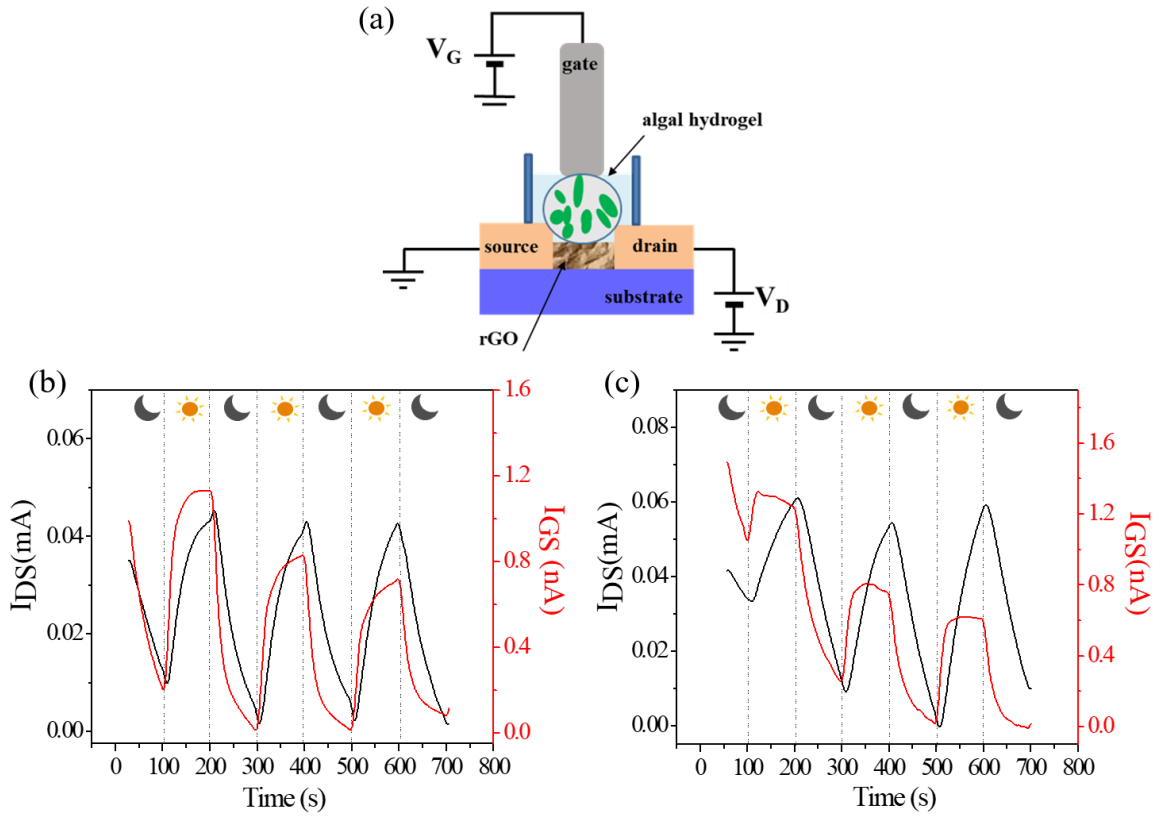

Figure 4.11: a) The scheme of the rGO EG-FET configuration with algal hydrogel acting as a solid electrolyte; Characterization of cyanobacteria hydrogel performed in the rGO EG-FET configuration ($V_{GS} = -1$ V, $V_{DS} = -0.9$ V, $t_{red} = 5$ s) using Pt (b) gate electrode (⌀= 100 µm) and Au (c) gate electrode (⌀= 250 µm). The curves are rescaled and raw data is presented in Appendix D.3.

The hydrogel was kept in ≈ 50 µL of culture medium B_{3N}, enabling the hydrogel to be kept sufficiently wet and swelled during the electrical measurements. As schematically represented, the hydrogel containing the cyanobacteria is in physical contact with both the gate electrode and the rGO. Compared to the channel geometry, the size of

the cyanobacteria hydrogel "drop" is approximately three times higher, so that the channel is entirely covered. The electrical characterizations in this configuration are shown in Figure 4.11 b. The photosynthetic activity was recorded in the same way as when the cyanobacteria were used as a liquid electrolyte. The amplification factor stayed similar. The catalytic activity of gold electrode toward the detection of oxygen activity was also investigated. Comparing the results obtained by using a gold gate electrode (Figure 4.11 c.) and taking into account that its diameter is 2.5 times higher than the Pt electrode diameter, the oxygen activity is recorded with greater amplification in the case of Pt. This is not surprising, as platinum is known as a better catalyst for oxygen reaction, compared to gold. The pollutant's influence was investigated using the Pt electrode and will be presented in the following text.

Pollutants detection

Water contaminations caused by pesticides presence are very frequent. In France, the 2013 surveillance program revealed that 92 % of collected water samples were polluted by pesticides, among which more than 80 % contained herbicides.[173] European commission listed diuron (3-(3,4-Dichlorophenyl)-1,1-dimethylurea) as one of the priority hazardous herbicides.[174] Diuron is often used to fight against weed on agricultural crops and noncrop lands, and often contaminates surface and ground waters.[175] In effect, diuron inhibits the photosynthesis process of plants by blocking the electron transfer in the photosystem reactive center.[176] Here, the pollutant's influence on the photosynthetic activity was investigated by incubating the algal hydrogel in a solution containing diuron, followed by electrical characterizations.

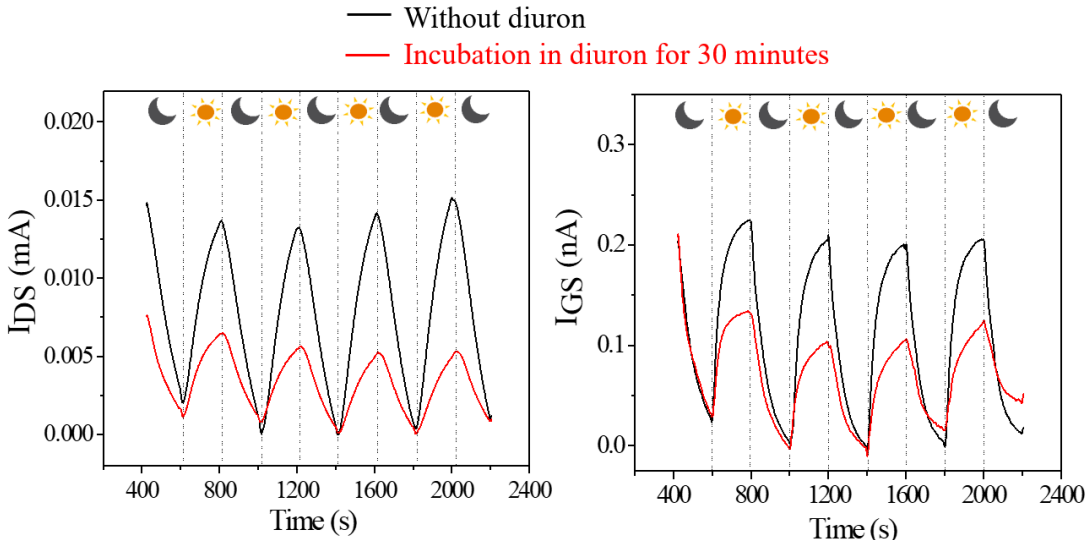

Figure 4.12: Drain current (left) and gate current (right) obtained in the algal hydrogel before (black curve) and after (red curve) incubation for 30 minutes in 1 µM diuron solution ($V_{GS} = -1$ V, $V_{DS} = -0.9$ V, $t_{red} = 5$ s). Raw data is shown in Appendix D.4.

Figure 4.12 shows the drain and gate currents of the rGO EG-FET device obtained before (black curve) and after (red curve) incubation in diuron. The incubation of algal hydrogel was performed here for 30 minutes in 1 µM diuron solution. From the obtained results it is observed that the diuron's presence decreases the photosynthetic activity. In fact the amplitude of the gate and drain current variations decreases, compared to the current amplitude obtained without diuron. In another experiment, the algal hydrogel was incubated in diuron for 24 hours. The results presented in Figure 4.13 a., show that the photosynthetic activity was completely affected in this case.

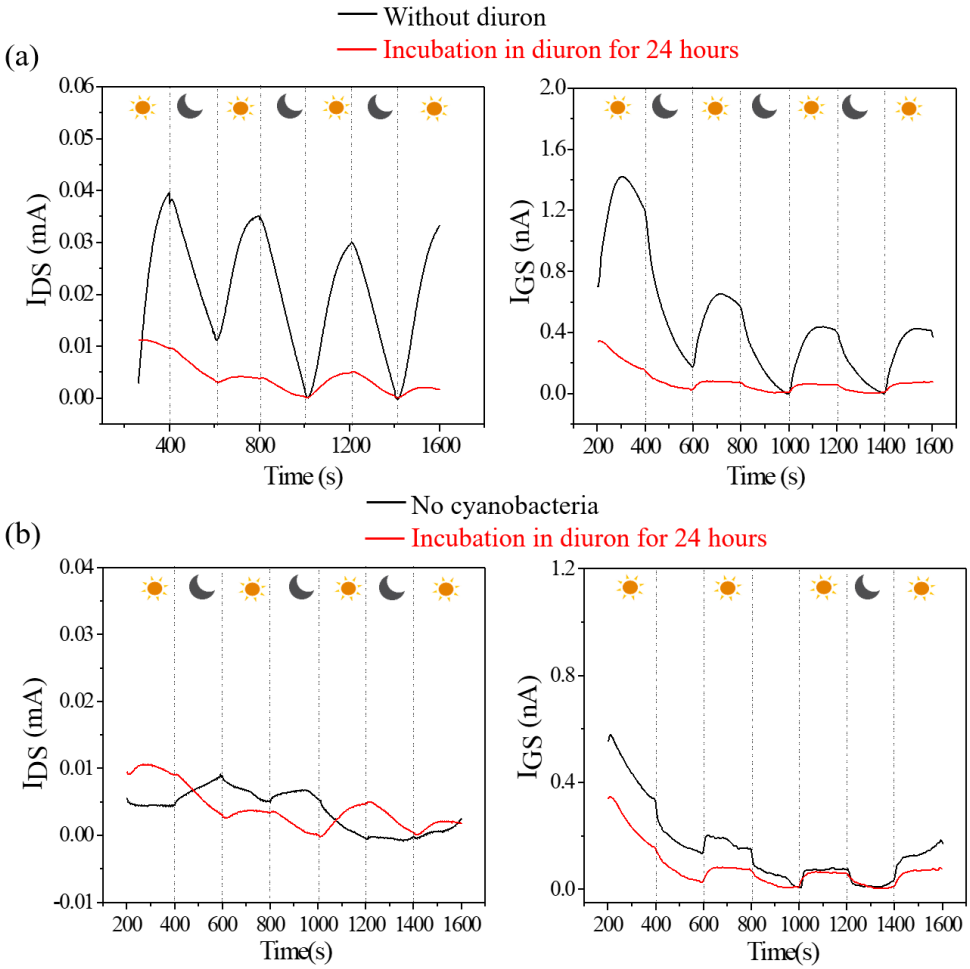

Figure 4.13: a) Drain current (left) and gate current (right) obtained in the algal hydrogel electrolyte before (black curve) and after (red curve) its incubation for 24 hours in 10 µM diuron solution. The results are compared with b) representing additional plot of hydrogel characterization without cyanobacteria ($V_{GS} = -1$ V, $V_{DS} = -0.9$ V, $t_{red} = 1$ s; raw data is presented in Appendix D.5 and Appendix D.6 for a) and b), respectively).

To verify this behavior, the current obtained in the polluted algal hydrogel was compared with the current obtained for the hydrogel without the algal presence (Figure 4.13 b.).

As it can be observed, the alternation of "day/night" cycles impacted in the same way both samples. A negligible photocurrent contribution is observed in both cases. These preliminary results evidence the possibility of qualitative herbicide tracking in the rGO EG-FET configuration.

4.5 Conclusions

In this chapter, we have seen the application of rGO EG-FET for life-cycle monitoring of photosynthetic organisms. The actual process occurring here is not only based on the capacitive effects occurring at the gate/electrolyte and the electrolyte/rGO interfaces. The faradic reaction due to oxygen reduction has to be taken into account when describing the mechanism related to the monitoring of the photosynthetic activities in EG-GFET configuration. As observed, photosynthetic activities were detected only in the case when the cyanobacteria were in contact with both the rGO channel and the gate electrode. This was the case with the rGO EG-FET configuration where the cyanobacteria were added into a liquid electrolyte and where the cyanobacteria hydrogel was used as a solid electrolyte. The oxygen reduction, expected to occur only at the platinum surface, was not detected upon cyanobacteria's immobilization at the gate electrode. The possibility of oxygen reduction at the rGO cannot be neglected. One should keep in mind that the defect-free graphene itself has not the possibility to catalyze the oxygen reduction, since it has no functional groups on its surface.[177;178] On the contrary, in modified graphene-based materials, the presence of foreign atoms that disturb the sp^2 carbon lattice can serve as catalytic centers for oxygen reduction.[179]

Nevertheless, further experimental work is needed to confirm the actual process. The deposition of cyanobacteria on solely the rGO channel of EG-FET is envisaged to be performed before my PhD defense, which could allow us to deduce the actual mechanism occurring here.

The preliminary results obtained for the pollutant's influence on the photosynthetic activities show the potential eligibility of the rGO EG-FET device for qualitative "pre-screening" of water samples using living organisms which mimic a real natural environment. The advantages of our device are the low working voltages which are compatible with biological samples, the use of small sample volumes (50-100 µL) and its high sensitivity. Moreover, the use of inkjet printing technology paves the way for low-cost, disposable and portable devices which could be used for easy in-field characterizations.

However, further experiments should be done with different pollutants and even pollutants cocktails such as atrazine, glyphosate and many others. Also, a complete study with various concentration is needed to define the detection limits of the device.

Conclusions and perspectives

Conclusions and perspectives

In this work, a formulation of an inkjet printable graphene oxide (GO) ink was presented. An *in-situ* approach for the electrochemical reduction of inkjet-printed GO film was developed, allowing us to obtain conductive reduced graphene oxide (rGO) in a practical way directly on the bottom-contact transistor's structure, without the use of harsh and toxic chemicals, and under ambient conditions. The electronic transport in rGO was tuned by using two different strategies: electrochemical control over the reduction state of rGO on the one hand, and doping from molecular adsorbates on the other hand. The electrochemical approach revealed a significant influence of the reduction degree on charge carrier's mobilities and the Dirac point position. Duration of the reduction process was found to be an important parameter, where with increased reduction time, the Dirac point position was found to shift toward less positive gate potentials, whereas the charge mobilities were found to pass through an optimum value before decreasing at longer reduction times. The shift of the Dirac point could be explained as the consequence of rGO dedoping during the reduction process since there is an effective removal of oxygen groups. Nevertheless, the reduction process could also induce some structural defects in the rGO's structure, which could act as scattering centers, leading to diminished values of charge mobilities. Thanks to the functionalization accessible structure of rGO we found out, from the molecular functionalization approach, that the rGO's doping level is sensitive to the presence of nitrogen-rich aromatic molecules, which were synthetized for this purpose. This is possibly due to the established charge transfer between the rGO and the molecular assemblies. In that view, the manipulation of rGO's electronic properties was achieved.

In the case of the rGO EG-FET used as a biosensor for the life-cycle monitoring of cyanobacteria, the device showed excellent sensitivity toward algae's oxygen production with an amplification factor of up to one million. In addition, our device was able to detect the decrease of cyanobacteria's photosynthetic activity when those are exposed to an herbicide (diruon), which is promising for further detection of water pollutants using our device.

As perspectives of this work, a fine-tuning of doping effects in rGO could be achieved through a deeper investigation of the combination of electrochemical reduction control and molecular functionalization strategies: on one hand the rGO's electronic properties

could be manipulated through control of the electrochemical reduction rate, and on the other hand, by using appropriate molecular species the doping effects could be additionally tuned.

Besides, the BTZ-C_n molecule could be engineered in a way to allow the direct application of the rGO EG-FET for the detection of biomolecules. In this case, the molecular assembly of BTZ-based molecules on rGO would have an attachment group for the direct adsorption of the desired bio-molecule. The presence of bio-molecules would modify the rGO's electrical properties through purely capacitive effects.

Regarding the rGO EG-FET configuration utilized for cyanobacteria's photosynthetic activity monitoring, further experimental work is needed for the precise determination of the interface where the electron transfer occurs. We could also formulate a printable hydrogel containing cyanobacteria for its deposition at the rGO surface, which could allow to have a very thin layer of cyanobacteria at the transistor's channel and facilitate further investigations. Also, the device could be probed with different pollutant cocktails for the determination of device sensitivity and detection limits.

Finally, we could use the inkjet printing technique to obtain all inkjet-printed devices, facilitating the biosensor's portability for potential in-field analysis.

Annexes

Appendix A

CVD graphene-based FET for biosensing purpose

Appendix A

CVD graphene-based FET for biosensing purpose

In this Appendix, I will present the research project I was involved in during the three months PhD internship spent at "Institut National de Recherche Scientifique, Centre Energie Materiaux Telecommunications" in Montreal, Canada. This project was conducted in the "Molecular and Device Physics laboratory" under the supervision of Professor Emanuele Orgiu. This was a collaborative project including the experts in genomic bacteriology and biology. The aim of the project was the fabrication of a back-gated graphene-based field-effect device serving as a biosensor for sepsis-related biomarkers. Here, the general aspects of the research context will be discussed along with the research strategy for the biosensor fabrication. Finally, some of the obtained results will be presented.

A.1 Research context

The idea here was to develop a biosensor that can detect a variety of biomarkers related to sepsis and meningitis. Sepsis is caused by the pathogen invasion into the blood stream[180]. One should note that sepsis itself is not a disease but the innate inflammatory response of the immune system to the presence of an infection in the body (e.g., bacterial presence).[181]

According to WHO, in 2017, there were 11 million deaths worldwide caused by sepsis, which was almost 20 % of worldwide deaths.[182] Bacteria *Neisseria meningitidis* is one of the very hazardous pathogens causing severe brain damage (such as learning disability, hearing loss) and it has the potential to cause epidemics.[183]

One of the most used methods for sepsis diagnosis, known as a gold standard, is positive blood culture.[a] The problem lies in the low sensitivity of these tests since a

[a]Blood culture represents a test verifying the presence of pathogens in blood. Positive blood culture diagnosis means infected blood.

negative blood culture is diagnosed in the majority of cases.[184] Also, important blood volumes are needed (≈10-30 mL) and the procedure can be time-consuming (2-10 days due to slow culture growing). Polymerase chain reaction (PCR)-based detection of pathogens is more sensitive and quicker compared to blood culture test, since it allows sepsis diagnosis within one working day.[185] However, the delivery of goal-oriented therapy could remarkably reduce the mortality rate if it were established within 6 hours, which explains why a development of reliable and rapid sensing tools is crucial.[186]

As WHO elaborated a project to defeat meningitis by 2030[187], the development of rapid and accurate detection of sepsis and meningitis-related biomarkers is necessary, which is also one of the main goals of this research project. Compared to conventional methods, our approach would allow to characterize very low sample volumes (1 µL).

Since the project began with my internship at INRS, the biosensor required to be fabricated and fully tested. As a preliminary step, we succeeded in detecting the target-receptor binding event by the end of the internship, which is discussed in the following subsection.

A.1.1 Development of the biosensor

Graphene's sensitivity to its electronic environment was used for sensing the presence of biomolecules. As discussed in Chapter 1, a charged molecule can act as a local gate and induce the accumulation of holes or electrons in the case of a negatively or positively charged molecule, respectively (see Figure 1.29). This mechanism allows to obtain a good sensing platform using graphene as the active channel in the GFET structure.

Commercially available CVD monolayer graphene (theoretical thickness of 0.345 nm) deposited onto Si/SiO_2 (1 cm×1 cm, oxide thickness 90 nm) was used as a substrate for GFET fabrication.

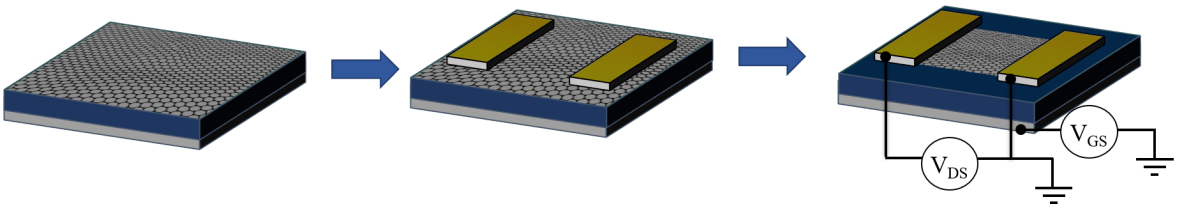

Figure A.1: Fabrication steps of GFET starting from large area CVD graphene on Si/SiO_2 (left), source/drain deposition (middle) and graphene etching (right) leading to final back-gated GFET device.

This large-area graphene required channel patterning, where channel dimensions (4 mm×3.5 mm) were chosen to fit the geometry of already available aluminum shadow masks for electrode deposition. The graphene layer patterning was performed using oxygen plasma. This method is largely used for graphene patterning.[188;189] Fabrication

steps are schematically represented in Figure A.1. As it can be observed, the deposition of electrode contacts (source/drain electrodes made of Ti/Au) was performed before graphene etching. Subsequently, the CVD graphene layer was covered with a mechanical mask, protecting the channel surface during the oxygen plasma etching. Figure A.2 depicts the protected and etched area on SiO_2 substrate.

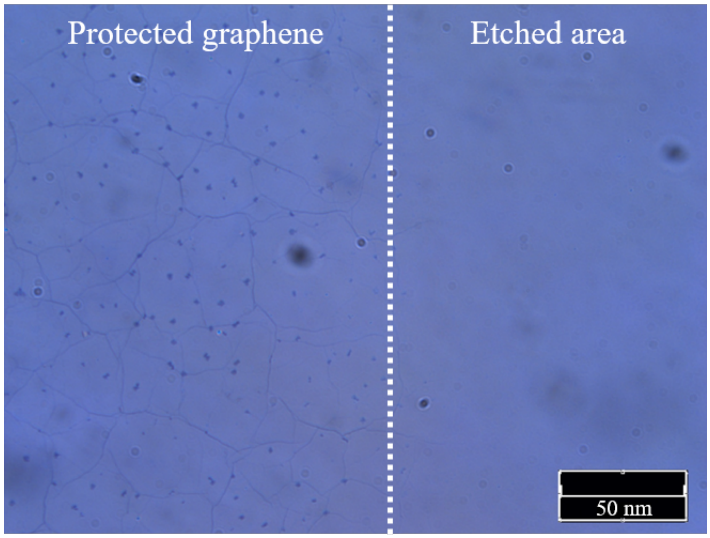

Figure A.2: SiO_2 substrate bearing protected non-etched graphene and etched area, characterized by optical microscopy. Dark lines visible on the non-etched area represent the presence of wrinkles.

A proper etching was found to be a crucial step for good working performances of GFETs, avoiding significant gate leakage currents.

For the receptor/target couple, the receptor molecule chosen here was an antibody from the IgG family (the most represented antibody in the human body, also known to protect humans from infections through binding of pathogens) under the name of Infliximab. This antibody is known to bind with TNF-α protein which was used as a target molecule. TNF-α has a role in the immune system regulation by creating inflammations.

As a transducer of bio-detection, graphene was covered with a supramolecular assembly of a novel molecule: 3-trifluoromethyl-3-(3-octadecyloxyphenyl) named as DZM in further text. DZM is composed of light-reactive diazirine head and aliphatic chain tail, as represented in Figure A.3 a. In the presence of UV light (λ= 365 nm), a diazirine group is activated into a reactive carbene, which allows the covalent attachment of an antibody. The versatility of this approach lies in the fact that the activated diazirine can accommodate any kind of receptor. The long aliphatic chain helps to establish a self-assembled molecular layer on graphene through VdW interactions.

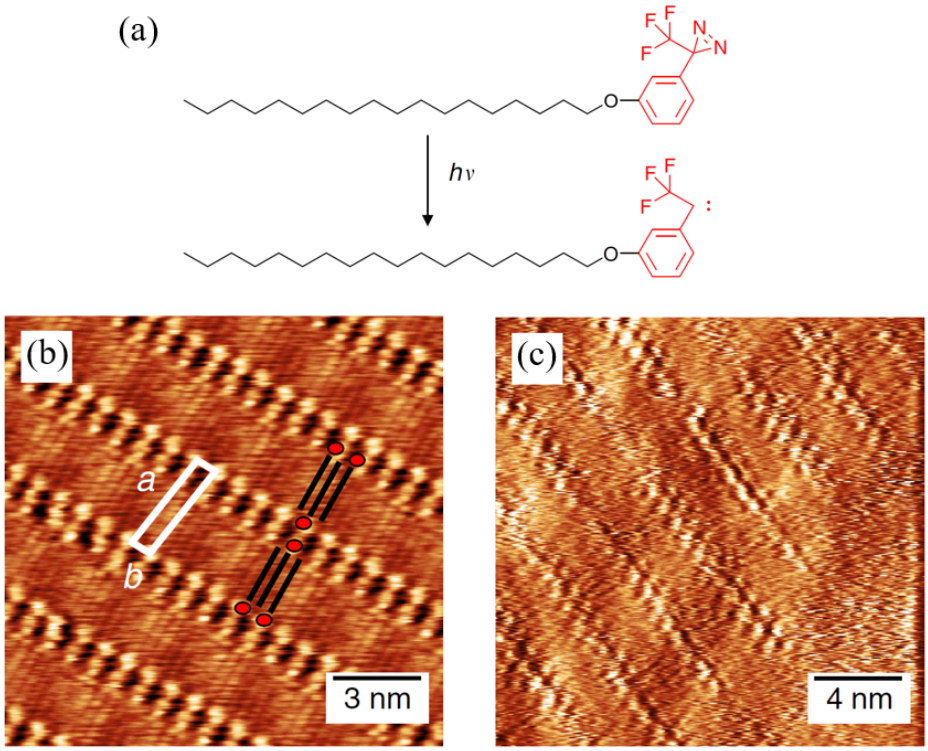

Figure A.3: a) Chemical structure of DZM molecule and the activation of diazirine group through UV irradiation; STM characterizations of DZM self-assemblies spin-coated from chloroform (1 mg mL^{-1}) on b) HOPG and c) CVD graphene.[190]

Orgiu and co-workers already studied the DZM self-assembling behavior on the HOPG and CVD graphene supported by SiO_2.[190] As shown in Figure A.3 (b. and c.), STM characterizations revealed the formation of well-ordered supramolecular assemblies observed on both substrates.

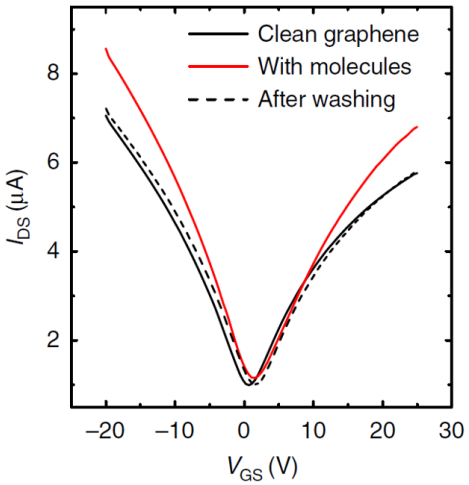

Figure A.4: Electrical characterizations in GFET configuration of CVD graphene supported by SiO_2 (black solid line), graphene functionalized with DZM (red) and GFET rinsed with chloroform (black-dotted line). The DZM was spin-coated from chloroform solution (1 mg mL^{-1}). The thickness of SiO_2 was 90 nm and the applied V_{DS} was 10 mV.[190]

Besides, they reported negligible doping effects on graphene caused by DZM presence since no significant shift of Dirac point was observed upon the electrical characterization of graphene functionalized with DZM (Figure A.4).

A.2 GFET electrical characterization

As mentioned in Chapter 1, in the back-gated configuration due to the important thickness of the solid dielectric, one should apply higher gate voltages compared to EG-GFET configuration to achieve an efficient graphene polarization.

Figure A.5 shows the output and corresponding transfer curves obtained in the fabricated GFET configuration. The output characteristics (Figure A.5, left) showed a solely linear regime, which is typical for graphene-based materials. Besides, the slope of the output characteristics varied with the applied gate voltage, evidencing an effective field-effect in the GFET device. The obtained transfer characteristic (Figure A.5, right) showed just one branch of the expected V-shaped curve, usually found for the ambipolar behavior of graphene. Although the gate voltage was swept from -40 to 80 V, a Dirac point was not observed. One should note that further widening of the gate potential window resulted in damaged devices, possibly due to dielectric breakdown. The obtained gate current (not shown here) stayed four orders of magnitude lower, confirming proper device fabrication with no leakage current.

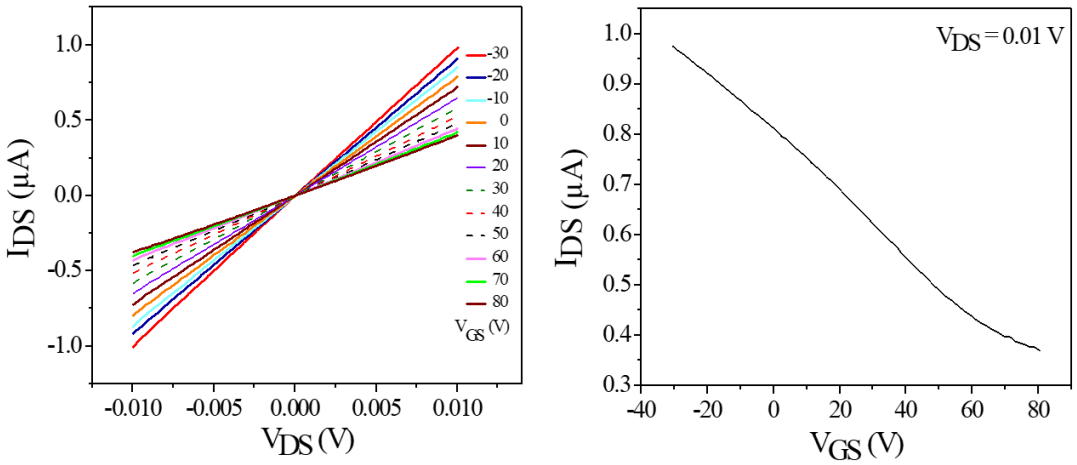

Figure A.5: Output (left) and transfer (right) characteristics of CVD graphene layer supported by SiO_2 in GFET configuration. The measurement is performed in dry conditions.

The Dirac point position observed to be far from the studied gate potential window (and toward more positive V_{GS}), indicated the presence of remarkable initial p-doping effects in graphene. We suppose that this may be due to the presence of impurities or residual PMMA, often used as supporting layer for CVD graphene transfer onto

Si/SiO_2 for the fabrication of commercial samples, since this behavior is observed for all fabricated devices.

Nevertheless, the device was applied for the detection of TNF-α protein's binding to the antibody from IgG family, which is presented in the following section.

A.2.1 Bio-detection experiments

Prior to bio-detection monitoring, the transfer curve acquisition was performed for several steps, as shown in Figure A.6 (left).

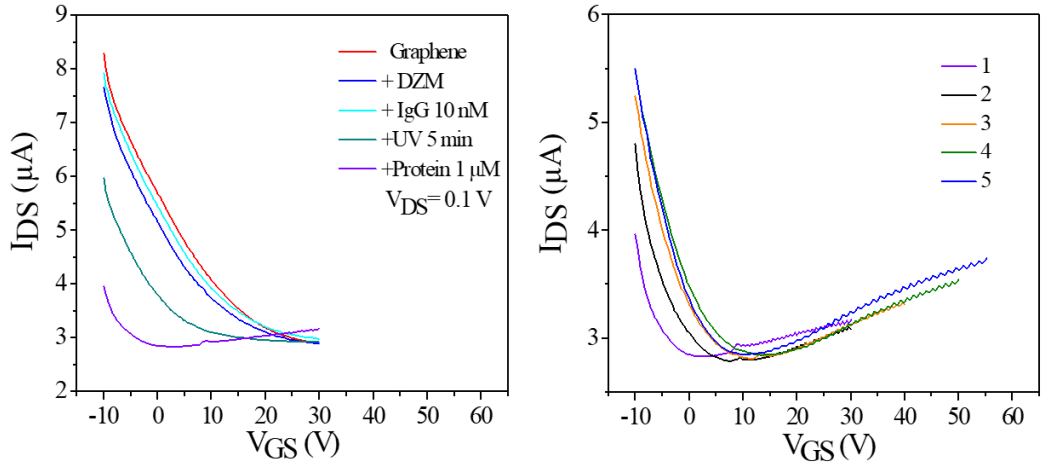

Figure A.6: Left: Transfer curves representing drain current variations with each step indicated in legend. Right: Transfer curve stabilization obtained upon the TNF-α protein addition. Transfer curve indicated as No.1 is the last transfer curve named as "+protein 1 µM" in left Figure.

The CVD graphene was characterized before and after the formation of the molecular carpet (+DZM), upon UV activation promoting the covalent attachment of antibodies (IgG) and finally, upon the addition of TNF-α protein as a target molecule. As it can be noticed, each step resulted in a current change, evidencing a high sensitivity of graphene. The attachment of TNF-α protein resulted in a drastic change of transfer characteristic. Therefore, the transfer curve's right branch appeared with the protein addition, suggesting an ambipolar behavior which was not observed before. For the sake of clarity, in Figure A.6 (right) are shown only the transfer curves obtained upon the protein addition. Current stabilization is observed upon consecutive transfer curve acquisitions. The protein's presence induced the change of graphene's electronic properties, resulting in a clear observation of the Dirac point. We suppose that proteins caused the accumulation of negative charge, resulting in a "shift" of the Dirac point position toward less positive potentials.

In another experiment, the I-V characteristics were compared after antibody-protein coupling, without rinsing and then after rinsing. Figure A.7 (left) shows the transfer

curve obtained upon the protein addition on previously functionalized graphene and the transfer curve obtained subsequently after rinsing the device with distilled water (Figure A.7, right). Device rinsing with distilled water is supposed to remove the proteins due to their solubility in water. Moreover, the protein/antibody interaction is weaker compared to antibody/molecule interaction (covalent interaction). As it can be noticed, protein removal resulted in a loss of the transfer curve's right branch, indicating the previously observed p-doping effects initially present in CVD graphene samples. At the same time, this experiment showed the evidence of protein's significant influence on graphene's electronic properties.

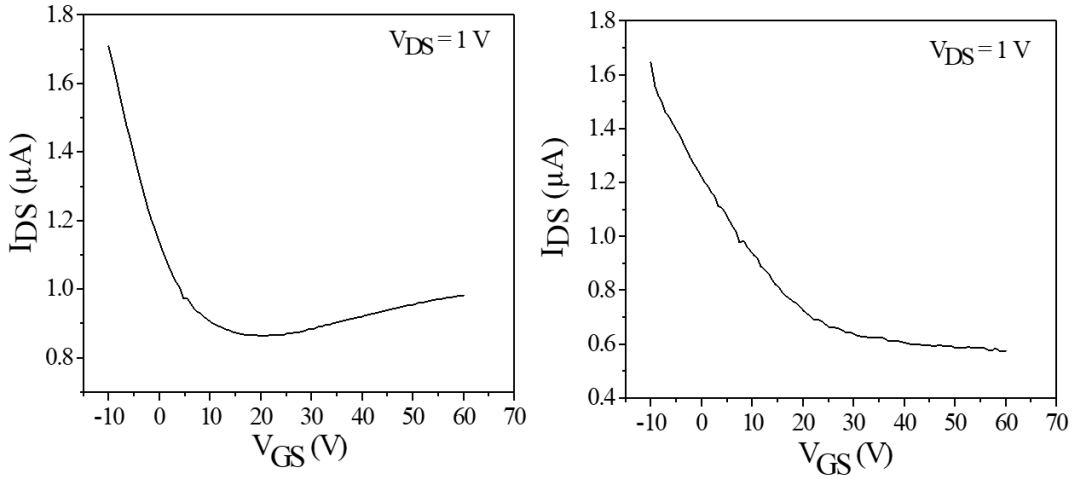

Figure A.7: Left: Transfer curves representing the last step of biodetection: protein addition (10 μM). Right: Transfer curve obtained upon rinsing the device with distilled water.

Besides, the fact that the target/receptor/DZM can be rinsed away altogether by removing the molecular carpet, soluble in chloroform, is the advantage of our device since the graphene layer can be reused.

Nevertheless, further experiments will be needed to discard the initial p-doping effects present in graphene samples. This will make it easier to measure the bio-event influence by following the variations of the Dirac point position. Besides, the device should be tested using IgG family antibodies toward several biomarkers associated with sepsis, such as C-reactive protein, Lipocalin 2 and CD64.

As a perspective, the development of a platform for the simultaneous analysis of different biomarkers at the same time is envisaged. The covalent attachment of different receptor molecules through UV activation of the diazirine group could be achieved, where each receptor will bind with different specific biomarkers. The versatility of the approach presented in this project allows not only to detect the biomarkers related to sepsis but also other disease-related biomarkers.

A.3 Experimental

Evaporation of metallic source/drain contacts (Ti/Au: 5 nm /50 nm) was performed using AXXIS e-beam evaporator (purchased at Kurt J. Lesker company). The mechanical mask used to protect the graphene's surface during plasma etching was made of Inconel (nickel-chromium alloy). The etching was performed using the Fluorescent ICP graver by Oxford Instruments. The adjusted parameters applied for strike power: 600 W, RF: 20 W at 10 mTorr for 3 s; and for inductively coupled plasma (ICP): 500 W, RF: 10 at 4 mTorr for 30 s. The electrical characterizations of fabricated GFET device (represented in Figure A.8) were performed using a Keithley 2636B.

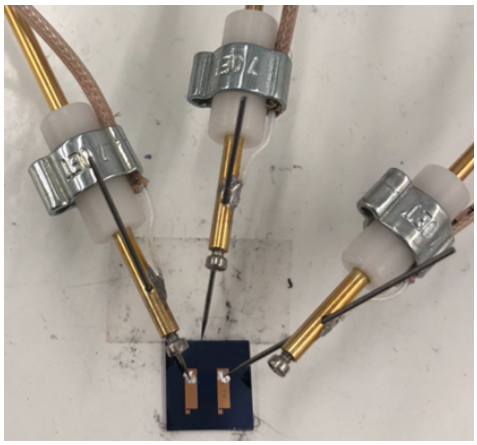

Figure A.8: Representation of fabricated GFET back-gated device along with the configuration for electrical characterizations.

The gate was contacted directly from the substrate's back-side (Si side) or using a silver paste to facilitate the contact.

The molecular functionalization of graphene was performed by spin-coating 40 µL of 1 mg mL^{-1} DZM (dissolved in chloroform) onto the whole substrate (spin coating speed: 4000 rpm; acceleration: 4000 rpm s^{-1}; duration: 30 s). The IgG antibodies solutions were prepared from Remicade Infliximab lyophilized powder, which was reconstituted in sterile water to a stock solution of 10 mg mL^{-1}. The Infliximab powder contained 50 mg of sucrose, 0.05 mg of polysorbate 80, 0.22 mg of monobasic sodium phosphate monohydrate, and 0.61 mg of dibasic sodium phosphate dyhydrate, which needed to be filtered. After filtration and centrifugation, the final concentration was measured by UV-Visible spectroscopy using Cytation 5 imaging reader with a wavelength of 280 nm. The stock solution of antibodies (59.181 µM) was further diluted in sterile water for experimental work.

TNF α protein was purchased at Acro biosystems in the form of lyophilized powder (Molecular weight: 18.2 kDa). Both buffer solutions (pH=7.4) and protein solutions kept just in sterile water were used. No important differences were observed in terms of electrical characterizations.

Appendix B

Inkjet printing technique

Appendix B

Inkjet printing technique

Some of the main components of the inkjet printer used in this work are the print carriage, cleaning station, platen and drop watcher.

- *The platen* is directly connected to the vacuum system, which permits holding the sample fixed to the platen surface avoiding its movement during the printing process. To promote the solvent evaporation, the platen can be heated (up to $60°C$). Thanks to the platen, a substrate can be aligned according to the printing needs.

- *The print carriage* (Figure B.1) is another mobile part of the printer. It contains the cartridge fixed to the cartridge holder. Before any printing process, it is essential to indicate the approximate thickness of the sample. According to that, the height of the print carriage will be automatically adjusted. The fiducial camera, a part of the print carriage, permits having an insight into the printed feature as well as to define the starting printing point of one pattern.

- *The drop watcher* system following in real time the jetting nozzles. Jetting speed can be adjusted and the nozzles behavior directly observed. Clogged nozzles are one of the main problems during the inkjet printing process. Having a real-time insight on the jetting nozzles functionality is essential, thus avoiding the use of the clogged nozzles and performing a cleaning process when needed.

- *The cleaning station* serves to clean the nozzles before, during and after the inkjet printing process. Different cleaning modes are available:

  - *Blotting* where the nozzles come in close contact with the cleaning pad, allowing the removal of an excess of ink out of the nozzle's surface.

  - *Spitting* permits cleaning the nozzles by ejecting the ink out of all the nozzles at the same time.

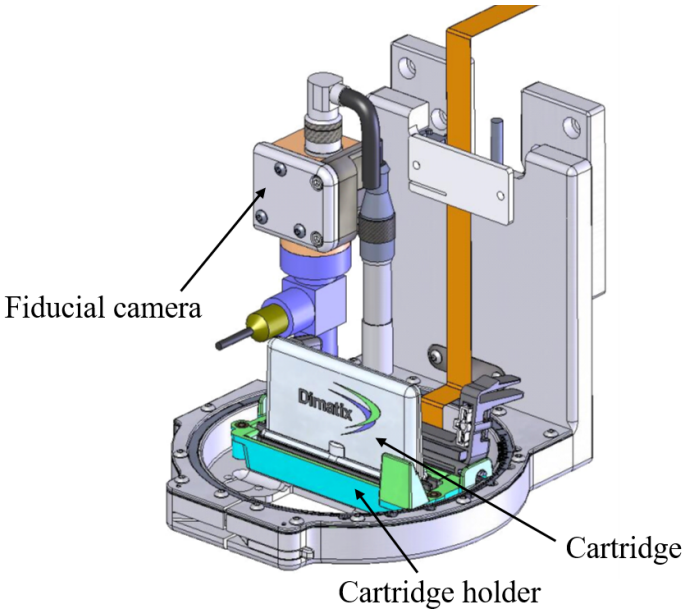

Figure B.1: Print carriage with arrows representing its main parts.[124]

– *Purging* consists in applying pressurized air on the nozzles, thus helping to clean hardly clogged nozzles.

The user can actually define his/her own sequence by combining the three modes and setting the duration of each phase.

For the elaboration of GO printed layers, the combination of spit-purge-spit cleaning modes was performed. The distance between the printer head and the substrate was kept at 500 µm. To promote the solvent evaporation, the substrate was heated at 40 °C. One printing nozzle was used in the printing process.

Appendix C

Additional data for Chapter 3

Appendix C

Additional data for Chapter 3

C.1 Electrochemical reduction of GO in a three-electrode cell

The study of GO reduction in a conventional 3-electrode electrochemical setup using a gold macroscopic working electrode is shown in Figure C.1. The data obtained here is comparable with data obtained on the macroscopic glassy carbon electrode described in the main text (Figure 3.3).

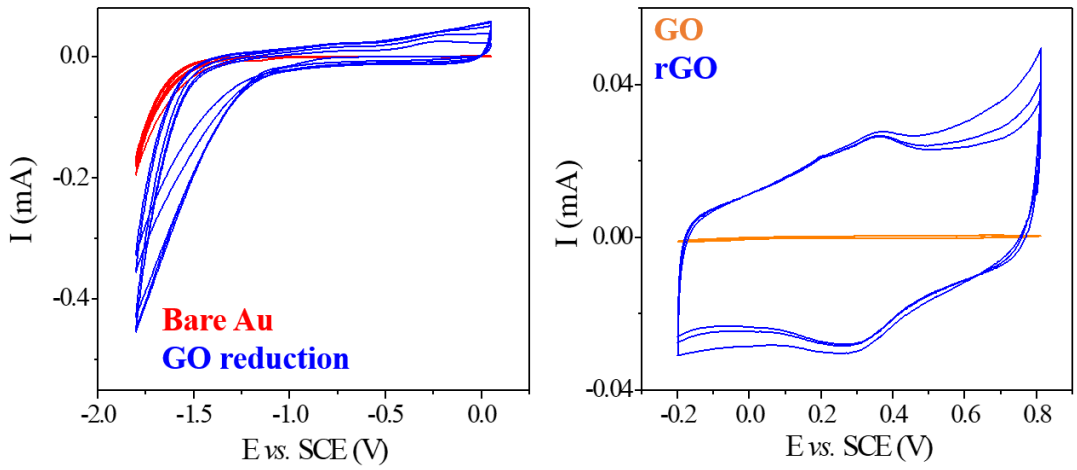

Figure C.1: Left: Cyclic voltammograms of bare Au macroscopic electrode (red) and GO reduction (blue) performed in PBS, scan rate 50 mV s^{-1}. Right: Electrochemical characterization in 1 M H_2SO_4 of GO before (orange) and after (blue) reduction on Au.

C.2 Electrical characterizations of rGO EG-FET device

C.2.1 Stability of rGO EG-FET device

The stability of rGO EG-FET device was verified by consecutive acquisitions of transfer curves on the same rGO layer represented in Figure C.2.

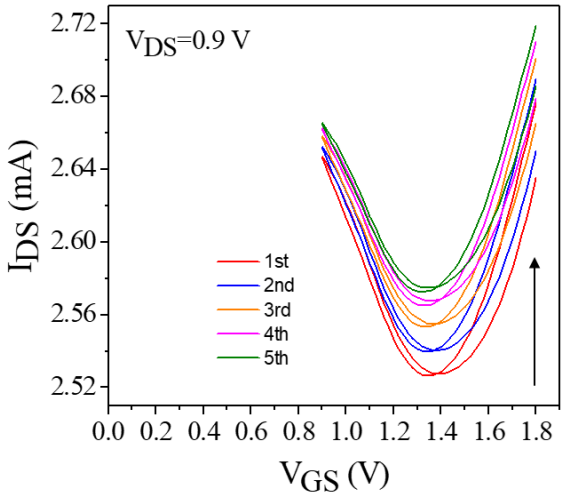

Figure C.2: Consecutive transfer curves recorded over the same printed rGO sample obtained after 5 s of reduction duration (t_{red} = 5 s).

The Dirac point position was observed to be stable and does not change during the electrical measurements. The current was observed to stabilize upon the transfer curve acquisition. Besides, the rGO's morphology was verified by optical microscopy before and after the electrical measurements. No degradations were observed.

C.2.2 Reduction degree influence: additional data

Additional data for another inkjet printed sample on which the reduction degree influence was studied is shown in Figure C.3. The shift of the Dirac point and the slope damping are observed to change upon the variation of reduction duration.

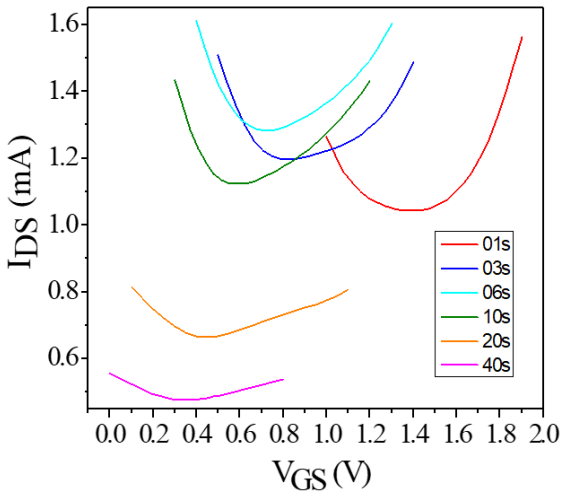

Figure C.3: Transfer characteristics of inkjet printed rGO layer upon progressive electrochemical reduction. Reduction time is indicated in the legend.

C.3 AFM characterizations on HOPG

The AFM images of molecular BTZ-C_6 deposition from the gas phase onto the HOPG are shown in Figure C.3. The characterization is performed by the acquisition of both topography and related phase AFM images.

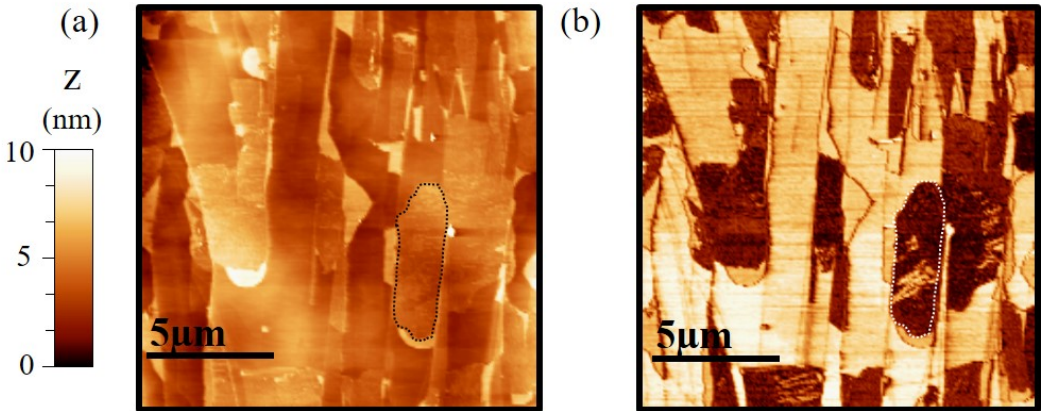

Figure C.4: AFM topography (a) and phase (b) characterization of BTZ-C_6 molecule deposited from the gas phase on HOPG. For the sake of clarity, the molecular presence is highlighted in the images with a black and white dashed lines for topography and phase characterizations, respectively.

In fact, the topographical characterization itself does not permit to clearly discern the difference between the substrate and the molecular adsorbates. On the other hand, the associated phase image enables us to determine the molecule's presence through contrast, reflecting the sample's composition. The bright contrast on

the phase characterization is attributed to HOPG, while the darker contrast is attributed to BTZ-C_6. As it can be observed, the molecular domains are ordered onto the HOPG without molecular islands.

C.4 Statistical study of molecular functionalization influence on the rGO's electrical properties

The data used for the statistical study of BTZ-C_n influence on the rGO (Figure 3.16, main text) is shown in Table C.1 and Table C.2.

Transistor 1					
Current (mA)					
bare rGO	1	2	3	4	5
	1.838	1.849	1.861	1.866	1.872
+1-propanol	1.916	1.918	1.921	1.924	-
+BTZ-C_6	1.940	1.944	1.945	1.943	1.939
Dirac point position (V)					
bare rGO	1	2	3	4	5
	1.990	2.010	2.020	2.020	2.020
+1-propanol	1.850	1.890	1.900	1.921	-
+BTZ-C_6	1.790	1.810	1.830	1.850	1.850

Table C.1: Current and Dirac point position values for Transistor 1.

Transistor 2					
Current (mA)					
bare rGO	1	2	3	4	5
	1.827	1.837	1.844	1.848	1.851
+1-propanol	1.855	1.855	1.863	1.867	1.871
+BTZ-C_6	1.842	1.850	1.833	1.844	1.849
Dirac point position (V)					
bare rGO	1	2	3	4	5
	1.770	1.810	1.830	1.830	1.830
+1-propanol	1.730	1.750	1.770	1.770	1.790
+BTZ-C_6	1.730	1.730	1.730	1.751	1.750

Table C.2: Current and Dirac point position values for Transistor 2.

Appendix D

Additional data for Chapter 4

Appendix D

Additional data for Chapter 4

Data used for the statistical study represented in Figure 3.16 of the main text is contained by Table D.1 and Table D.1.

V_{GS} (V)	I_{GS}(nA)	E_G *vs* Ag/AgCl (V)	I_{DS}(mA)
−0.5	118.1594	−0.1150	1.2210
−0.6	88.6335	−0.2170	1.2191
−0.7	59.8242	−0.3180	1.2187
−0.8	9.8146	−0.4160	1.2188
−0.9	46.4345	−0.5160	1.2220
−1	82.0848	−0.6140	1.2279
−1.1	125.9065	−0.7150	1.2294
−1.2	169.6926	−0.8150	1.2299
−1.3	214.2448	−0.9160	1.2304
−1.4	258.7726	−1.0160	1.2311
−1.5	270.0904	−1.1160	1.2323
−1.6	335.0565	−1.2150	1.2383
−1.7	390.3965	−1.3080	1.2592

Table D.1: Additional data referred to the measure of the platinum electrode electrochemical potential *vs* Ag/AgCl reference electrode (represented in Figure 4.5).

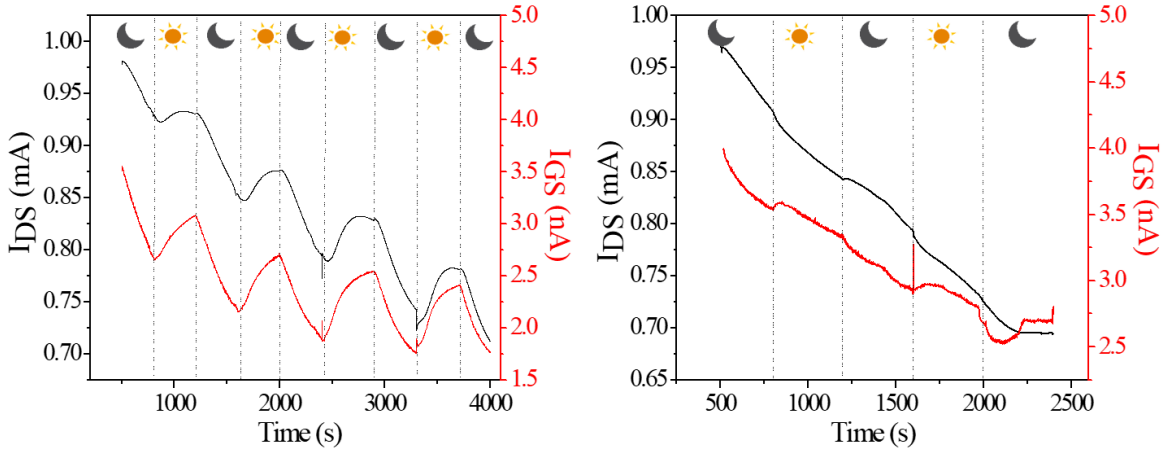

Figure D.1: Raw data corresponding to Figure 4.7 shown in the main text. The data recorded using cyanobacteria as electrolyte (left) and the culture medium B_{3N} without cyanobacteria (right).

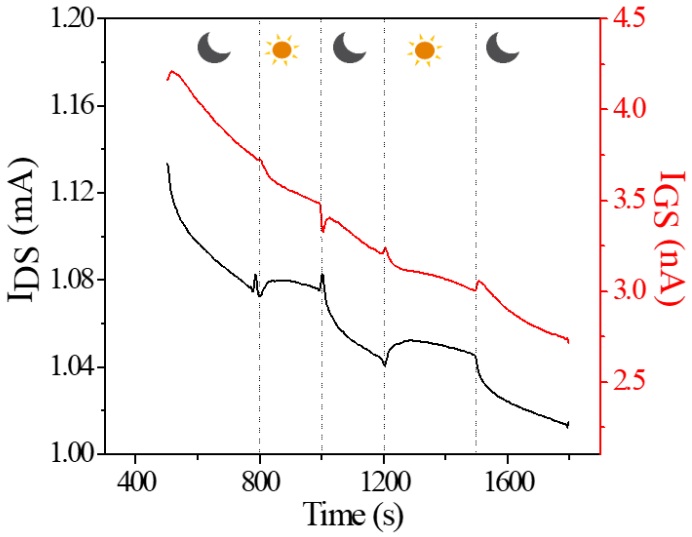

Figure D.2: Raw data corresponding to Figure 4.10 recorded upon gate functionalization with algal hydrogel.

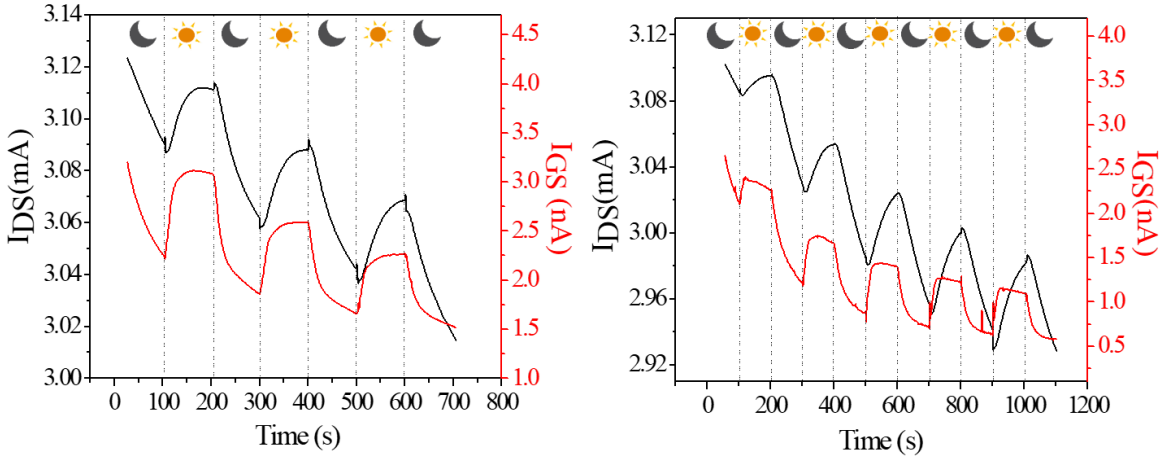

Figure D.3: Raw data corresponding to Figure 4.11 (b. and c.) recorded in cyanobacteria hydrogel using Pt (left) gate electrode (⌀= 100 µm) and Au (right) gate electrode (⌀= 250 µm).

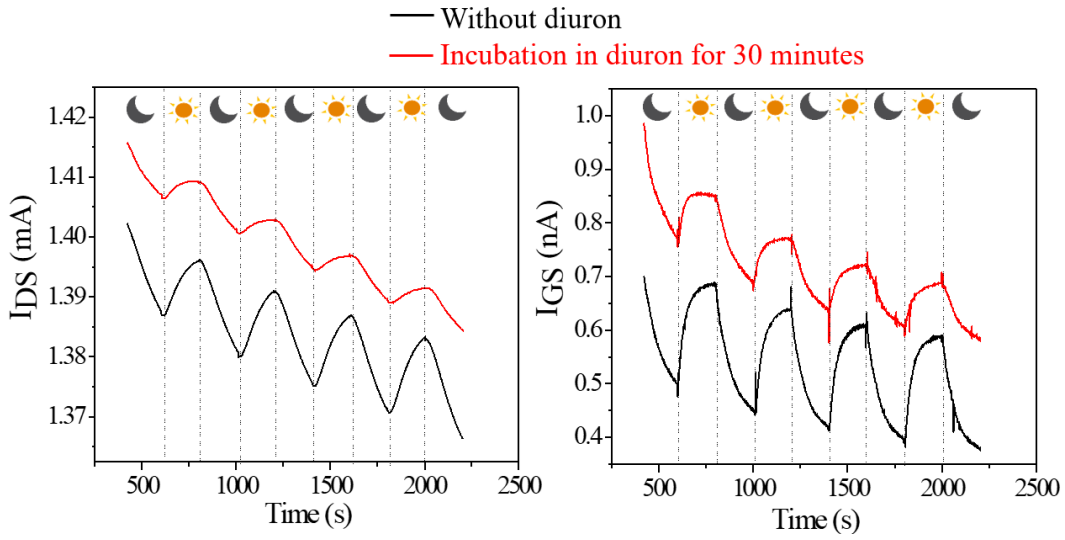

Figure D.4: Raw data corresponding to Figure 4.12. The data is obtained in the algal hydrogel before and after incubation for 30 minutes in 1 µM diuron solution (left: drain current; right: gate current).

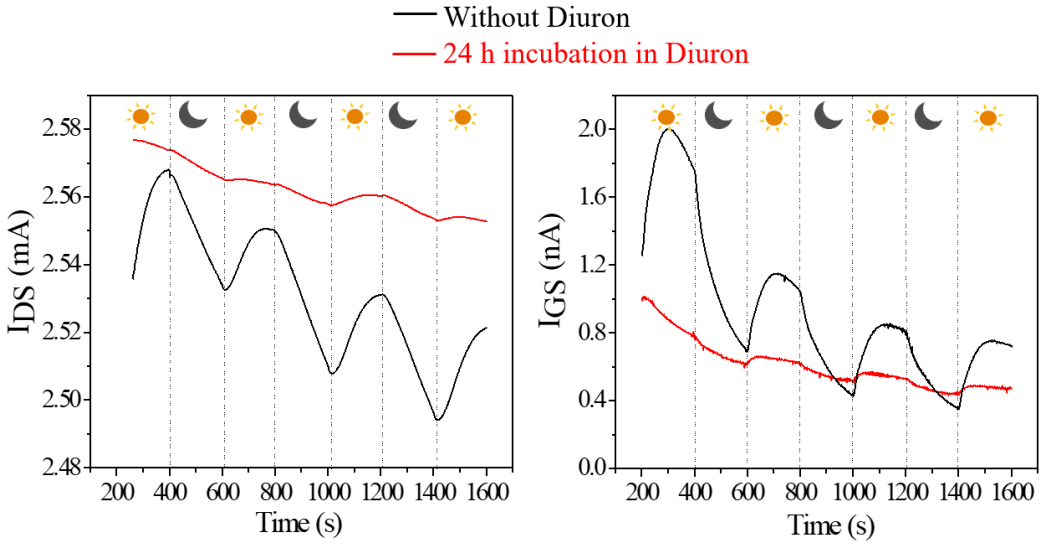

Figure D.5: Raw data corresponding to Figure 4.13 (a) obtained in the algal hydrogel electrolyte before and after 24 hours hydrogel incubation in 10 µM diuron solution (left: drain current; right: gate current).

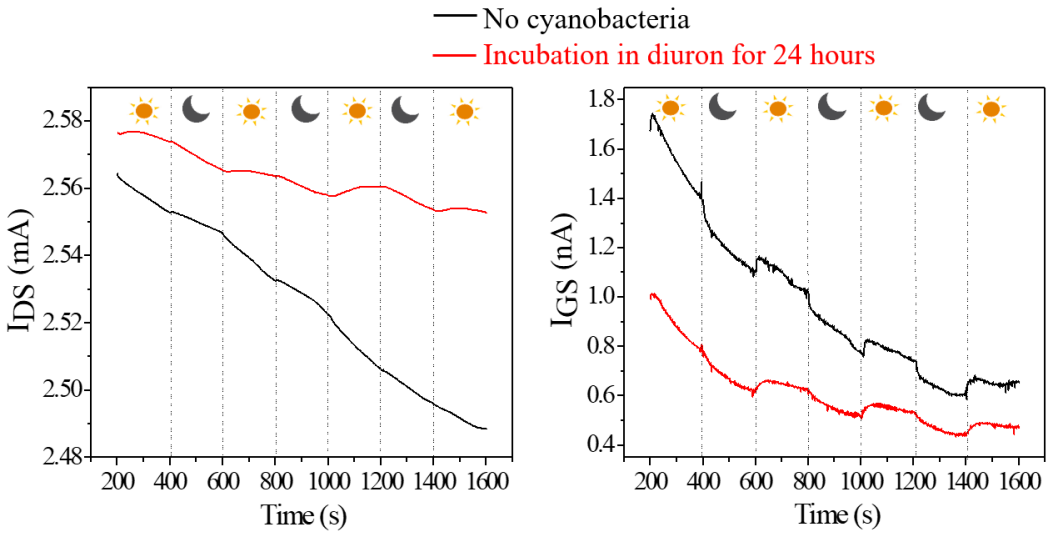

Figure D.6: Raw data corresponding to Figure 4.13 (b) obtained in the algal hydrogel incubated in 10 µM diuron for 24 hours (left: drain current; right: gate current).

Bibliography

Bibliography

[1] K. S. Novoselov. Electric Field Effect in Atomically Thin Carbon Films. *Science*, 306(5696):666–669, October 2004.

[2] Wonbong Choi, Indranil Lahiri, Raghunandan Seelaboyina, and Yong Soo Kang. Synthesis of graphene and its applications: a review. *Critical Reviews in Solid State and Materials Sciences*, 35(1):52–71, 2010.

[3] Qingqing Ke and John Wang. Graphene-based materials for supercapacitor electrodes–a review. *Journal of Materiomics*, 2(1):37–54, 2016.

[4] Haixin Chang and Hongkai Wu. Graphene-based nanomaterials: Synthesis, properties, and optical and optoelectronic applications. *Advanced Functional Materials*, 23(16):1984–1997, 2013.

[5] Rafael Furlan de Oliveira, Pietro Antonio Livio, Verónica Montes-García, Stefano Ippolito, Matilde Eredia, Pablo Fanjul-Bolado, María Begoña González García, Stefano Casalini, and Paolo Samorì. Liquid-gated transistors based on reduced graphene oxide for flexible and wearable electronics. *Advanced Functional Materials*, 29(46):1905375, 2019.

[6] H. P. Boehm, R. Setton, and E. Stumpp. Nomenclature and terminology of graphite intercalation compounds (IUPAC Recommendations 1994). *Pure and Applied Chemistry*, 66(9):1893–1901, January 1994.

[7] Christian Riedl. Epitaxial graphene on silicon carbide surfaces: growth, characterization, doping and hydrogen intercalation. *PhD thesis*, 2010.

[8] M Scarselli, P Castrucci, and M De Crescenzi. Electronic and optoelectronic nano-devices based on carbon nanotubes. *Journal of Physics: Condensed Matter*, 24(31):313202, August 2012.

[9] Y. Huang, J. Wu, and K. C. Hwang. Thickness of graphene and single-wall carbon nanotubes. *Physical Review B*, 74(24):245413, December 2006.

[10] Z. H. Ni, H. M. Wang, J. Kasim, H. M. Fan, T. Yu, Y. H. Wu, Y. P. Feng, and Z. X. Shen. Graphene Thickness Determination Using Reflection and Contrast Spectroscopy. *Nano Letters*, 7(9):2758–2763, September 2007.

[11] DDL Chung. Review graphite. *Journal of materials science*, 37(8):1475–1489, 2002. Publisher: Springer.

[12] Peter R. Buseck. Geological fullerenes: review and analysis. *Earth and Planetary Science Letters*, 203(3-4):781–792, November 2002.

[13] Neha Chauhan, Toru Maekawa, and Dasappan Nair Sakthi Kumar. Graphene based biosensors—accelerating medical diagnostics to new-dimensions. *Journal of Materials Research*, 32(15):2860–2882, 2017.

[14] H Cheun Lee, Wei-Wen Liu, Siang-Piao Chai, Abdul Rahman Mohamed, Chin Wei Lai, Cheng-Seong Khe, CH Voon, U Hashim, and NMS Hidayah. Synthesis of single-layer graphene: A review of recent development. *Procedia Chemistry*, 19:916–921, 2016.

[15] AM Abdelkader, AJ Cooper, RAW Dryfe, and IA Kinloch. How to get between the sheets: a review of recent works on the electrochemical exfoliation of graphene materials from bulk graphite. *Nanoscale*, 7(16):6944–6956, 2015.

[16] Josphat Phiri, Patrick Gane, and Thad C. Maloney. General overview of graphene: Production, properties and application in polymer composites. *Materials Science and Engineering: B*, 215:9–28, January 2017.

[17] Pei Yu, Sean E. Lowe, George P. Simon, and Yu Lin Zhong. Electrochemical exfoliation of graphite and production of functional graphene. *Current Opinion in Colloid & Interface Science*, 20(5-6):329–338, October 2015.

[18] Nazish Parveen, Mohd Omaish Ansari, and Moo Hwan Cho. Simple route for gram synthesis of less defective few layered graphene and its electrochemical performance. *RSC Advances*, 5(56):44920–44927, 2015.

[19] Khaled Parvez, Zhong-Shuai Wu, Rongjin Li, Xianjie Liu, Robert Graf, Xinliang Feng, and Klaus Mullen. Exfoliation of graphite into graphene in aqueous solutions of inorganic salts. *Journal of the American Chemical Society*, 136(16):6083–6091, 2014.

[20] Ching-Yuan Su, Ang-Yu Lu, Yanping Xu, Fu-Rong Chen, Andrei N. Khlobystov, and Lain-Jong Li. High-Quality Thin Graphene Films from Fast Electrochemical Exfoliation. *ACS Nano*, 5(3):2332–2339, March 2011.

[21] Rebecca S. Edwards and Karl S. Coleman. Graphene synthesis: relationship to applications. *Nanoscale*, 5(1):38–51, 2013.

[22] E. V. Rut'kov, A. V. Kuz'michev, and N. R. Gall'. Carbon interaction with rhodium surface: Adsorption, dissolution, segregation, growth of graphene layers. *Physics of the Solid State*, 53(5):1092–1098, May 2011.

[23] Silvan Roth, Jürg Osterwalder, and Thomas Greber. Synthesis of epitaxial graphene on rhodium from 3-pentanone. *Surface Science*, 605(9-10):L17–L19, May 2011.

[24] Cecilia Mattevi, Hokwon Kim, and Manish Chhowalla. A review of chemical vapour deposition of graphene on copper. *J. Mater. Chem.*, 21(10):3324–3334, 2011.

[25] Juha Riikonen, Wonjae Kim, Changfeng Li, Olli Svensk, Sanna Arpiainen, Markku Kainlauri, and Harri Lipsanen. Photo-thermal chemical vapor deposition of graphene on copper. *Carbon*, 62:43–50, 2013.

[26] Alfonso Reina, Stefan Thiele, Xiaoting Jia, Sreekar Bhaviripudi, Mildred S. Dresselhaus, Juergen A. Schaefer, and Jing Kong. Growth of large-area single- and Bi-layer graphene by controlled carbon precipitation on polycrystalline Ni surfaces. *Nano Research*, 2(6):509–516, June 2009.

[27] Ahmad Umair and Hassan Raza. Controlled synthesis of bilayer graphene on nickel. *Nanoscale Research Letters*, 7(1):437, December 2012.

[28] M. P. Lavin-Lopez, M. Fernandez-Diaz, L. Sanchez-Silva, J. L. Valverde, and A. Romero. Improving the growth of monolayer CVD-graphene over polycrystalline iron sheets. *New Journal of Chemistry*, 41(12):5066–5074, 2017.

[29] Yunzhou Xue, Bin Wu, Yunlong Guo, Liping Huang, Lang Jiang, Jianyi Chen, Dechao Geng, Yunqi Liu, Wenping Hu, and Gui Yu. Synthesis of large-area, few-layer graphene on iron foil by chemical vapor deposition. *Nano Research*, 4(12):1208–1214, December 2011.

[30] Giampiero Amato, Federico Beccaria, Elisabetta Landini, and Ettore Vittone. Raman analysis of strained graphene grown on dewetted cobalt. *Journal of Raman Spectroscopy*, 50(4):499–508, April 2019.

[31] Matteo Jugovac, Francesca Genuzio, Eduardo Gonzalez Lazo, Nataša Stojić, Giovanni Zamborlini, Vitaliy Feyer, Tevfik Onur Menteş, Andrea Locatelli, and Claus Michael Schneider. Role of carbon dissolution and recon-

densation in graphene epitaxial alignment on cobalt. *Carbon*, 152:489–496, November 2019.

[32] Zhen-Yu Juang, Chih-Yu Wu, Ang-Yu Lu, Ching-Yuan Su, Keh-Chyang Leou, Fu-Rong Chen, and Chuen-Horng Tsai. Graphene synthesis by chemical vapor deposition and transfer by a roll-to-roll process. *Carbon*, 48(11):3169–3174, September 2010.

[33] Roberto Muñoz and Cristina Gómez-Aleixandre. Review of CVD Synthesis of Graphene: Review of CVD Synthesis of Graphene. *Chemical Vapor Deposition*, 19(10-11-12):297–322, December 2013.

[34] Maria Losurdo, Maria Michela Giangregorio, Pio Capezzuto, and Giovanni Bruno. Graphene CVD growth on copper and nickel: role of hydrogen in kinetics and structure. *Physical Chemistry Chemical Physics*, 13(46):20836, 2011.

[35] Matthias Batzill. The surface science of graphene: Metal interfaces, CVD synthesis, nanoribbons, chemical modifications, and defects. *Surface Science Reports*, 67(3-4):83–115, March 2012.

[36] Guohui Zhang, Aleix G. Güell, Paul M. Kirkman, Robert A. Lazenby, Thomas S. Miller, and Patrick R. Unwin. Versatile Polymer-Free Graphene Transfer Method and Applications. *ACS Applied Materials & Interfaces*, 8(12):8008–8016, March 2016.

[37] Woong Sun Lim, Yi Yeon Kim, Hyeongkeun Kim, Sukjae Jang, Namyong Kwon, Beyoung Jae Park, Jong-Hyun Ahn, Ilsub Chung, Byung Hee Hong, and Geun Young Yeom. Atomic layer etching of graphene for full graphene device fabrication. *Carbon*, 50(2):429–435, February 2012.

[38] Haider Al-Mumen, Fubo Rao, Wen Li, and Lixin Dong. Singular Sheet Etching of Graphene with Oxygen Plasma. *Nano-Micro Letters*, 6(2):116–124, April 2014.

[39] Neeraj Mishra, John Boeckl, Nunzio Motta, and Francesca Iacopi. Graphene growth on silicon carbide: A review: Graphene growth on silicon carbide. *physica status solidi (a)*, 213(9):2277–2289, September 2016.

[40] Dandan Wang, Lei Liu, Wei Chen, Xiaobo Chen, Han Huang, Jun He, Yuan-Ping Feng, A. T. S. Wee, and D. Z. Shen. Optimized growth of graphene on SiC: from the dynamic flip mechanism. *Nanoscale*, 7(10):4522–4528, 2015.

[41] YQ Wu, PD Ye, Michael A Capano, Yi Xuan, Y Sui, Minghao Qi, James A Cooper, T Shen, D Pandey, G Prakash, et al. Top-gated graphene field-effect-transistors formed by decomposition of sic. *Applied Physics Letters*, 92(9):092102, 2008.

[42] H. Huang, S. Chen, A.T.S. Wee, and W. Chen. Epitaxial growth of graphene on silicon carbide (SiC). In *Graphene*, pages 3–26. Elsevier, 2014.

[43] George Bepete, Eric Anglaret, Luca Ortolani, Vittorio Morandi, Kai Huang, Alain Pénicaud, and Carlos Drummond. Surfactant-free single-layer graphene in water. *Nature Chemistry*, 9(4):347–352, April 2017.

[44] David W. Johnson, Ben P. Dobson, and Karl S. Coleman. A manufacturing perspective on graphene dispersions. *Current Opinion in Colloid & Interface Science*, 20(5-6):367–382, October 2015.

[45] Xiaolin Li, Guangyu Zhang, Xuedong Bai, Xiaoming Sun, Xinran Wang, Enge Wang, and Hongjie Dai. Highly conducting graphene sheets and langmuir–blodgett films. *Nature nanotechnology*, 3(9):538–542, 2008.

[46] Umar Khan, Arlene O'Neill, Mustafa Lotya, Sukanta De, and Jonathan N. Coleman. High-Concentration Solvent Exfoliation of Graphene. *Small*, 6(7):864–871, April 2010.

[47] Keith R. Paton, Eswaraiah Varrla, Claudia Backes, Ronan J. Smith, Umar Khan, Arlene O'Neill, Conor Boland, Mustafa Lotya, Oana M. Istrate, Paul King, Tom Higgins, Sebastian Barwich, Peter May, Pawel Puczkarski, Iftikhar Ahmed, Matthias Moebius, Henrik Pettersson, Edmund Long, João Coelho, Sean E. O'Brien, Eva K. McGuire, Beatriz Mendoza Sanchez, Georg S. Duesberg, Niall McEvoy, Timothy J. Pennycook, Clive Downing, Alison Crossley, Valeria Nicolosi, and Jonathan N. Coleman. Scalable production of large quantities of defect-free few-layer graphene by shear exfoliation in liquids. *Nature Materials*, 13(6):624–630, June 2014.

[48] Vasilios Georgakilas, Jitendra N. Tiwari, K. Christian Kemp, Jason A. Perman, Athanasios B. Bourlinos, Kwang S. Kim, and Radek Zboril. Noncovalent Functionalization of Graphene and Graphene Oxide for Energy Materials, Biosensing, Catalytic, and Biomedical Applications. *Chemical Reviews*, 116(9):5464–5519, May 2016. Publisher: American Chemical Society.

[49] Benjamin Collins Brodie. Xiii. on the atomic weight of graphite. *Philosophical Transactions of the Royal Society of London*, (149):249–259, 1859.

[50] Da Chen, Hongbin Feng, and Jinghong Li. Graphene Oxide: Preparation, Functionalization, and Electrochemical Applications. *Chemical Reviews*, 112(11):6027–6053, November 2012. Publisher: American Chemical Society.

[51] Heyong He, Jacek Klinowski, Michael Forster, and Anton Lerf. A new structural model for graphite oxide. *Chemical physics letters*, 287(1-2):53–56, 1998.

[52] Yanwu Zhu, Shanthi Murali, Weiwei Cai, Xuesong Li, Ji Won Suk, Jeffrey R Potts, and Rodney S Ruoff. Graphene and graphene oxide: synthesis, properties, and applications. *Advanced materials*, 22(35):3906–3924, 2010.

[53] L Staudenmaier. Verfahren zur darstellung der graphitsäure. *Berichte der deutschen chemischen Gesellschaft*, 31(2):1481–1487, 1898.

[54] William S. Hummers and Richard E. Offeman. Preparation of Graphitic Oxide. *Journal of the American Chemical Society*, 80(6):1339–1339, March 1958. Publisher: American Chemical Society.

[55] Daniela C. Marcano, Dmitry V. Kosynkin, Jacob M. Berlin, Alexander Sinitskii, Zhengzong Sun, Alexander Slesarev, Lawrence B. Alemany, Wei Lu, and James M. Tour. Improved Synthesis of Graphene Oxide. *ACS Nano*, 4(8):4806–4814, August 2010. Publisher: American Chemical Society.

[56] Maria del Prado Lavin-Lopez, Amaya Romero, Jesus Garrido, Luz Sanchez-Silva, and José Luis Valverde. Influence of Different Improved Hummers Method Modifications on the Characteristics of Graphite Oxide in Order to Make a More Easily Scalable Method. *Industrial & Engineering Chemistry Research*, 55(50):12836–12847, December 2016. Publisher: American Chemical Society.

[57] Andrea G Marrani, Robertino Zanoni, Ricardo Schrebler, and Enrique A Dalchiele. Toward graphene/silicon interface via controlled electrochemical reduction of graphene oxide. *The Journal of Physical Chemistry C*, 121(10):5675–5683, 2017.

[58] Yuyan Shao, Jun Wang, Mark Engelhard, Chongmin Wang, and Yuehe Lin. Facile and controllable electrochemical reduction of graphene oxide and its applications. *Journal of Materials Chemistry*, 20(4):743–748, 2010. Publisher: Royal Society of Chemistry.

[59] Songfeng Pei and Hui-Ming Cheng. The reduction of graphene oxide. *Carbon*, 50(9):3210–3228, August 2012.

[60] Yong Zhou, Qiaoliang Bao, Lena Ai Ling Tang, Yulin Zhong, and Kian Ping Loh. Hydrothermal dehydration for the "green" reduction of exfoliated graphene oxide to graphene and demonstration of tunable optical limiting properties. *Chemistry of Materials*, 21(13):2950–2956, 2009.

[61] Jinping Zhao, Songfeng Pei, Wencai Ren, Libo Gao, and Hui-Ming Cheng. Efficient preparation of large-area graphene oxide sheets for transparent conductive films. *ACS nano*, 4(9):5245–5252, 2010.

[62] Xingfa Gao, Joonkyung Jang, and Shigeru Nagase. Hydrazine and Thermal Reduction of Graphene Oxide: Reaction Mechanisms, Product Structures, and Reaction Design. *The Journal of Physical Chemistry C*, 114(2):832–842, January 2010. Publisher: American Chemical Society.

[63] Sungjin Park and Rodney S. Ruoff. Chemical methods for the production of graphenes. *Nature Nanotechnology*, 4(4):217–224, April 2009.

[64] Vincent C. Tung, Matthew J. Allen, Yang Yang, and Richard B. Kaner. High-throughput solution processing of large-scale graphene. *Nature Nanotechnology*, 4(1):25–29, January 2009.

[65] Scott Gilje, Song Han, Minsheng Wang, Kang L Wang, and Richard B Kaner. A chemical route to graphene for device applications. *Nano letters*, 7(11):3394–3398, 2007. Publisher: ACS Publications.

[66] María Jesús Fernández-Merino, L Guardia, JI Paredes, S Villar-Rodil, Pablo Solís-Fernández, Amelia Martínez-Alonso, and JMD Tascón. Vitamin c is an ideal substitute for hydrazine in the reduction of graphene oxide suspensions. *The Journal of Physical Chemistry C*, 114(14):6426–6432, 2010.

[67] Li Song, Fitri Khoerunnisa, Wei Gao, Weihong Dou, Takuya Hayashi, Katsumi Kaneko, Morinobu Endo, and Pulickel M. Ajayan. Effect of high-temperature thermal treatment on the structure and adsorption properties of reduced graphene oxide. *Carbon*, 52:608 – 612, 2013.

[68] Yang Qiu, Fei Guo, Robert Hurt, and Indrek Külaots. Explosive thermal reduction of graphene oxide-based materials: Mechanism and safety implications. *Carbon*, 72:215–223, June 2014.

[69] Shaw Yong Toh, Kee Shyuan Loh, Siti Kartom Kamarudin, and Wan Ramli Wan Daud. Graphene production via electrochemical reduction of graphene oxide: synthesis and characterisation. *Chemical Engineering Journal*, 251:422–434, 2014.

[70] Hui-Lin Guo, Xian-Fei Wang, Qing-Yun Qian, Feng-Bin Wang, and Xing-Hua Xia. A Green Approach to the Synthesis of Graphene Nanosheets. *ACS Nano*, 3(9):2653–2659, September 2009.

[71] Jeffrey M Mativetsky, Andrea Liscio, Emanuele Treossi, Emanuele Orgiu, Alberto Zanelli, Paolo Samorì, and Vincenzo Palermo. Graphene transistors via in situ voltage-induced reduction of graphene-oxide under ambient conditions. *Journal of the American Chemical Society*, 133(36):14320–14326, 2011.

[72] Jeffrey M Mativetsky, Emanuele Treossi, Emanuele Orgiu, Manuela Melucci, Giulio Paolo Veronese, Paolo Samori, and Vincenzo Palermo. Local current mapping and patterning of reduced graphene oxide. *Journal of the American Chemical Society*, 132(40):14130–14136, 2010.

[73] Austin C Faucett, Jaymes N Flournoy, Jeremy S Mehta, and Jeffrey M Mativetsky. Evolution, structure, and electrical performance of voltage-reduced graphene oxide. *FlatChem*, 1:42–51, 2017.

[74] N. D. Mermin. Crystalline Order in Two Dimensions. *Physical Review*, 176(1):250–254, December 1968.

[75] Mikhail I. Katsnelson. Graphene: carbon in two dimensions. *Materials Today*, 10(1-2):20–27, January 2007.

[76] Kostya S Novoselov, D Jiang, F Schedin, TJ Booth, VV Khotkevich, SV Morozov, and Andre K Geim. Two-dimensional atomic crystals. *Proceedings of the National Academy of Sciences*, 102(30):10451–10453, 2005.

[77] Changgu Lee, Xiaoding Wei, Jeffrey W Kysar, and James Hone. Measurement of the elastic properties and intrinsic strength of monolayer graphene. *science*, 321(5887):385–388, 2008.

[78] P. R. Wallace. The Band Theory of Graphite. *Physical Review*, 71(9):622–634, May 1947.

[79] A. H. Castro Neto, F. Guinea, N. M. R. Peres, K. S. Novoselov, and A. K. Geim. The electronic properties of graphene. *Reviews of Modern Physics*, 81(1):109–162, January 2009.

[80] G. W. Semenoff, V. Semenoff, and Fei Zhou. Domain Walls in Gapped Graphene. *Physical Review Letters*, 101(8):087204, August 2008.

[81] Brian J. Schultz, Robert V. Dennis, Vincent Lee, and Sarbajit Banerjee. An electronic structure perspective of graphene interfaces. *Nanoscale*, 6(7):3444, 2014.

[82] Michael Körner, Dominik Smith, Pavel Buividovich, Maksim Ulybyshev, and Lorenz von Smekal. Hybrid monte carlo study of monolayer graphene with partially screened coulomb interactions at finite spin density. *Physical Review B*, 96(19):195408, 2017.

[83] Daniel R. Cooper, Benjamin D'Anjou, Nageswara Ghattamaneni, Benjamin Harack, Michael Hilke, Alexandre Horth, Norberto Majlis, Mathieu Massicotte, Leron Vandsburger, Eric Whiteway, and Victor Yu. Experimental Review of Graphene. *ISRN Condensed Matter Physics*, 2012:1–56, 2012.

[84] Meihua Jin, Hae-Kyung Jeong, Woo Jong Yu, Dong Jae Bae, Bo Ram Kang, and Young Hee Lee. Graphene oxide thin film field effect transistors without reduction. *Journal of Physics D: Applied Physics*, 42(13):135109, July 2009.

[85] Ke-Yan Lian, Yong-Fei Ji, Xiao-Fei Li, Ming-Xing Jin, Da-Jun Ding, and Yi Luo. Big Bandgap in Highly Reduced Graphene Oxides. *The Journal of Physical Chemistry C*, 117(12):6049–6054, March 2013.

[86] Fei Zheng, Wei-Long Xu, Han-Dong Jin, Xiao-Tao Hao, and Kenneth P. Ghiggino. Charge transfer from poly(3-hexylthiophene) to graphene oxide and reduced graphene oxide. *RSC Advances*, 5(109):89515–89520, 2015.

[87] Brian J Schultz, Christopher J Patridge, Vincent Lee, Cherno Jaye, Patrick S Lysaght, Casey Smith, Joel Barnett, Daniel A Fischer, David Prendergast, and Sarbajit Banerjee. Imaging local electronic corrugations and doped regions in graphene. *Nature communications*, 2(1):1–8, 2011.

[88] Da Zhan, Jiaxu Yan, Linfei Lai, Zhenhua Ni, Lei Liu, and Zexiang Shen. Engineering the Electronic Structure of Graphene. *Advanced Materials*, 24(30):4055–4069, 2012.

[89] K. S. Novoselov, E. McCann, S. V. Morozov, V. I. Fal'ko, M. I. Katsnelson, U. Zeitler, D. Jiang, F. Schedin, and A. K. Geim. Unconventional quantum Hall effect and Berry's phase of 2 in bilayer graphene. *Nature Physics*, 2(3):177–180, March 2006.

[90] Yuanbo Zhang, Yan-Wen Tan, Horst L. Stormer, and Philip Kim. Experimental observation of the quantum Hall effect and Berry's phase in graphene. *Nature*, 438(7065):201–204, November 2005.

[91] K. S. Novoselov, A. K. Geim, S. V. Morozov, D. Jiang, M. I. Katsnelson, I. V. Grigorieva, S. V. Dubonos, and A. A. Firsov. Two-dimensional gas of massless Dirac fermions in graphene. *Nature*, 438(7065):197–200, November 2005.

[92] Konstantin S Novoselov and AK Geim. The rise of graphene. *Nat. Mater*, 6(3):183–191, 2007.

[93] Wangyang Fu, Lin Jiang, Erik P van Geest, Lia MC Lima, and Grégory F Schneider. Sensing at the surface of graphene field-effect transistors. *Advanced Materials*, 29(6):1603610, 2017.

[94] Max C Lemme, Tim J Echtermeyer, Matthias Baus, and Heinrich Kurz. A graphene field-effect device. *IEEE Electron Device Letters*, 28(4):282–284, 2007.

[95] Fengnian Xia, Damon B Farmer, Yu-ming Lin, and Phaedon Avouris. Graphene field-effect transistors with high on/off current ratio and large transport band gap at room temperature. *Nano letters*, 10(2):715–718, 2010.

[96] Seyoung Kim, Junghyo Nah, Insun Jo, Davood Shahrjerdi, Luigi Colombo, Zhen Yao, Emanuel Tutuc, and Sanjay K Banerjee. Realization of a high mobility dual-gated graphene field-effect transistor with al 2 o 3 dielectric. *Applied Physics Letters*, 94(6):062107, 2009.

[97] B Huard, JA Sulpizio, N Stander, K Todd, B Yang, and D Goldhaber-Gordon. Transport measurements across a tunable potential barrier in graphene. *Physical review letters*, 98(23):236803, 2007.

[98] Kosuke Nagashio. Graphene field-effect transistor application-electric band structure of graphene in transistor structure extracted from quantum capacitance. *Journal of Materials Research*, 32(1):64–72, 2017.

[99] Dmitry Kireev, Max Brambach, Silke Seyock, Vanessa Maybeck, Wangyang Fu, Bernhard Wolfrum, and Andreas Offenhäusser. Graphene transistors for interfacing with cells: towards a deeper understanding of liquid gating and sensitivity. *Scientific reports*, 7(1):1–12, 2017.

[100] Anindya Das, Simone Pisana, Biswanath Chakraborty, Stefano Piscanec, Srijan K Saha, Umesh V Waghmare, Konstantin S Novoselov, Hulikal R Krishnamurthy, Andre K Geim, Andrea C Ferrari, et al. Monitoring dopants by raman scattering in an electrochemically top-gated graphene transistor. *Nature nanotechnology*, 3(4):210–215, 2008.

[101] Hua Zhong, Zhiyong Zhang, Haitao Xu, Chenguang Qiu, and Lian-Mao Peng. Comparison of mobility extraction methods based on field-effect measurements for graphene. *Aip Advances*, 5(5):057136, 2015.

[102] Ciril Reiner-Rozman, Melanie Larisika, Christoph Nowak, and Wolfgang Knoll. Graphene-based liquid-gated field effect transistor for biosensing: Theory and experiments. *Biosensors and Bioelectronics*, 70:21–27, 2015.

[103] James Deane Patterson and Bernard C Bailey. *Solid-state physics: introduction to the theory*. Springer Science & Business Media, 2007.

[104] Kunal S Mali, John Greenwood, Jinne Adisoejoso, Roald Phillipson, and Steven De Feyter. Nanostructuring graphene for controlled and reproducible functionalization. *Nanoscale*, 7(5):1566–1585, 2015.

[105] Ying Wang, Yuyan Shao, Dean W Matson, Jinghong Li, and Yuehe Lin. Nitrogen-doped graphene and its application in electrochemical biosensing. *ACS nano*, 4(4):1790–1798, 2010.

[106] Frédéric Joucken, Yann Tison, Jérôme Lagoute, Jacques Dumont, Damien Cabosart, Bing Zheng, Vincent Repain, Cyril Chacon, Yann Girard, Andrés Rafael Botello-Méndez, et al. Localized state and charge transfer in nitrogen-doped graphene. *Physical Review B*, 85(16):161408, 2012.

[107] Frédéric Joucken, Yann Tison, Patrick Le Fèvre, Antonio Tejeda, Amina Taleb-Ibrahimi, Edward Conrad, Vincent Repain, Cyril Chacon, Amandine Bellec, Yann Girard, et al. Charge transfer and electronic doping in nitrogen-doped graphene. *Scientific reports*, 5(1):1–10, 2015.

[108] Alejandro Criado, Michele Melchionna, Silvia Marchesan, and Maurizio Prato. The covalent functionalization of graphene on substrates. *Angewandte Chemie International Edition*, 54(37):10734–10750, 2015.

[109] John Greenwood, Thanh Hai Phan, Yasuhiko Fujita, Zhi Li, Oleksandr Ivasenko, Willem Vanderlinden, Hans Van Gorp, Wout Frederickx, Gang Lu, Kazukuni Tahara, et al. Covalent modification of graphene and graphite using diazonium chemistry: tunable grafting and nanomanipulation. *ACS nano*, 9(5):5520–5535, 2015.

[110] Wei Chen, Shi Chen, Dong Chen Qi, Xing Yu Gao, and Andrew Thye Shen Wee. Surface transfer p-type doping of epitaxial graphene. *Journal of the American Chemical Society*, 129(34):10418–10422, 2007.

[111] Xiaochen Dong, Dongliang Fu, Wenjing Fang, Yumeng Shi, Peng Chen, and Lain-Jong Li. Doping single-layer graphene with aromatic molecules. *Small*, 5(12):1422–1426, 2009.

[112] Woo Jong Yu, Lei Liao, Sang Hoon Chae, Young Hee Lee, and Xiangfeng Duan. Toward tunable band gap and tunable dirac point in bilayer graphene with molecular doping. *Nano letters*, 11(11):4759–4763, 2011.

[113] Bing Li, Alexander V Klekachev, Mirco Cantoro, Cedric Huyghebaert, André Stesmans, Inge Asselberghs, Stefan De Gendt, and Steven De Feyter. Toward tunable doping in graphene fets by molecular self-assembled monolayers. *Nanoscale*, 5(20):9640–9644, 2013.

[114] Roald Phillipson, César J Lockhart De La Rosa, Joan Teyssandier, Peter Walke, Deepali Waghray, Yasuhiko Fujita, Jinne Adisoejoso, Kunal S Mali, Inge Asselberghs, Cedric Huyghebaert, et al. Tunable doping of graphene by using physisorbed self-assembled networks. *Nanoscale*, 8(48):20017–20026, 2016.

[115] Yasuhide Ohno, Kenzo Maehashi, Yusuke Yamashiro, and Kazuhiko Matsumoto. Electrolyte-gated graphene field-effect transistors for detecting ph and protein adsorption. *Nano letters*, 9(9):3318–3322, 2009.

[116] Qin Fan, Lude Wang, Duo Xu, Yanhong Duo, Jie Gao, Lei Zhang, Xianbao Wang, Xiang Chen, Jinhua Li, and Han Zhang. Solution-gated transistors of two-dimensional materials for chemical and biological sensors: status and challenges. *Nanoscale*, 2020.

[117] Guangyu Xu, Jeffrey Abbott, Ling Qin, Kitty YM Yeung, Yi Song, Hosang Yoon, Jing Kong, and Donhee Ham. Electrophoretic and field-effect graphene for all-electrical dna array technology. *Nature communications*, 5(1):1–9, 2014.

[118] Xin Jin, Hong Zhang, Yu-Tao Li, Meng-Meng Xiao, Zhi-Ling Zhang, Dai-Wen Pang, Gary Wong, Zhi-Yong Zhang, and Guo-Jun Zhang. A field effect transistor modified with reduced graphene oxide for immunodetection of ebola virus. *Microchimica Acta*, 186(4):223, 2019.

[119] Il-Yung Sohn, Duck-Jin Kim, Jin-Heak Jung, Ok Ja Yoon, Tien Nguyen Thanh, Trung Tran Quang, and Nae-Eung Lee. ph sensing characteristics and biosensing application of solution-gated reduced graphene oxide field-effect transistors. *Biosensors and Bioelectronics*, 45:70–76, 2013.

[120] Wangyang Fu, Cornelia Nef, Oren Knopfmacher, Alexey Tarasov, Markus Weiss, Michel Calame, and Christian Schonenberger. Graphene transistors are insensitive to ph changes in solution. *Nano letters*, 11(9):3597–3600, 2011.

[121] Hyo Eun Kim, Ariadna Schuck, June Ho Lee, and Yong-Sang Kim. Solution-gated graphene field effect transistor for tp53 dna sensor with coplanar electrode array. *Sensors and Actuators B: Chemical*, 291:96–101, 2019.

[122] Xiaochen Dong, Yumeng Shi, Wei Huang, Peng Chen, and Lain-Jong Li. Electrical detection of dna hybridization with single-base specificity using transistors based on cvd-grown graphene sheets. *Advanced Materials*, 22(14):1649–1653, 2010.

[123] Kibron website. https://www.kibron.com/aquapi-plusproduct.

[124] Fujifilm Dimatix. *Fujifilm Dimatix materials printer DMP-2800 Series user manual*. Fujifilm.

[125] Giorgio Mattana, Alberto Loi, Marion Woytasik, Massimo Barbaro, Vincent Noël, and Benoît Piro. Inkjet-printing: A new fabrication technology for organic transistors. *Advanced Materials Technologies*, 2(10):1700063, 2017.

[126] Snehajyoti Chatterjee, Shrikanth S Gadad, and Tapas K Kundu. Atomic force microscopy. *Resonance*, 15(7):622–642, 2010.

[127] Mehmet Z Baykara and UD Schwarz. Atomic force microscopy: Methods and applications. In *Encyclopedia of Spectroscopy and Spectrometry*. Elsevier, 2017.

[128] Ignacio Horcas, Rs Fernández, JM Gomez-Rodriguez, JWSX Colchero, JWSXM Gómez-Herrero, and AM Baro. Wsxm: a software for scanning probe microscopy and a tool for nanotechnology. *Review of scientific instruments*, 78(1):013705, 2007.

[129] Andrea Liscio, Konstantinos Kouroupis-Agalou, Xavier Diez Betriu, Alessandro Kovtun, Emanuele Treossi, Nicola Maria Pugno, Giovanna

De Luca, Loris Giorgini, and Vincenzo Palermo. Evolution of the size and shape of 2D nanosheets during ultrasonic fragmentation. *2D Materials*, 4(2):025017, February 2017.

[130] Hao Tong, Jiajia Zhu, Jianhui Chen, Yongqin Han, Sudong Yang, Bing Ding, and Xiaogang Zhang. Electrochemical reduction of graphene oxide and its electrochemical capacitive performance. *Journal of Solid State Electrochemistry*, 17(11):2857–2863, 2013.

[131] Yao Chen, Xiong Zhang, Dacheng Zhang, Peng Yu, and Yanwei Ma. High performance supercapacitors based on reduced graphene oxide in aqueous and ionic liquid electrolytes. *Carbon*, 49(2):573–580, 2011.

[132] Meng Cheng, Rong Yang, Lianchang Zhang, Zhiwen Shi, Wei Yang, Duoming Wang, Guibai Xie, Dongxia Shi, and Guangyu Zhang. Restoration of graphene from graphene oxide by defect repair. *Carbon*, 50(7):2581–2587, 2012.

[133] Haomin Wang, Yihong Wu, Chunxiao Cong, Jingzhi Shang, and Ting Yu. Hysteresis of electronic transport in graphene transistors. *ACS nano*, 4(12):7221–7228, 2010.

[134] Akshay Mathkar, Dylan Tozier, Paris Cox, Peijie Ong, Charudatta Galande, Kaushik Balakrishnan, Arava Leela Mohana Reddy, and Pulickel M Ajayan. Controlled, stepwise reduction and band gap manipulation of graphene oxide. *The journal of physical chemistry letters*, 3(8):986–991, 2012.

[135] Ke-Yan Lian, Yong-Fei Ji, Xiao-Fei Li, Ming-Xing Jin, Da-Jun Ding, and Yi Luo. Big bandgap in highly reduced graphene oxides. *The Journal of Physical Chemistry C*, 117(12):6049–6054, 2013.

[136] HK Jeong, MH Jin, KP So, SC Lim, and YH Lee. Tailoring the characteristics of graphite oxides by different oxidation times. *Journal of Physics D: Applied Physics*, 42(6):065418, 2009.

[137] Sandra Vasilijević, Giorgio Mattana, Guillaume Anquetin, Nicolas Battaglini, and Benoît Piro. Electrochemical tuning of reduced graphene oxide in printed electrolyte-gated transistors. impact on charge transport properties. *Electrochimica Acta*, 371:137819, 2021.

[138] Meryl D Stoller, Carl W Magnuson, Yanwu Zhu, Shanthi Murali, Ji Won Suk, Richard Piner, and Rodney S Ruoff. Interfacial capacitance of single layer graphene. *Energy & Environmental Science*, 4(11):4685–4689, 2011.

[139] Kui Xu, Xiao Ji, Chi Chen, Houzhao Wan, Ling Miao, and Jianjun Jiang. Electrochemical double layer near polar reduced graphene oxide electrode: Insights from molecular dynamic study. *Electrochimica Acta*, 166:142–149, 2015.

[140] Fang Chen, Quan Qing, Jilin Xia, Jinghong Li, and Nongjian Tao. Electrochemical gate-controlled charge transport in graphene in ionic liquid and aqueous solution. *Journal of the American Chemical Society*, 131(29):9908–9909, 2009.

[141] Beom Joon Kim, Moon Sung Kang, Viet Hung Pham, Tran Viet Cuong, Eui Jung Kim, Jin Suk Chung, Seung Hyun Hur, and Jeong Ho Cho. Low-voltage solution-processed graphene transistors based on chemically and solvothermally reduced graphene oxide. *Journal of Materials Chemistry*, 21(34):13068–13073, 2011.

[142] J-H Chen, C Jang, Masa Ishigami, S Xiao, William G Cullen, Ellen D Williams, and MS Fuhrer. Diffusive charge transport in graphene on sio2. *Solid State Communications*, 149(27-28):1080–1086, 2009.

[143] Sergey M Kozlov, Francesc Viñes, and Andreas Görling. On the interaction of polycyclic aromatic compounds with graphene. *Carbon*, 50(7):2482–2492, 2012.

[144] Khaireddine Ezzayani, Arbia Ben Khelifa, Eric Saint-Aman, Frederique Loiseau, and Habib Nasri. Complex of hexamethylenetetramine with magnesium-tetraphenylporphyrin: Synthesis, structure, spectroscopic characterizations and electrochemical properties. *Journal of Molecular Structure*, 1137:412–418, 2017.

[145] Fei Zheng, Wei-Long Xu, Han-Dong Jin, Xiao-Tao Hao, and Kenneth P Ghiggino. Charge transfer from poly (3-hexylthiophene) to graphene oxide and reduced graphene oxide. *RSC advances*, 5(109):89515–89520, 2015.

[146] Michele Di Lauro, Simona la Gatta, Carlo A Bortolotti, Valerio Beni, Vitaliy Parkula, Sofia Drakopoulou, Martina Giordani, Marcello Berto, Francesco Milano, Tobias Cramer, et al. A bacterial photosynthetic enzymatic unit modulating organic transistors with light. *Advanced Electronic Materials*, 6(1):1900888, 2020.

[147] Daiki Nishiori, Wenchao Zhu, Raphaël Salles, Mariko Miyachi, Yoshinori Yamanoi, Takashi Ikuta, Kenzo Maehashi, Tatsuya Tomo, and Hiroshi

Nishihara. Photosensing system using photosystem i and gold nanoparticle on graphene field-effect transistor. *ACS applied materials & interfaces*, 11(45):42773–42779, 2019.

[148] World Health Organization. Drinking-water. https://www.who.int/news-room/fact-sheets/detail/drinking-water.html.

[149] Manuela Schellin, Barbara Hauser, and Peter Popp. Determination of organophosphorus pesticides using membrane-assisted solvent extraction combined with large volume injection–gas chromatography–mass spectrometric detection. *Journal of Chromatography A*, 1040(2):251–258, 2004.

[150] Shimshon Belkin. Microbial whole-cell sensing systems of environmental pollutants. *Current opinion in microbiology*, 6(3):206–212, 2003.

[151] Maria Teresa Giardi and Emanuela Pace. Photosynthetic proteins for technological applications. *TRENDS in Biotechnology*, 23(5):257–263, 2005.

[152] Amina Antonacci and Viviana Scognamiglio. Biotechnological advances in the design of algae-based biosensors. *Trends in biotechnology*, 38(3):334–347, 2020.

[153] Christophe Védrine, Jean-Claude Leclerc, Claude Durrieu, and Canh Tran-Minh. Optical whole-cell biosensor using chlorella vulgaris designed for monitoring herbicides. *Biosensors and Bioelectronics*, 18(4):457–463, 2003.

[154] Dieter Frense, Adrian Müller, and Dieter Beckmann. Detection of environmental pollutants using optical biosensor with immobilized algae cells. *Sensors and Actuators B: Chemical*, 51(1-3):256–260, 1998.

[155] L Croisetiere, R Rouillon, and R Carpentier. A simple mediatorless amperometric method using the cyanobacterium synechococcus leopoliensis for the detection of phytotoxic pollutants. *Applied microbiology and biotechnology*, 56(1-2):261–264, 2001.

[156] Aliki Tsopela, Ahmet Lale, Emilie Vanhove, Olivier Reynes, Isabelle Séguy, Pierre Temple-Boyer, Philippe Juneau, R Izquierdo, and Jérôme Launay. Integrated electrochemical biosensor based on algal metabolism for water toxicity analysis. *Biosensors and Bioelectronics*, 61:290–297, 2014.

[157] Aliki Tsopela, Adrian Laborde, Ludovic Salvagnac, Vincent Ventalon, Eléna Bedel-Pereira, Isabelle Séguy, Pierre Temple-Boyer, Philippe Juneau,

R Izquierdo, and Jérôme Launay. Development of a lab-on-chip electrochemical biosensor for water quality analysis based on microalgal photosynthesis. *Biosensors and Bioelectronics*, 79:568–573, 2016.

[158] Michal Koblížek, Jan Malỳ, Jiří Masojídek, Josef Komenda, Tomáš Kučera, Maria T Giardi, Autar K Mattoo, and Roberto Pilloton. A biosensor for the detection of triazine and phenylurea herbicides designed using photosystem ii coupled to a screen-printed electrode. *Biotechnology and bioengineering*, 78(1):110–116, 2002.

[159] Isao Shitanda, Satoshi Takamatsu, Kunihiro Watanabe, and Masayuki Itagaki. Amperometric screen-printed algal biosensor with flow injection analysis system for detection of environmental toxic compounds. *Electrochimica Acta*, 54(21):4933–4936, 2009.

[160] Matteo Tucci, Matteo Grattieri, Andrea Schievano, Pierangela Cristiani, and Shelley D Minteer. Microbial amperometric biosensor for online herbicide detection: Photocurrent inhibition of anabaena variabilis. *Electrochimica Acta*, 302:102–108, 2019.

[161] Benoît Piro, Giorgio Mattana, and Steeve Reisberg. Transistors for chemical monitoring of living cells. *Biosensors*, 8(3):65, 2018.

[162] Jérémy Le Gall, Flavien Mouillard, Trung Ngoc Le, Thi Thu Vu, Giorgio Mattana, Roberta Brayner, Samia Zrig, Vincent Noël, and B Piro. Monitoring photosynthetic microorganism activity with an electrolyte-gated organic field effect transistor. *Biosensors and Bioelectronics*, page 112166, 2020.

[163] Chaojie Song and Jiujun Zhang. *Electrocatalytic Oxygen Reduction Reaction*, pages 89–134. Springer London, London, 2008.

[164] Charles C Liang and ANDRE L JULIARD. Reduction of oxygen at the platinum electrode. *Nature*, 207(4997):629–630, 1965.

[165] Ignacio Moreno-Garrido. Microalgae immobilization: current techniques and uses. *Bioresource technology*, 99(10):3949–3964, 2008.

[166] Roberta Brayner, Alain Couté, Jacques Livage, Catherine Perrette, and Clémence Sicard. Micro-algal biosensors. *Analytical and bioanalytical chemistry*, 401(2):581–597, 2011.

[167] Jérémy Le Gall, Sandra Vasilijević, Nicolas Battaglini, Giorgio Mattana, Vincent Noël, Roberta Brayner, and Benoît Piro. Algae-functionalized

hydrogel-gated organic field-effect transistor. application to the detection of herbicides. *Electrochimica Acta*, page 137881, 2021.

[168] Elias Said, Xavier Crispin, Lars Herlogsson, Sami Elhag, Nathaniel D Robinson, and Magnus Berggren. Polymer field-effect transistor gated via a poly (styrenesulfonic acid) thin film. *Applied Physics Letters*, 89(14):143507, 2006.

[169] Jiang Liu, Lars Herlogsson, A Sawatdee, P Favia, Mats Sandberg, Xavier Crispin, Isak Engquist, and Magnus Berggren. Vertical polyelectrolyte-gated organic field-effect transistors. *Applied Physics Letters*, 97(10):197, 2010.

[170] TG Bäcklund, R Österbacka, H Stubb, J Bobacka, and A Ivaska. Operating principle of polymer insulator organic thin-film transistors exposed to moisture. *Journal of applied physics*, 98(7):074504, 2005.

[171] Matthew J Panzer and C Daniel Frisbie. High carrier density and metallic conductivity in poly (3-hexylthiophene) achieved by electrostatic charge injection. *Advanced Functional Materials*, 16(8):1051–1056, 2006.

[172] Justine Pallu, Meltem Avci-Adali, Peter Mackeben, Leila Mohammadnejad, Giorgio Mattana, Vincent Noël, and Benoît Piro. A dna hydrogel gated organic field effect transistor. *Organic Electronics*, 75:105402, 2019.

[173] Soizic Morin, Betty Chaumet, and Nicolas Mazzella. A time-dose response model to assess diuron-induced photosynthesis inhibition in freshwater biofilms. *Frontiers in Environmental Science*, 6:131, 2018.

[174] Water framework directives-priority substances. European Commission. https://www.ec.europa.eu/environment/water/water-framework.

[175] Randall Baselt. Encyclopedia of toxicology, 2014.

[176] A William Rutherford and Anja Krieger-Liszkay. Herbicide-induced oxidative stress in photosystem ii. *Trends in biochemical sciences*, 26(11):648–653, 2001.

[177] Luis Miguel Rivera, Gonzalo García, and Elena Pastor. Novel graphene materials for the oxygen reduction reaction. *Current Opinion in Electrochemistry*, 9:233–239, 2018.

[178] Jaana Lilloja, Elo Kibena-Põldsepp, Maido Merisalu, Protima Rauwel, Leonard Matisen, Ahti Niilisk, Eduardo SF Cardoso, Gilberto Maia, Väino

Sammelselg, and Kaido Tammeveski. An oxygen reduction study of graphene-based nanomaterials of different origin. *Catalysts*, 6(7):108, 2016.

[179] Fuping Pan, Youxin Duan, Xinkai Zhang, and Junyan Zhang. A facile synthesis of nitrogen/sulfur co-doped graphene for the oxygen reduction reaction. *ChemCatChem*, 8(1):163–170, 2016.

[180] Frank Bloos and Konrad Reinhart. Rapid diagnosis of sepsis. *Virulence*, 5(1):154–160, 2014.

[181] Terence Chan and Frank Gu. Early diagnosis of sepsis using serum biomarkers. *Expert review of molecular diagnostics*, 11(5):487–496, 2011.

[182] Sepsis. World Health Organization. https://www.who.int/news-room/fact-sheets/detail/sepsis.

[183] Meningitis. World Health Organization. https://www.who.int/news-room/fact-sheets/detail/meningococcal-meningitis.

[184] Rishi S Nannan Panday, Eline MJ Lammers, Nadia Alam, and Prabath WB Nanayakkara. An overview of positive cultures and clinical outcomes in septic patients: a sub-analysis of the prehospital antibiotics against sepsis (phantasi) trial. *Critical Care*, 23(1):182, 2019.

[185] Ngo Tat Trung, Nguyen Sy Thau, Mai Hong Bang, et al. Pcr-based sepsis@ quick test is superior in comparison with blood culture for identification of sepsis-causative pathogens. *Scientific reports*, 9(1):1–7, 2019.

[186] Konrad Reinhart, Michael Meisner, and Frank M Brunkhorst. Markers for sepsis diagnosis: what is useful? *Critical care clinics*, 22(3):503–19, 2006.

[187] Meningitis defeating. World Health Organization. https://www.who.int/publications/m/item/defeating-meningitis-2030-baseline-situation-analysis.

[188] Woong Sun Lim, Yi Yeon Kim, Hyeongkeun Kim, Sukjae Jang, Namyong Kwon, Beyoung Jae Park, Jong-Hyun Ahn, Ilsub Chung, Byung Hee Hong, and Geun Young Yeom. Atomic layer etching of graphene for full graphene device fabrication. *Carbon*, 50(2):429–435, 2012.

[189] Haider Al-Mumen, Fubo Rao, Wen Li, and Lixin Dong. Singular sheet etching of graphene with oxygen plasma. *Nano-Micro Letters*, 6(2):116–124, 2014.

[190] Marco Gobbi, Sara Bonacchi, Jian X Lian, Yi Liu, Xiao-Ye Wang, Marc-Antoine Stoeckel, Marco A Squillaci, Gabriele D'avino, Akimitsu Narita, Klaus Müllen, et al. Periodic potentials in hybrid van der waals heterostructures formed by supramolecular lattices on graphene. *Nature communications*, 8(1):1–8, 2017.